14. SITE 849[1]

Shipboard Scientific Party[2]

HOLE 849A

Date occupied: 7 June 1991

Date departed: 8 June 1991

Time on hole: 7 hr, 41 min

Position: 0°10.983′N, 110°31.183′W

Bottom felt (rig floor; m, drill-pipe measurement): 3848.8

Distance between rig floor and sea level (m): 11.7

Water depth (drill-pipe measurement from sea level, m): 3837.1

Total depth (rig floor; m): 3857.5

Penetration (m): 8.7

Number of cores (including cores with no recovery): 1

Total length of cored section (m): 8.7

Total core recovered (m): 8.69

Core recovery (%): 99.9

Oldest sediment cored:
Depth (mbsf): 8.7
Nature: clayey diatom nannofossil ooze
Earliest age: Pleistocene

HOLE 849B

Date occupied: 8 June 1991

Date departed: 10 June 1991

Time on hole: 2 days, 12 hr, 44 min

Position: 0°10.983′N, 110°31.183′W

Bottom felt (rig floor; m, drill-pipe measurement): 3850.8

Distance between rig floor and sea level (m): 11.7

Water depth (drill-pipe measurement from sea level, m): 3839.1

Total depth (rig floor; m): 4201.3

Penetration (m): 350.5

Number of cores (including cores with no recovery): 37

Total length of cored section (m): 350.5

Total core recovered (m): 343.78

Core recovery (%): 98.1

Oldest sediment cored:
Depth (mbsf): 349.0
Nature: nannofossil ooze with diatoms and foraminifers
Earliest age: late Miocene

Basement:
Depth sub-bottom (m): 350.5
Nature: basalt

HOLE 849C

Date occupied: 10 June 1991

Date departed: 11 June 1991

Time on hole: 14 hr, 6 min

Position: 0°10.991′N, 110°31.177′W

Bottom felt (rig floor; m, drill-pipe measurement): 3850.8

Distance between rig floor and sea level (m): 11.7

Water depth (drill-pipe measurement from sea level, m): 3839.1

Total depth (rig floor; m): 3956.3

Penetration (m): 105.5

Number of cores (including cores with no recovery): 11

Total length of cored section (m): 104.5

Total core recovered (m): 105.7

Core recovery (%): 101.1

Oldest sediment cored:
Depth (mbsf): 105.5
Nature: diatom nannofossil ooze with radiolarians
Earliest age: Pliocene

HOLE 849D

Date occupied: 11 June 1991

Date departed: 12 June 1991

Time on hole: 1 day, 13 hr, 26 min

Position: 0°10.993′N, 110°31.167′W

Bottom felt (rig floor; m, drill-pipe measurement): 3850.8

Distance between rig floor and sea level (m): 11.7

Water depth (drill-pipe measurement from sea level, m): 3839.1

Total depth (rig floor; m): 4177.5

Penetration (m): 326.7

Number of cores (including cores with no recovery): 34

Total length of cored section (m): 322.7

Total core recovered (m): 319.45

Core recovery (%): 99.0

Oldest sediment cored:
Depth (mbsf): 322.70
Nature: radiolarian nannofossil ooze
Earliest age: late Miocene

Principal results: Site 849 (WEQ-6), located less than 20 km from the Equator, presently lies within the equatorial divergence zone. This is the second site drilled along the Leg 138 western (110°W) transect, a transect designed to sample the various elements of the equatorial circulation system in an area far removed from the influence of the eastern boundary of the Pacific Ocean. The transect also serves as the eastern end member of a series of studies (Legs 85 and 130) aimed at understanding the regional and global responses of the equatorial Pacific Ocean to changes in climate.

Four holes were drilled at Site 849. Hole 849A was a single APC mud-line core dedicated to whole-round geochemical and physical property measurements. Hole 849B was APC-cored to 120.7 mbsf before excessive overpull required the drilling crew to switch to the XCB-coring system. The hole was continued to 350.5 mbsf, where basement was reached. After completing three logging runs in Hole 849B, the drilling crew APC-cored Hole 849C to a depth of 105.5 mbsf. Hole 849D was APC-cored to 108.5 mbsf and then continued with the XCB to a total depth of 326.7 mbsf, when the time allocated for completion of operations at Site 849 was reached. Real-time analysis of continuous GRAPE, susceptibility, and color reflectance measurements showed that overlapping triple APC-coring, combined with double XCB-coring assured nearly 100% recovery of the entire sediment section at this site.

The sedimentary sequence can be described as a single lithologic unit composed primarily of diatom nannofossil ooze with minor intervals of diatom ooze. The sediment is characterized by a very high degree of variability that is best described by the high-frequency changes in the GRAPE density (which primarily reflects calcium carbonate content) and in the color reflectance. These signals show a remarkable correlation with other Leg 138 sites, indicating the degree to which these data sets may provide high-resolution stratigraphy. The correlation is so strong that it is possible to use correlations from Site 846 (more than 1900 km to the east of Site 849) to resolve gaps between successive XCB cores in Site 849.

While magnetic intensities were too low at this site to provide a magnetostratigraphy, stratigraphic age control was provided by all four of the chief planktonic microfossil groups, though their abundances and state of preservation differ significantly. With the exception of the lower 10 m of the section that is barren of diatoms, radiolarians and diatoms are abundant with moderate to good preservation from the upper Miocene to the Pleistocene. Calcareous nannofossils are generally abundant and well preserved throughout the Pleistocene and Pliocene with slight etching of some placoliths and moderate to strong overgrowth of discoasterids in the Miocene. Foraminifers are common in the Pleistocene and late Pliocene and rarer in the rest of the section. Preservation of foraminifers is, however, poor throughout the sequence.

Sedimentation rates at this site were relatively high during the late Pliocene and Pleistocene and ranged from 25 to 35 m/m.y. During the late Miocene and early Pliocene, rates were extremely high, ranging from 55 to as much as 100 m/m.y. and providing a greatly expanded section. The lowest sedimentation rates in the section (about 15 m/m.y.) are found in the oldest sediment (between 8 and 10 Ma) of the site.

Three logging runs were completed, including the geophysical and geochemical tool strings and the formation microscanner. For the most part, variability in the logs dominantly reflects changes in the calcium carbonate content of the sedimentary sequence and shows a high degree of correlation with directly measured sediment properties such as GRAPE density. Velocity and density profiles from the logs can be used to produce an excellent match between the observed seismic profile and a calculated synthetic profile, a correlation that we hope will allow us to extrapolate our results well beyond the borehole.

The chemistry of interstitial waters at Site 849 is influenced by recrystallization and diagenesis. Diffusive transport of some constituents has been disrupted by a layer of diagenetic carbonate found at about 235 mbsf (~6.2 Ma). This layer effectively seals off the bottom 100 m of the sediment column, disrupting diffusive communication between the material above and below. The effect of this layer can be seen in the profiles of alkalinity, sulfate, ammonia, calcium, and strontium; above this layer, these profiles have been controlled by diagenesis; below they have been controlled by diffusion.

The expanded record at Site 849 provides an important opportunity to study equatorial divergence during the late Neogene. While the high productivity associated with the expanded record comes with the price of no magnetic stratigraphy, the phenomenally consistent, high-resolution GRAPE density record can be used as a stratigraphic tool to correlate this site with other sites along the eastern transect of Leg 138. This correlation will make it possible to examine in detail the response of both temporal and spatial gradients in the Pacific Ocean to global climate change. The

continuous double XCB section presents an opportunity to continue high-resolution studies through the late Miocene. Thus, even though the paleomagnetism has returned "to the salt mines," Leg 138 continues to be a "cornucopia" for high-resolution paleoceanographic and paleoclimatic studies. At the conclusion of Site 849, the Leg 138 seismologists had completed 8.72 log ($m^2 \bullet$ kt).

BACKGROUND AND SCIENTIFIC OBJECTIVES

Site 849 is located beneath the present-day equatorial divergence zone; the primary objective of this site was to provide a late Neogene record of equatorial divergence in the eastern equatorial Pacific in a region removed from the direct effects of the eastern boundary of the Pacific Ocean (Fig. 1). The closest previously piston-cored drill site to Site 849 is DSDP Site 572, located approximately 350 km west. The combination of a failed core orientation tool and low magnetization, however, precluded Site 572 from having magnetic stratigraphy for this key location. In addition, Site 572 was cored with the older designed hydraulic piston core and thus contains many intervals of core disturbance, making it impossible to construct a continuous composite record at this site. While we expected relatively low magnetic intensities associated with high biogenic accumulation rates, we hoped to improve upon results of Site 572. In particular, we hoped to take advantage of the improved capabilities of the APC-coring system to use real-time monitoring of core overlap to help ensure recovery of a complete late Neogene section.

Based on basement subsidence and spreading rate estimates for this sector of the Pacific Ocean, the basement age at Site 849 was expected to be approximately 12.5 m.y. (Fig. 2). The site is located north of a detailed site survey conducted on the Equator as part of the *Thomas Washington* Venture 1 expedition. Within this region, surficial and basement topographies are generally subdued, with both basement and surficial relief increasing to the west and the southeast. A small basement peak rises approximately 300 m above the surrounding seafloor in the western extreme of the survey area (Fig. 3); a well-developed moat around this basement high attests to the activity of bottom currents in the region. While small drilling targets could be found within the detailed survey area, the location of Site 849 was placed 9 km north of the detailed survey in an area where the sediment was thickest and least disturbed, and evidence for channel development absent. The sediment thickness here is about 340 m, and the reflectors are relatively flat-lying and undisturbed (Fig. 4).

OPERATIONS

Transit to Site 849

The transit to Site 849 (prospectus Site WEQ-6) covered 171 nmi in 13.8 hr at an average speed of 11.6 kt. At 1245 hr (all times are in local time, L, which is Universal Time Coordinated, UTC, minus 7 hr; all times in Table 1 are UTC) 7 June, the vessel slowed to 6 kt so that the seismic gear could be deployed and a short seismic survey begun; this survey covered 22 nmi at an average speed of 6.1 kt. A beacon was deployed at 1639L 7 June, approximately 7.5 km north of the proposed location. The site survey continued for 10 min after beacon deployment, then the ship returned to the site location and we had lowered the thrusters and hydrophones by 1730L 7 June. The depth to the seafloor at Site 849, based upon the precision depth recorder (PDR), was 3855.0 mbrf.

Hole 849A

This hole was a single mud-line core dedicated to whole-round geochemical and physical property measurements. The pipe was lowered to a depth of 3848 mbrf, and the first (and only) piston core was on deck at 0045L 8 June (see Table 1 for coring summary). The core was retrieved with a full barrel, thus permitting only an estimate of mud-line depth (3848.8 mbrf).
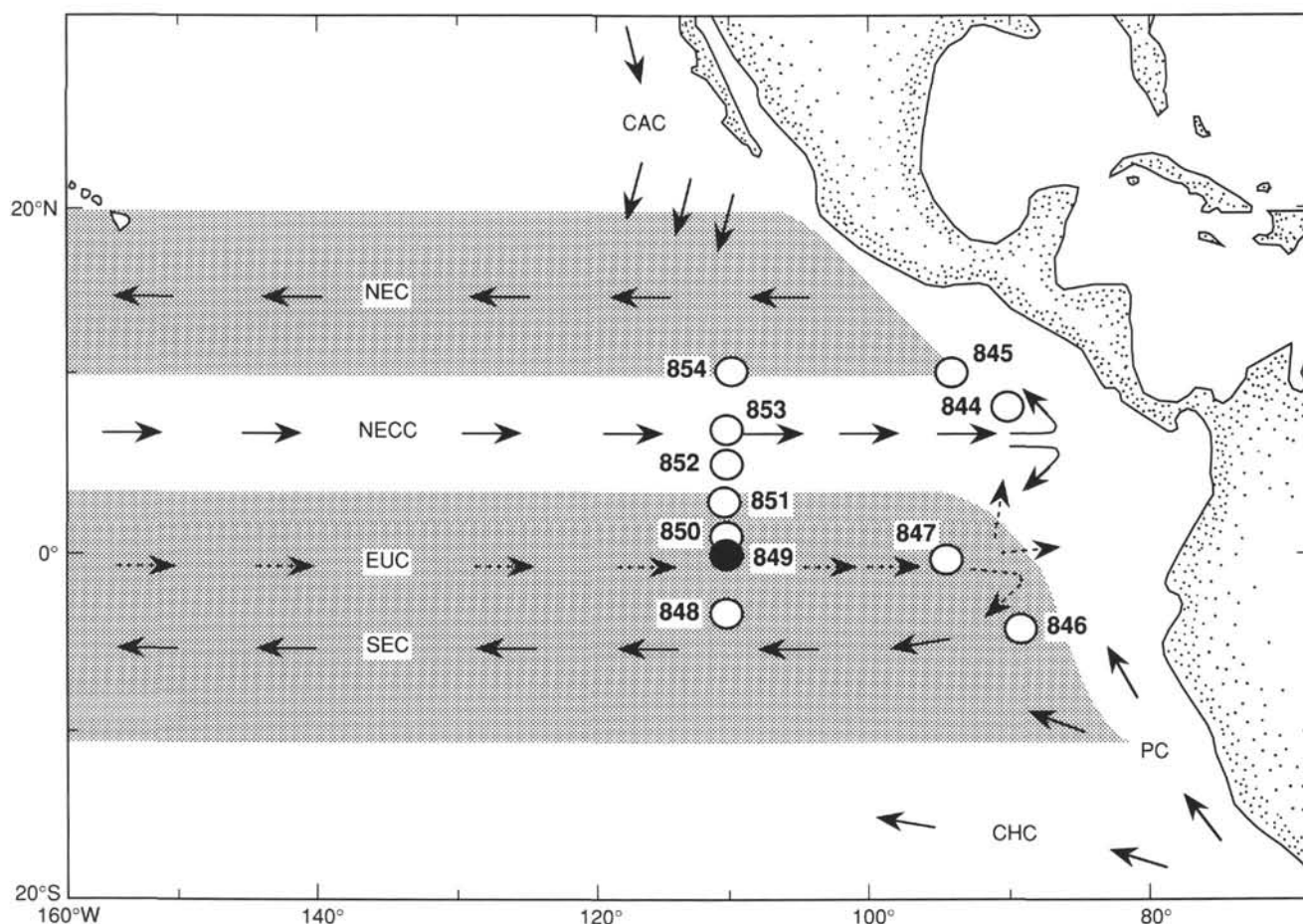
Figure 1. Location of Site 849 and generalized circulation system of the eastern equatorial Pacific Ocean. Other Leg 138 sites are shown for reference. Surface current shown as solid arrows, subsurface current as dashed arrows. CAC = California Current; NEC = North Equatorial Current; NECC = North Equatorial Countercurrent; EUC = Equatorial Undercurrent; SEC = South Equatorial Current; PC = Peru Current; CHC = Chile Current. Shaded area illustrates general latitudinal extent of the SEC and NEC.

Hole 849B

At 0155L 8 June, Core 138-849B-1H was taken in a water depth of 3848 mbrf and from it we retrieved 6.76 m of sediment, establishing the mud-line depth at 3850.8 mbrf. APC Cores 138-849B-1H through -13H were taken from 0 to 120.7 mbsf, with orientation beginning at Core 138-849B-4H. An overpull of 100,000 lb was required to pull Core 138-849B-13H from the sediment; thus, the APC-coring program in Hole 849B was terminated at this point. Recovery in the APC interval was 102.8%.

Drilling continued with the XCB-coring system, and Cores 138-849-14X through-37X were taken over the interval from 120.7 to 350.5 mbsf. Core 138-849B-37X was drilled about 1.5 m into basement, but only 13 cm of basalt fragments was recovered. XCB-coring concluded at this point, and the hole was prepared for logging.

Recovery in the XCB section of the hole was 95.6%.

Logging at Hole 849B

The hole was swept with mud, and pipe was pulled to the logging depth of 61.0 mbsf. All three standard ODP tool strings were run, with only a few operational problems (see Table 2 for a summary of logging operations). The heave compensator did not function properly, and the hole thus was logged without it. The absence of compensation for heave did not affect log quality significantly, as the height of swells

was only 2 to 3 ft, and only a few uncompensated accelerations were noted in the initial processing of the FMS data.

The first logging run was with the geophysical tool string. The downward pass logged the hole from 61.0 to 350.2 mbsf and the main upward pass logged the hole from 350.2 to 71.9 mbsf. During the upward pass, the base of the tool string stuck in the open hole at 149.7 mbsf. The tool was twice lowered and raised to break it free but without success. The third attempt freed the tool string. Tool sticking on the upward pass resulted in step-like structures around 135–116 mbsf in the velocity and density logs. Further up the hole, the tool again experienced minor sticking problems, as evidenced by large variations in cable tension. During the repeat geophysical run, from 172.5 to 71.9 mbsf, the tool experienced minor sticking problems above 114 mbsf.

Next, the geochemical tool was lowered into the hole. At a depth of a few hundred meters below the rig floor, the ACT sonde appeared nearly ready to fail and was brought to the surface for repairs. The tool was then lowered to total depth (351.1 mbsf), the GST calibrated, and the main log run from 351.1 mbsf to the mudline. No sticking problems occurred during the geochemical run.

The FMS tool was rigged up and lowered to total depth (350.5 mbsf). During the first pass, the hole was logged over the interval from 350.5 to 233.5 mbsf. The tool string was lowered back to total depth and a second pass was made from 350.5 to 111.6 mbsf. The log was stopped at 111.6 mbsf during the second pass because the hole
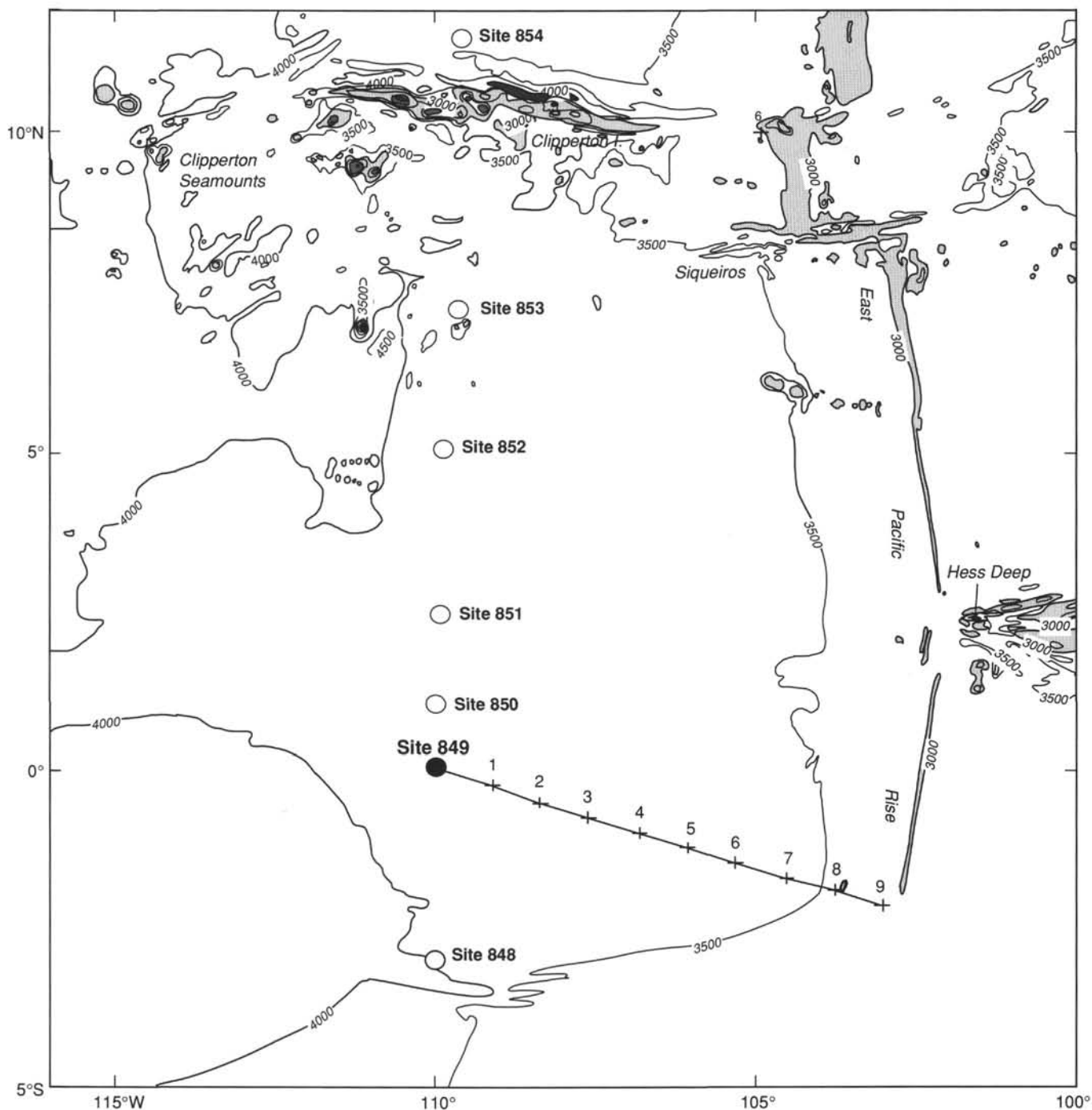
Figure 2. Generalized bathymetric map showing location of Site 849 and other Leg 138 sites drilled along the 110°W transect (from Mammerickx, 1989). Backtracked path shows location of Site 849 in 1 m.y. increments for past 9 m.y. Bathymetry in meters.

was washed out well beyond the maximum FMS caliper extension. After the calipers were closed, the FMS tool string was brought to the surface and logging operations concluded. The drill string was then pulled out of the hole, and the bit cleared the mud line at 1304L 10 June, ending Hole 849B.

Hole 849C

Hole 849C was drilled to ensure that a continuous APC section was recovered and that enough material was available for high-reso-lution paleoceanographic studies. The vessel was offset 20 m south, and the bit was washed down 1 m below the mud line to 3851.8 mbrf. The first piston core barrel landed too hard, and the shear pin parted, prefiring the core. During the next APC attempt, the overshot shear pin parted (damaged in the initial landing), necessitating another wireline round trip.

The first piston core was successfully taken at 1645L 10 June. APC-coring continued to total depth (Core 138-849C-11H; 105.5 mbsf), with orientation beginning at Core 138-849C-4H. The recovery for Hole 849C was 101.1%. The pipe was then pulled above the
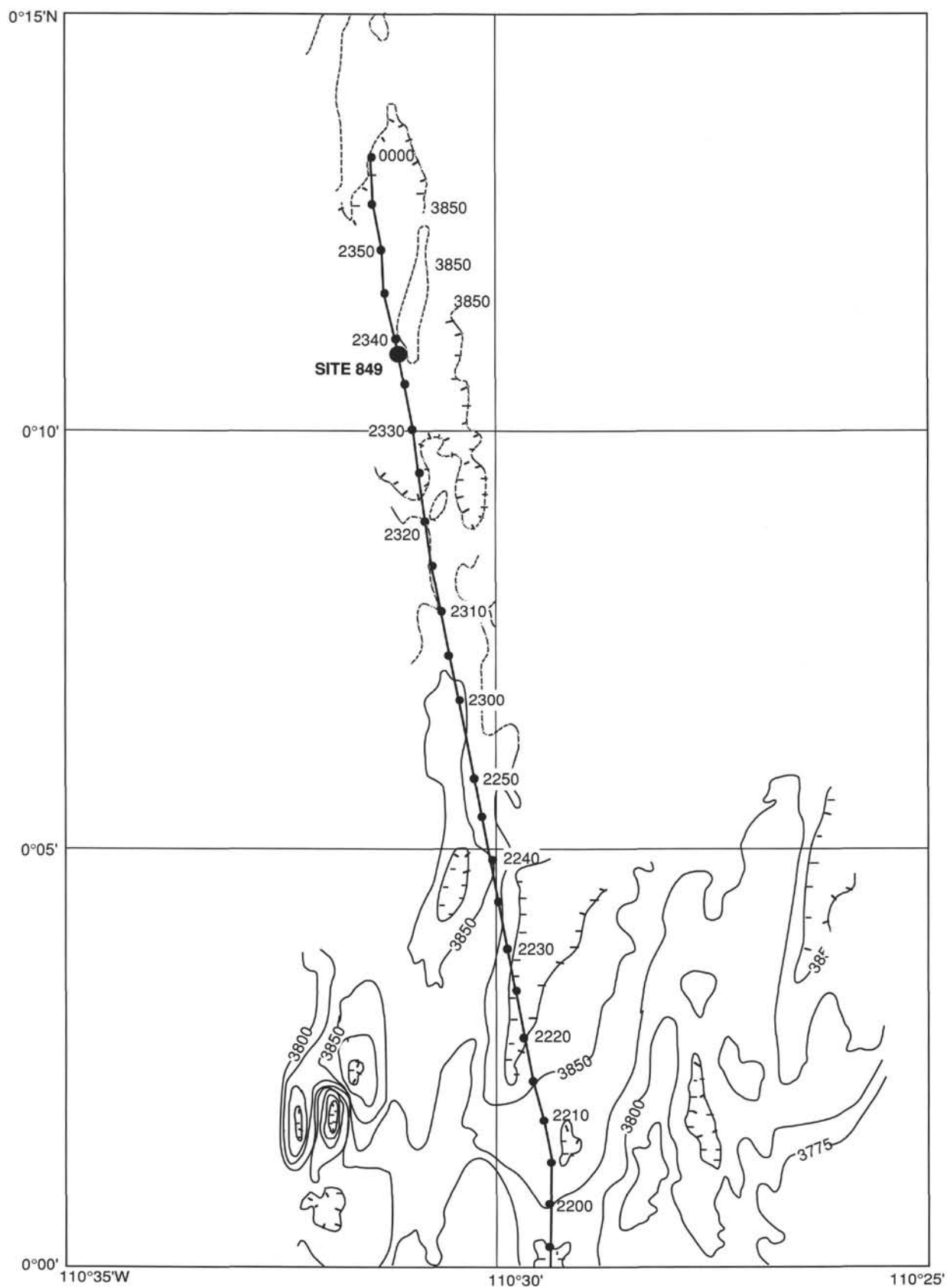
Figure 3. SeaBeam map hand-contoured from navigation-adjusted SeaBeam contour maps collected from the *Thomas Washington* during the Venture 1 cruise, September 1989. Location of Site 849 is shown.
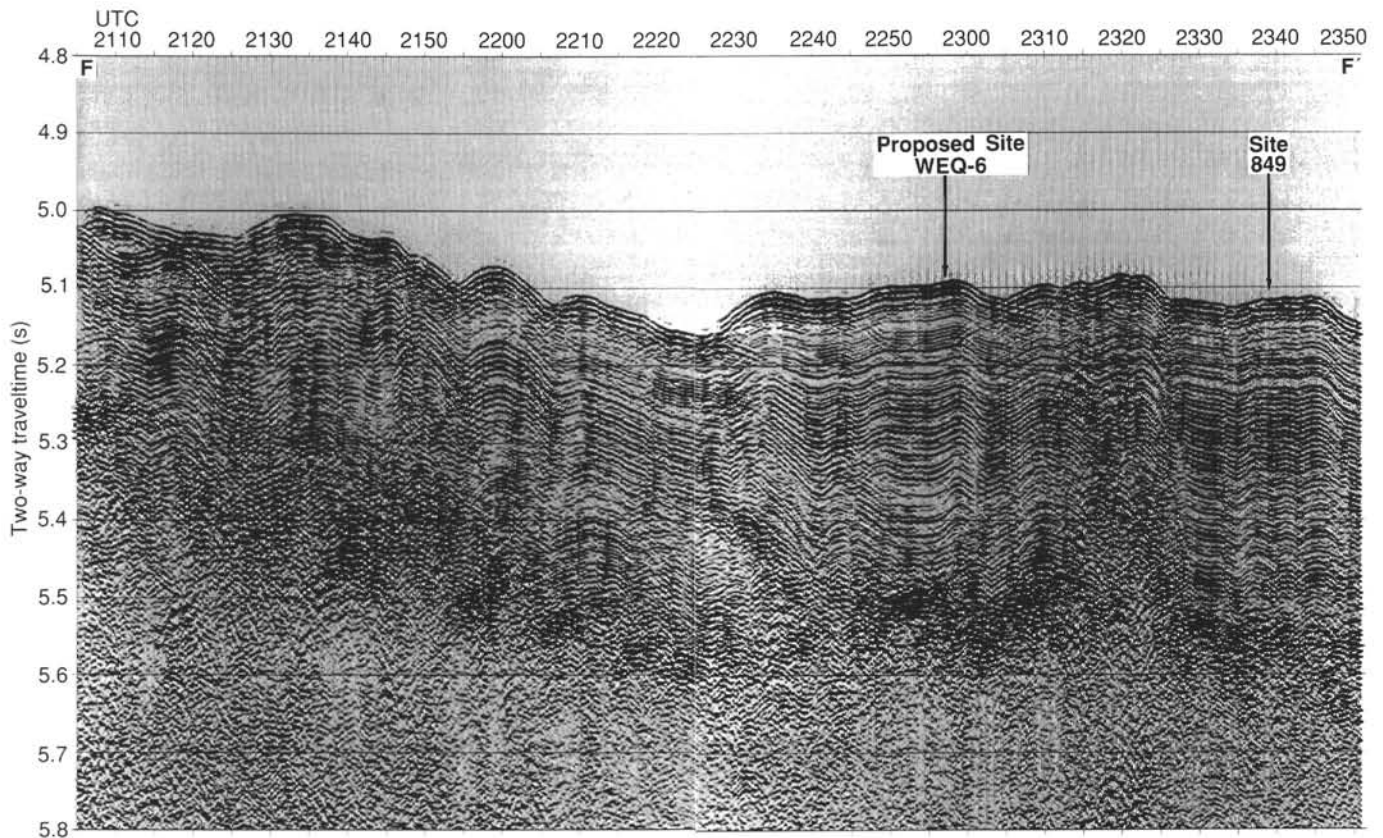
Figure 4. Seismic line collected with an 80-in.[3] water gun during the *JOIDES Resolution* survey of Site 849. Proposed Site WEQ-6 is shown as well as final position of Site 849.

mudline to begin another hole. The bit cleared the mudline at 0310 hr, 11 June, ending Hole 849C.

Hole 849D

Hole 849 was drilled to ensure that a continous APC section was recovered and to try to recover a complete XCB section. The vessel was offset 20 m east and the bit was washed down 4 m below the mudline to 3854.8 m. Core 138-849D-1H was taken at 0415 hr, 11 June. APC coring advanced to 108.5 mbsf (Core 138-849D-11H) with orientation beginning with Core 138-849D-4H. XCB coring began after Core 138-11H and continued through Core 138-849D-34X (326.7 mbsf), at which point time constraints forced the termination of the hole. Recovery was 91.9% in the APC interval and 102.3% in the XCB interval.

The last core (138-849D-34X) was retrieved slowly to coat the aft sand line. The forward core line would be used for the rest of the leg. At 0925L 12 June, the last core was brought on deck and the pipe was pulled out of the hole. After the bit came on deck at 1610L, the rig floor was quickly secured, the hydrophones and thrusters were retracted, and the vessel began the transit to Site 850 at 1630L 12 June.

LITHOSTRATIGRAPHY

Introduction

The sediments at Site 849 are composed primarily of diatom nannofossil ooze with minor intervals of diatom ooze. APC coring at four holes and XCB coring at two holes (849B and 849D) recovered a nearly continuous sedimentary section (see "Sedimentation Rates" section, this chapter). This sedimentary sequence spans the Pleistocene to upper Miocene and terminates at basalt basement 350.5 mbsf in Hole 849B (Fig. 5).

Characterization of sediments at this site was based on visual core descriptions and smear-slide analyses. The continuously measured lithologic parameters GRAPE density, magnetic susceptibility, and color reflectance (Fig. 6), as well as logging measurements, physical properties, and chemistry data, were useful for documenting the lithology of this site.

The sedimentary sequence at Site 849 can be described as one lithologic unit of diatom nannofossil ooze with interbeds of nannofossil diatom ooze. The interbeds range in thickness from less than 5 cm to greater than 1 m. Nannofossil abundance in the sequence ranges from 15% to 85% (as estimated by smear-slide analyses). Diatom abundance is, in general, inversely proportional to nannofossil abundance and ranges from 5% to 75% (Fig. 7). Foraminifers are common in the upper 100 m, but are a minor constituent (less than 10%) below this depth. Radiolarian abundance is generally less than 5%, with the exception of two intervals, from 90 to 105 mbsf and 275 to 330 mbsf, where their abundance ranges from 7% to 38%.

Description of Units

Lithologic Unit I

Intervals:
  Cores 138-849A-1H, -849B-1H through -849B-37X, -849C-1H
    through -849C-11H, -849D-1H through -849D-34X
Age: Pleistocene to late Miocene
Depth: 0.0–8.7 mbsf, Hole 849A; 0.0–350.5 mbsf, Hole 849B; 1.0
  –105.5 mbsf, Hole 849C; 4.0–326.7 mbsf, Hole 849D.

A color change from pale brown (10YR 8/3 to 10YR 5/2) to light gray (5Y 7/1 to N 7) at the top of the sedimentary sequence (Sections 138-849A-1H-3, 100 cm; -849B-1H-3, 90 cm; -849C-1H-2, 87 cm) marks the transition from oxidizing conditions above this level to

reducing conditions below. Through approximately 70 mbsf in Holes 849B, C, and D, the sediments are composed of diatom foraminifer nannofossil ooze, grading into a foraminifer diatom nannofossil ooze with radiolarians from 70 to 100 mbsf. Foraminifers represent 10% to 30% of the sedimentary constituents (as indicated by smear-slide analyses, Fig. 7). Below 100 mbsf, foraminifers become a minor constituent (less than 10%). Diatoms are present throughout the upper 100 m of the sequence, comprising from 10% to 30% of the major lithology. Nannofossil diatom ooze occurs as interbeds from 27 to 52 mbsf. Elsewhere, diatom-rich intervals are present as burrow fills. Radiolarians are a minor constituent in the interval from 0 to 100 mbsf, reaching abundances of 10% to 20% from 70 to 100 mbsf.

Sediments from 110 to 125 mbsf, below the upper interval of increased foraminifer abundance (Cores 138-849B-13X, -14X, 138-849D-12X, and -13X) contain thick (up to 1 m) beds of pale olive (5Y 6/3) nannofossil diatom ooze interbedded with diatom nannofossil ooze, some of which is laminated. This interval, approximately 4.3–4.6 Ma, is dominated by the diatom *Thalassiothrix longissima* (Fig. 8).

From 125 through about 236 mbsf, the sedimentary sequence is characterized by interbedded diatom nannofossil ooze and nannofossil diatom ooze. These interbeds vary in thickness from less than 5 cm to greater than 1 m. Diatom content in this interval ranges from 15% to 40%, with values as high as 70%. The nannofossil-rich major lithology is very pale gray (N8), while the diatom-rich minor lithology is generally light gray (N7) to yellowish-gray (5Y 8/1) and pale olive (5Y 6/3) in the most diatom-rich intervals (Fig. 9). This interbedded interval terminates at 237.2 mbsf in Hole 849B and 235.1 mbsf in Hole 849D (Sections 138-849B-26X-2, 3 cm, and -849D-25X-4, 10 cm), where a 3-cm layer of silicified carbonate occurs.

From 236 to 255 mbsf, the diatom content of the sediments is lower than in the overlying interval, but very pale gray (N8) and yellowish-gray (5Y 7/1) compositional color banding resumes at 255 mbsf and continues through approximately 280 mbsf. While interbedding is not indicated in the smear-slide summaries for this site, %CaCO$_3$ and GRAPE density variations show fluctuations similar to the interval from 125 to 235 mbsf (Fig. 10).

An interval of nannofossil diatom ooze occurs between approximately 280 and 305 mbsf (Cores 138-849B-33X, -849D-31X and -32X). This interval (age ca. 10 Ma) varies from light gray (N6) to greenish-gray (5BG 6/1) to dark greenish-gray (5Y 4/1). Diatoms in this interval are a mixture of species. Radiolarians are common, up to 40% of the total sediment (Fig. 7). From approximately 305 to 322 mbsf in Holes 849B and 849D (Cores 138-849B-34X to -35X and -849D-33X), sediments are radiolarian nannofossil ooze and diatom radiolarian nannofossil ooze. The color in this radiolarian-rich interval also varies from gray (N6) to greenish-gray (5GY 6/1).

The base of the sediment sequence is marked by a distinct transition from light greenish-gray (5G 7/1 and 5G 6/1) to pale yellow (2.5Y 7/4) sediments (Section 138-849B-36X-3, 145 cm) at approximately 336.7 mbsf. From this depth down to basalt basement at 350 mbsf, very small hematite clasts and manganese dendrites are present (Fig. 11).

Color Reflectance Spectroscopy

Although visual color observations serve to identify lithologic contacts and diagenetic features, automated color spectroscopy provided a more continuous and quantitative record of color changes. The reflectance spectroscopy data for the entire sedimentary sequence clearly demonstrate the dominance of small-scale variability at Site 849. In Figure 12, three channels of reflectance data (blue = 450–500 nm, red = 650–700 nm, and near-infrared = 850–900 nm) are given, with examples of reflectance spectra at full resolution (511 channels) for some of the lithologies described above.

In the upper part of the sedimentary column, reflectance data clearly delineate nannofossil diatom ooze from diatom nannofossil ooze, as the more diatom-rich material has greater reflectance in the

near infrared-bands (>700 nm) than in the visible bands (<700 nm), while the opposite occurs in the nannofossil ooze. Often the more diatom-rich intervals have lower average reflectance than the nannofossil-rich zones. This difference is shown in Figure 12 by example spectra of nannofossil diatom ooze (containing around 70% diatoms) from Section 138-849B-6H-3, 10 cm (47.80 mbsf) and of diatom nannofossil ooze (containing around 65% nannofossils) from Section 138-849B-6H-4, 122 cm (50.42 mbsf). In the oxidized layer near the sediment/water interface, both diatom- and nannofossil-rich lithologies have high red and near-infrared reflectance. This presumably results from the presence of oxide minerals.

The olive-gray diatom oozes dominated by *Thalassiothrix longissima* (described above) are illustrated by a reflectance spectrum from Section 138-849B-14X-3, 110 cm (Fig. 12). This spectrum is similar to that of the nannofossil diatom ooze, but more extreme with near-infrared reflectance 20% greater than visible reflectance.

In the interval from about 280 to 330 mbsf, the sediments are on average darker than in the rest of the sedimentary sequence. This zone contains higher concentrations of radiolarians and diatoms, but the spectral character of this interval is different from that of the other diatom oozes (Fig. 12). This sediment has the lowest average reflectance measured at this site. Notably, the near-infrared reflectance is roughly the same as the visible reflectance. Lowest reflectance occurs in the red and near-infrared bands, near 700 nm.

The basal sediments contain oxides and have relatively high reflectance in the red and infrared bands (>650 nm) and low reflectance in the blue and green bands (<550 nm). The example illustrated in Figure 12 shows an additional reflectance peak in the yellow band (550–600 nm).

Trace Fossils

Burrowing is moderate to strong within the sediments recovered at Site 849, except within the intervals of laminated diatom ooze discussed above. Solid burrows and *Planolites* are the most commonly recognized trace fossils and occur throughout. Solid burrows and *Planolites* within the very light-gray intervals commonly contain light-gray or light olive-gray (5Y 7/1 to 5Y 6/2) diatom-rich material. Bioturbation is more noticeable in the darker colored interbeds.

The intensity of burrowing is moderate to strong within the light-brown upper 4 m of sediment and particularly marked in the coarser-grained darker brown interbeds, the topmost of which includes *Skolithos* (Fig. 13). Open burrows are common in the top 10 m. Light gray, diatom-rich burrow fills are common between about 6–20 and 30 to 32 mbsf (Hole 849B). From about 36 to 53 mbsf, bioturbation is more apparent in relatively dark-colored, diatom-rich interbeds. Between 53 and 75 mbsf, zones of light-gray, diatom-rich burrow fill occur. Between 75 and 82 mbsf, bioturbation is more apparent in darker, more diatom-rich interbeds and *Zoophycos* occurs. Pyrite-rich burrow fill is scattered throughout the upper 100 m.

In the most diatom-rich sediments (between 115.5–125.2 mbsf, 164–176 mbsf, and from 220–237 mbsf) laminated beds appear free from bioturbation, although some have burrowed contacts with the surrounding lithology, particularly along the upper contact. Burrowing is moderate in the diatom nannofossil ooze between 100 and 275 mbsf. Where trace fossils are discernible, solid burrows (sometimes with purple "halos") and *Planolites* are most common, but *Chondrites* is also observed below 150 mbsf on relatively smooth core surfaces. Between 275–350 mbsf, bioturbation is moderate to heavy in the darker, diatom- and radiolarian-rich interbeds (Fig. 14). *Chondrites* and *Zoophycos* are common in Core 138-849C-32X (Fig. 15).

Diagenetic Features

Post-depositional gray (N5) and greenish-gray (5BG 7/1) color banding and laminations caused by sulfate-reduction organic matter diagenesis are common throughout most of the sequence, with the

Table 1. Summary of coring operations.

Core no.	Date (June 1991)	Time (UTC)	Depth (mbsf)	Length cored (m)	Length recovered (m)	Recovery (%)
138-849A-1H	8	0745	0.0–8.7	8.7	8.69	99.9
Coring totals				8.7	8.69	99.9
138-849B-1H	8	0855	0.0–6.7	6.7	6.76	101.0
2H	8	0950	6.7–16.2	9.5	8.93	94.0
3H	8	1045	16.2–25.7	9.5	9.01	94.8
4H	8	1150	25.7–35.2	9.5	9.77	103.0
5H	8	1245	35.2–44.7	9.5	10.05	105.8
6H	8	1345	44.7–54.2	9.5	9.84	103.0
7H	8	1450	54.2–63.7	9.5	10.06	105.9
8H	8	1555	63.7–73.2	9.5	9.89	104.0
9H	8	1700	73.2–82.7	9.5	10.09	106.2
10H	8	1800	82.7–92.2	9.5	9.79	103.0
11H	8	1900	92.2–101.7	9.5	9.96	105.0
12H	8	2005	101.7–111.2	9.5	10.03	105.6
13H	8	2110	111.2–120.7	9.5	9.89	104.0
14X	8	2210	120.7–130.3	9.6	4.46	46.4
15X	8	2305	130.3–140.0	9.7	9.41	97.0
16X	9	0000	140.0–149.7	9.7	9.53	98.2
17X	9	0055	149.7–159.3	9.6	9.74	101.0
18X	9	0145	159.3–168.5	9.2	9.44	102.0
19X	9	0235	168.5–177.7	9.2	9.73	106.0
20X	9	0325	177.7–187.3	9.6	9.46	98.5
21X	9	0420	187.3–197.0	9.7	9.31	96.0
22X	9	0510	197.0–206.6	9.6	9.65	100.0
23X	9	0600	206.6–216.3	9.7	9.74	100.0
24X	9	0700	216.3–226.0	9.7	9.82	101.0
25X	9	0755	226.0–235.7	9.7	9.25	95.3
26X	9	0855	235.7–245.3	9.6	6.30	65.6
27X	9	1000	245.3–255.0	9.7	9.66	99.6
28X	9	1055	255.0–264.7	9.7	9.68	99.8
29X	9	1155	264.7–274.3	9.6	9.68	101.0
30X	9	1255	274.3–283.9	9.6	9.56	99.6
31X	9	1350	283.9–293.6	9.7	9.79	101.0
32X	9	1450	293.6–303.2	9.6	9.77	102.0
33X	9	1600	303.2–312.9	9.7	9.86	101.0
34X	9	1715	312.9–322.6	9.7	9.74	100.0
35X	9	1825	322.6–332.2	9.6	9.88	103.0
36X	9	1930	332.2–341.8	9.6	9.81	102.0
37X	9	2120	341.8–350.5	8.7	6.44	74.0
Coring totals				350.5	343.78	98.1
138-849C-1H	10	2345	1.0–10.5	9.5	9.68	102.0
2H	11	0100	10.5–20.0	9.5	9.95	105.0
3H	11	0145	20.0–29.5	9.5	9.26	97.5
4H	11	0025	29.5–39.0	9.5	8.33	87.7
5H	11	0340	39.0–48.5	9.5	10.03	105.6
6H	11	0435	48.5–58.0	9.5	8.90	93.7
7H	11	0530	58.0–67.5	9.5	10.03	105.6
8H	11	0630	67.5–77.0	9.5	9.94	104.0
9H	11	0725	77.0–86.5	9.5	9.58	101.0
10H	11	0820	86.5–96.0	9.5	10.12	106.5
11H	11	0920	96.0–105.5	9.5	9.88	104.0
Coring totals				104.5	105.70	101.1
138-849D-1H	11	1115	4.0–13.5	9.5	4.36	45.9
2H	11	1205	13.5–23.0	9.5	9.47	99.7
3H	11	1255	23.0–32.5	9.5	9.79	103.0
4H	11	1350	32.5–42.0	9.5	8.98	94.5
5H	11	1440	42.0–51.5	9.5	9.90	104.0
6H	11	1535	51.5–61.0	9.5	9.42	99.1
7H	11	1630	61.0–70.5	9.5	9.93	104.0
8H	11	1720	70.5–80.0	9.5	8.70	91.6
9H	11	1815	80.0–89.5	9.5	9.76	103.0
10H	11	1905	89.5–99.0	9.5	9.55	100.0
11H	11	2000	99.0–108.5	9.5	9.90	104.0
12X	11	2105	108.5–115.5	7.0	8.81	126.0
13X	11	2200	115.5–125.1	9.6	8.58	89.4
14X	11	2245	125.1–134.8	9.7	9.47	97.6
15X	11	2340	134.8–144.5	9.7	9.61	99.1
16X	12	0030	144.5–154.1	9.6	9.70	101.0
17X	12	0120	154.1–163.3	9.2	9.74	106.0

Table 1 (continued).

Core no.	Date (June 1991)	Time (UTC)	Depth (mbsf)	Length cored (m)	Length recovered (m)	Recovery (%)
18X	12	0210	163.3–172.5	9.2	9.88	107.0
19X	12	0300	172.5–182.1	9.6	9.73	101.0
20X	12	0345	182.1–191.8	9.7	9.60	98.9
21X	12	0440	191.8–201.4	9.6	9.34	97.3
22X	12	0525	201.4–211.1	9.7	9.69	99.9
23X	12	0620	211.1–220.8	9.7	9.76	100.0
24X	12	0710	220.8–230.5	9.7	9.73	100.0
25X	12	0805	230.5–240.1	9.6	8.66	90.2
26X	12	0855	240.1–249.8	9.7	9.63	99.3
27X	12	0945	249.8–259.0	9.2	9.47	103.0
28X	12	1035	259.0–268.6	9.6	9.44	98.3
29X	12	1125	268.6–278.3	9.7	9.84	101.0
30X	12	1215	278.3–288.0	9.7	9.77	101.0
31X	12	1310	288.0–297.7	9.7	9.70	100.0
32X	12	1400	297.7–307.4	9.7	9.79	101.0
33X	12	1455	307.4–317.0	9.6	9.91	103.0
34X	12	1625	317.0–326.7	9.7	9.84	101.0
Coring totals				322.7	319.45	99.0

Table 2. Summary of logging operations.

Local day (June 1991)	Time (L)	Cumulative hours	Base of string (mbsf)	Comments
9	14:20	0.0		Last core on deck
9	16:45	2.4		Start rig up
9	18:35	4.2		Geophysical tool rigged up (NGT/SDT/HLDT/DIT/TLT); RIH
9	20:16	5.9	61.0	Start downlog, no heave compensator
9	20:45	6.4	350.2	Stopped downlog; at TD
9	20:58	6.6	350.2	At TD, start main log up (NGT/SDT/HLDT/DIT/TLT)
				Heave compensator not functioning. No heave comp for any run
9	21:45	7.4	149.7	Tool sticks in open hole; drop twice and come up to break free
9	22:05	7.8	71.9	Stop up log, go back to 172.5 mbsf for repeat section
9	22:10	7.8	172.5	Start repeat log up
9	22:22	8.0	71.9	End repeat section; close calipers and POOH
9	23:35	9.3		Geophysical tool string at wellhead
10	2:20	12.0		RIH w/ Geochemical String (NGT/ACT/GST) after ACT changeout
10	3:48	13.5	351.1	At TD; calibrate GST while moving up at 300'/hr
10	3:53	13.5	342.0	GST calibrated; drop back to TD
10	3:55	13.6	351.1	Start main log w/ Geochemical String from TD
10	5:40	15.3	50.3	Enter pipe and continue logging to mudline
10	5:55	15.6	0.0	Stop main log; POOH
10	7:00	16.7		Geochemical String at wellhead
10	8:10	17.8		RIH w/ FMS string (NGT/GPIT/FMS/TLT)
10	9:43	19.4	350.5	At TD start FMS repeat log
10	10:15	19.9	233.5	Stop repeat log; drop back to TD for main log
10	10:21	20.0	350.5	Start main FMS log at TD
10	10:50	20.5	111.6	Stop main FMS log
10	11:16	20.9		POOH FMS string
10	12:30	22.2		FMS string at wellhead
10	12:55	22.6		Rigged down from logging

exception of the intervals of nannofossil diatom ooze (Fig. 16). These color bands and laminations are usually parallel to the bedding plane and often crosscut burrows, indicating that diagenesis occurred after the sediments were buried below the bioturbated layer of the upper sediment column. The greenish-gray bands are often associated with higher magnetic susceptibility than the surrounding sediments.

A thin layer (3 cm) of silicified carbonate occurs at 237.2 mbsf in Hole 849B (Section 138-849-B-26X-2, 0 cm), and 235.1 mbsf in Hole 849D (Section 138-849D-25X-4, 10 cm, Fig. 17). This layer lies beneath an interval of thick interbeds of nannofossil diatom ooze and diatom nannofossil ooze. Below this silicified layer, from 237 mbsf through approximately 255 mbsf, is an interval of nannofossil ooze with low (less than 10%) diatom abundances. Pore-water geochemical data indicate that this layer may serve as a barrier to pore-water migration (see "Inorganic Geochemistry" section, this chapter). In

addition, this layer is marked by a steplike shift in the resistivity and velocity logs (see "Downhole Measurements" section, this chapter). Measurements of GRAPE density and wet-bulk density (see "Physical Properties" section, this chapter) also show a distinct anomaly across this layer across this boundary, from lower density above the silicified layer to higher density below. The typical carbonate and siliceous variations seen in the upper 230 m of the sediment column continue below this layer.

Summary of Lithology

While the dominant lithology at Site 849 is diatom nannofossil ooze, interbeds of a more siliceous diatom nannofossil ooze and nannofossil diatom ooze from 5 cm to 1 m thick are present throughout the sequence. Carbonate percentages are high but variable through most of the se-

quence. Both decimeter-scale and meter-scale variations are seen in the carbonate and silica content as demonstrated by GRAPE density, %CaCO₃ (Fig. 10), and digital color reflectance (Fig. 12).

BIOSTRATIGRAPHY

Sediments recovered from the four holes (849A to 849D) cored at Site 849 provide a continuous sedimentary record for the late Pleistocene through late middle Miocene. Calcareous nannofossils, foraminifers, radiolarians, and diatoms are generally present throughout the sequence and are used for developing the biostratigraphic framework (Tables 3 to 6; Fig. 18). Preservation of the calcareous nannofossils, radiolarians, and diatoms is generally moderate to good. The one exception is the lowermost portion (~10 m) of the sedimentary sequence that lacks siliceous microfossils. Preservation of the foraminifers is generally poor throughout the sequence.

The epoch boundaries are placed approximately as follows;

Boundary	Hole	Depth (mbsf)	Depth (mcd)	Event
Pleistocene/ Pliocene	849B	39.80–41.80	46.75–48.25	B *Gephyrocapsa oceanica* s.l.
	849C	39.13–39.80	47.28–47.95	
late/early Pliocene	849B	92.49–92.80	104.29–106.40	T *Reticulofenestra pseudoumbilicus*
	849C	90.50–90.90	108.15–108.35	
Pliocene/ Miocene	849B	165.80–167.30	190.75–192.25	T *Discoaster quinqueramus*
upper/middle Miocene	849B	320.96–322.30	359.86–361.20	B *Discoaster hamatus*

T = top occurrence; B = bottom occurrence.

The lowermost portion of the recovered sequence (Sample 138-849B-37X-CC) is placed in calcareous nannofossil Zone CN5b, indicating an age younger than 12.2 Ma. The stratigraphically lowest sample containing siliceous microfossils (138-849B-36X-CC) is assigned to the radiolarian *Diartus pettersoni* Zone and the diatom *Actinocyclus moronensis* Zone, indicating an age younger than 10.6 Ma.

The one core recovered from Hole 849A contains a microfossil assemblage characteristic of calcareous nannofossil Zone CN14b–CN15 (NN20–NN21) and the diatom *Pseudoeunotia doliolus* Zone. The following discussion focuses on biostratigraphic results from Holes 849B, 849C, and 849D.

Calcareous Nannofossils

Calcareous nannofossils recovered at Site 849 represent a stratigraphic sequence from the upper Pleistocene (Zones CN14b from Okada and Bukry, 1980, and NN20 from Martini, 1971) through the uppermost middle Miocene (Zones CN5b and NN7). Nannofossils are common to abundant and are generally well preserved throughout the Pleistocene-Pliocene section. Slight etching of some placoliths and moderate to strong overgrowth of discoasterids were observed in the Miocene assemblages. The nannofossil biostratigraphic events recognized at Site 849 are reported in Table 3.

The Pleistocene interval (Cores 138-849B-1H through -5H) is characterized by *Pseudoemiliania lacunosa, Calcidiscus* spp., different morphotypes of *Gephyrocapsa* spp., helicoliths, and ceratolithids. The first occurrence of *Gephyrocapsa oceanica* s.l. approximates the Pleistocene/Pliocene boundary and is placed between Samples 138-849B-5H-4, 60 cm, and -5H-5, 60 cm, and Samples 138-849C-5H-1, 13 cm, and -5H-1, 80 cm.

The Pliocene interval (Cores 138-849B-6H through -18X) is characterized by discoasterids, helicoliths, ceratolithids, different morphotypes of *Reticulofenestra* spp., and sphenoliths (in the lower Pliocene section). The last occurrence of *Reticulofenestra pseudo-*

umbilicus (top of Zones CN11 and NN14–15) approximates the upper/lower Pliocene boundary, and is recorded between Samples 138-849B-10H-CC, and -11H-1, 60 cm, and Samples 138-849C-10H-3, 100 cm, and -10H-3, 140 cm. Discoasterids and ceratolithids are rare to common throughout this interval.

The last occurrence of *Discoaster quinqueramus* (top of Zones CN9b and NN 11) approximates the Pliocene/Miocene boundary and is recorded between Samples 138-849B-18X-5, 50 cm, and -18X-6, 50 cm. *Discoaster quinqueramus* and *Discoaster berggreni* are rare and exhibit poor preservation through their entire stratigraphic range, which encompasses Zones CN9 and NN11.

The upper Miocene and the uppermost middle Miocene intervals (Cores 138-849B-19X through -37X) are characterized by moderately well-preserved assemblages. Discoasterids fluctuate in abundance but are generally rare throughout these intervals and show moderate to poor preservation, which prevented the identification of some species. Sphenoliths, helicoliths, and placoliths (such as *Reticulofenestra* spp., *Dictyococcites* spp., and *Coccolithus pelagicus*) are abundant and well preserved. The interval between Cores 138-849B-33X and -34X corresponds to the total range of *Discoaster hamatus* and has been placed in Zone CN7 (NN9). The occurrence of *D. hamatus* is recorded between Samples 138-849B-34X-6, 56 cm, and -34X-7, 40 cm. Within these two samples, the last occurrence of *Coccolithus miopelagicus* is recorded. This event approximates the upper/middle Miocene boundary. The interval below this event (Cores 138-849B-35X through -37X) is placed within Zones CN6 and CN5b (NN8 and NN7). It was not possible to obtain a more precise biostratigraphic assignment for this interval, owing to the absence of the biozonal marker *Catinaster coalitus*. However, the lowermost part of the sedimentary sequence at Site 849 (Core 138-849B-37X) was assigned to Subzone CN5b (Zone NN7), based on the presence of common specimens of *Discoaster kugleri* and *Discoaster musicus*.

Foraminifers

Planktonic foraminifers are few to common in Cores 138-849B-1H through -11H and rare to few through the remainder of the section. The preservation state of the foraminifers is poor throughout the sedimentary sequence. One exception is Sample 138-849B-21X-CC, in which common to abundant planktonic foraminifers are moderately well preserved. Samples 138-849B-33X-CC, -34X-CC, and -36X-CC are barren of foraminifers.

Throughout the entire sequence, radiolarians dominate the coarse-fraction residues, except in the two lowest cores (138-849B-36X and -37X), which contain abundant manganese micronodules. Other major components observed in the coarse-fraction residues include rare to few echinoid spines, sponge spicules, fish teeth, chert, and volcanic glass. Echinoid spines are absent from Cores 138-849B-33X through -35X, whereas sponge spicules are common. Chert fragments occur in Sample 138-849B-26X-CC. Volcanic glass is rare in Cores 138-849B-31X-CC and -32X-CC, and common below these samples for the remainder of the sequence.

Planktonic foraminifer datums identified in the sequence are given in Table 4. The zonal marker for Zone N22, *Globorotalia truncatulinoides,* occurs only in Core 138-849B-2H-CC, and the base of this zone was equated to the last occurrence of *Globorotalia limbata* in Sample 138-849B-7H-CC. The last occurrence of *Dentoglobigerina altispira* in Sample 138-849B-8H-CC indicates an age greater than 2.9 Ma for that level. The base of Zone N21 was equated to the last occurrence of *Sphaeroidinellopsis* spp. in Sample 138-849B-10H-CC. The first occurrence of *Globorotalia tumida* in Sample 138-849B-16X-CC approximates the base of the lower Pliocene zonal interval N19–N18. The first occurrence of *Globorotalia plesiotumida* in Sample 138-849B-30X-CC approximates the base of the upper Miocene Zone N17. The remainder of the sequence below Core 138-849B-30X-CC is unzoned.

Radiolarians

Radiolarians sampled at Site 849 range in age from the Quaternary (*Collosphaera tuberosa* Zone) to the late middle Miocene (*Diartus pettersoni* Zone, Table 5). The most recent radiolarian zone (*Buccinosphaera invaginata*) was not identified. The oldest material recovered that could be identified to the zonal level (*D. pettersoni* Zone) is from Sample 138-849B-36X-CC. Below this level, all samples were barren of siliceous microfossils.

Preservation and abundance of the radiolarians is generally good within the Pleistocene-Pliocene section. There is no clear indication of the reworking of older radiolarians into the younger part of the section. The Pleistocene-Pliocene section appears to be complete, with all the major zones and radiolarian datums recognized in the samples studied. Specimens of *Phormostichoartus fistula* are slightly more abundant in this section than in samples from previous sites; however, their very low abundance makes their last occurrence an unreliable datum for intersite correlations. Sufficient specimens of *Spongaster pentas* and *Spongaster berminghami* were found at this site to make useful comparisons with their previously published first and last appearance datums (Johnson et al., 1989), but their scattered occurrence in other Leg 138 sites to the south and east prevents them from being useful for correlation with these sites. The high accumulation rates in the lower Pliocene and upper Miocene greatly expand the *Phormostichoartus doliolum* and *Solenosphaera omnitubus* zones at this site, and most datums within this interval can be closely constrained. However, the occurrence of *Acrobotrys tritubus* is scattered, and its first and last appearances cannot be used as reliable datums.

Radiolarians were common to abundant throughout the middle to upper Miocene part of the section and preservation was generally good, except near the bottom of the recovered section (Core 138-849B-37X and the bottom part of Core 138-849B-36X). The deepest reliable datum (Table 5) is the last appearance of *Carpocanium cristata* (between Samples 138-849B-35X-5, 111 cm, and -35X-CC). This datum occurs within the middle part of the *Diartus pettersoni* Zone and has an age of 10 ($\pm$ 0.1) Ma within the tropical Indian and Pacific oceans (Johnson and Nigrini, 1985).

Diatoms

Common to abundant diatoms are generally present in the Quaternary through middle Miocene sediments recovered from Site 849. The exception is the interval containing the two deepest cores (138-849B-36X-CC and -37X-CC), which have either rare fragments or are barren of diatoms. Diatoms are generally moderate or well preserved with only a few intervals (138-849B-7H-2, 70 cm, through -8H-5, 70 cm, and -33H-CC through 35H-CC) containing poorly preserved specimens.

The diatom assemblage observed in samples from Site 849 is similar to that observed at other Leg 138 sites and permits recognition of the diatom zones from the Quaternary *Pseudoeunotia doliolus* through the upper Miocene *Actinocyclus moronensis* zones (Table 6). Cores 138-849A-1H, -849B-1H, -849C-1H, and -849D-1H are assigned to the *P. doliolus* Zone based on the occurrence of *P. doliolus* stratigraphically above the last occurrence of *Nitzschia reinholdii*. However, complete specimens of *N. reinholdii* are rare in the uppermost part of Holes 849B and 849C, allowing only tentative placement of the *P. doliolus/N. reinholdii* boundary. Fragments of *N. reinholdii* in Samples 138-849B-2H-CC and -849C-2H-CC suggest that this boundary occurs within the upper portion of Cores 138-849B-2H and -849C-2H. Complete specimens of *N. reinholdii* occur in Sample 138-849D-2H-CC, indicating that this zonal boundary also approximates the upper portion of Hole 138-849D-2H.

Samples 138-849B-2H-CC through -5H-4, 70 cm, -849D-2H-CC through -4H-CC, and Sample 138-849C-4H-CC are assigned to subzone B of the *N. reinholdii* Zone based on the co-occurrence of *P.*

doliolus and *N. reinholdii* stratigraphically above the occurrence of *Rhizosolenia praebergonii*. The last occurrence of *Nitzschia fossilis* is placed in the interval between Samples 138-849B-2H-CC and -3H-3, 70 cm, and -849D-2H-CC and -3H-CC. The interval from Samples 138-849B-5H-6, 70 cm, through -6H-3, 15 cm, is assigned to Subzone A of the *N. reinholdii* Zone based on the co-occurrence of *Rhizosolenia praebergonii* var. *robustus* and *P. doliolus*. The first occurrence of *P. doliolus* was placed between Samples 138-849B-6H-3, 15 cm, and -6H-5, 70 cm, and 138-849C-5H-CC and -6H-CC, and 138-849D-5H-CC and -6H-CC.

The last occurrence of *Thalassiosira convexa* has been placed between Samples 138-849B-7H-3, 60 cm, and -7H-CC and Samples 138-849D-6H-CC and 7H-CC, permitting the interval from Sample 138-849B-6H-5, 70 cm, through -7H-3, 60 cm, to be assigned to Subzone C of the *Rhizosolenia praebergonii* Zone. Samples 138-849B-7H-CC through -8H-2, 60 cm, are assigned to Subzone B of the *Rhizolosolenia praebergonii* Zone based on the co-occurrence of *R. praebergonii* and *Nitzschia jouseae* within this interval. The base of the *R. praebergonii* Zone is placed in Samples 138-849B-9H-2, 60 cm, -849C -7H-CC, and -849D-7H-CC. The intervening interval from Samples 138-849B-8H-4, 60 cm, through -9H-2, 60 cm, represents Subzone A of the *R. praebergonii* Zone. Samples from 138-849B-9H-4, 60 cm, through -16H-1, 70 cm, -849D-8H-CC, and -849D-16H-CC, are assigned to the *Nitzschia jouseae* Zone based on the continuous occurrence of *N. jouseae* and the absence of *R. praebergonii* throughout this interval.

Samples 138-849B-16H-CC through -24X-3, 60 cm, and -849D-16H-CC through -23X-CC are assigned to the *Thalassiosira convexa* Zone. This zone consists of three subzones. Unfortunately, the rare occurrence of *Thalassiosira miocenica* in the upper portion of this interval precludes recognition of the C/B subzonal boundary. The occurrence of *Thalassiosira praeconvexa* with *T. miocenica* and/or *Thalassiosira convexa* in Samples 138-849B-21X-5, 70 cm, through -24X-3, 60 cm, permit this interval to be assigned to Subzone A of the *T. convexa* Zone.

The intervals from Samples 138-849B-24X-6, 60 cm, through -28X-4, 60 cm, and -849D-24X-CC through -28X-CC were placed in the *Nitzschia miocenica* Zone. The co-occurrence of *Thalassiosira praeconvexa* and *N. miocenica* in the interval from Samples 138-849B-24X-6, 60 cm, through -26X-CC permits this interval to be placed in Subzone B of this Zone. Samples 138-849B-27H-2, 70 cm, through -28X-4, 60 cm, and -849D-26X-CC through -28X-CC are assigned to Subzone A of this zone.

The last continuous occurrence of *Thalassiosira yabei* was observed in Samples 138-849B-30X-5, 70 cm, and -849D-30X-CC, permitting samples for the interval from 138-849B-28X-7, 40 cm, through -30X-5, 70 cm, and Sample 138-849D-29X-CC to be assigned to the *Nitzschia porteri* Zone. Placement of the *N. porteri/T. yabei* zonal boundary between Samples 138-849B-30X-4, 70 cm, and -30X-5, 70 cm, and -849D-29X-CC and -30X-CC is supported by the first occurrence of *Nitzschia cylindrica* between Samples 138-849B-30X-4, 60 cm, and -30X-5, 70 cm, and 138-849D-29X-CC and -30X-CC.

The interval from Sections 138-849B-30X-5 through -33X-4 has been placed in the *T. yabei* Zone. The occurrence of *Thalassiosira burckliana* in Samples 138-849B-30X-CC and -31-CC, and 138-849D-30X-CC permits these samples to be assigned to Subzone B of this zone. The scattered occurrence of *T. burckliana*, however, prevents placement of the B/A subzonal boundary. The base of the *T. yabei* Zone is typically defined by the last occurrence of *Actinocyclus moronensis;* however, similar to *T. burckliana,* this species has a scattered occurrence, limiting its stratigraphic usefulness at this site. At Site 849, the base of the *T. yabei* Zone was tentatively placed at the last occurrence of *Denticulopsis hustedtii* in Sample 138-849B-33X-4, 55 cm. The uppermost occurrence of *A. moronensis* was observed in Sample 138-849B-35X-CC. Diatoms are scattered in Cores 138-849B-35X through -37X. In this interval, Sample 138-
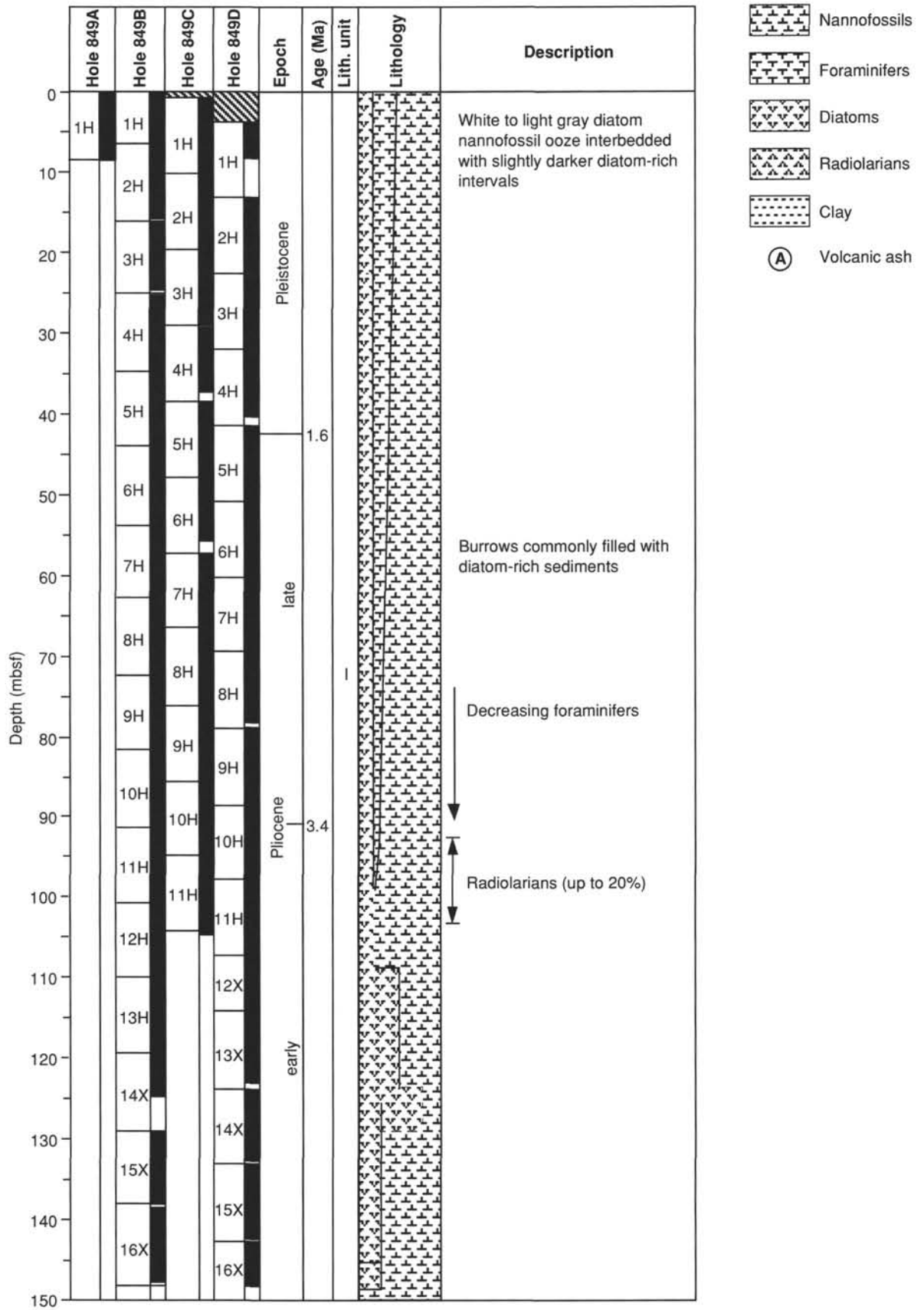
Figure 5. Lithostratigraphic summary of Site 849.
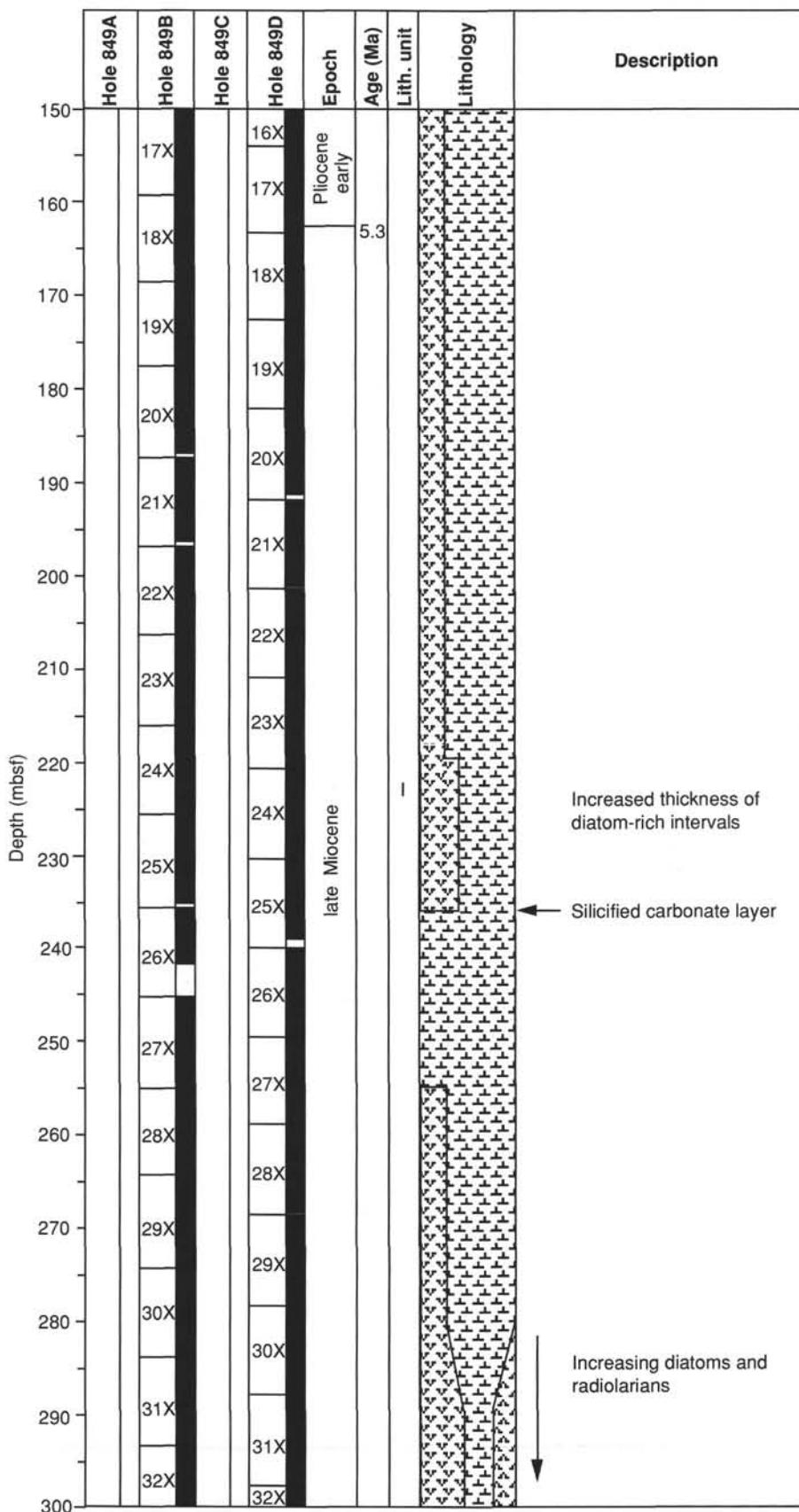
Figure 5 (continued).
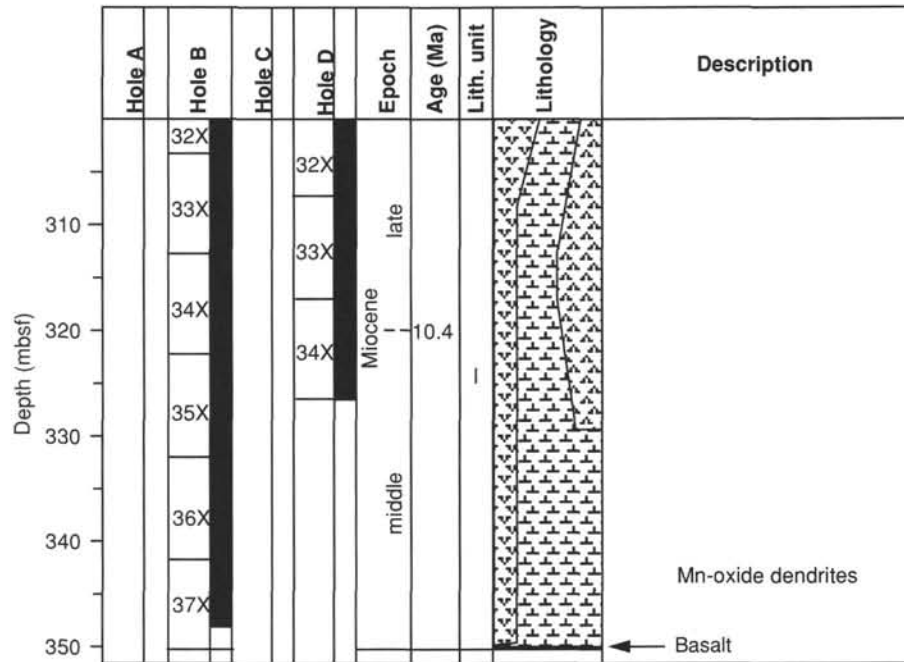
Figure 5 (continued).

849B-36X-6, 60 cm, is assigned to the *A. moronensis* zone based on the occurrence of *A. moronensis*, *Denticulopsis hustedtii*, and *T. yabei* without *Craspedodiscus coscinodiscus*.

PALEOMAGNETISM

The natural remanent magnetization (NRM) was measured for the APC cores from Holes 849A and 849B. The NRM intensity is between 1 and 10 mA/m, with a direction largely dominated by a steep upward component. The same cores were demagnetized to 15 mT. Additional demagnetization steps at 8 and 10 mT were performed on Sections 138-849B-1H-2 and -849B-1H-6, respectively.

Magnetic intensity decreases by more than a factor of ten at 4 mbsf in Hole 849B (Fig. 19). This level coincides with the brown to white color transition of the sediment (see "Lithostratigraphy" section, this chapter). Over this short interval, we observed coherent directions having a mean inclination of $5°$, in good agreement with the equatorial position of the site. Because no other interval having consistent directions was observed downhole, we did not measure intensity in Holes 849C and 849D.

Failure to observe a characteristic component of magnetization at this site is due to the low magnetization intensity. The remanence intensity signal of the sediments as measured on the pass-through magnetometer is similar to that of empty plastic core liners (see Sites 846 and 847) and proved also to be within the noise level of the Molspin magnetometer. Below 4 mbsf, a sharp decrease also occurred in the parameter M(15)/NRM, the ratio of 15-mT demagnetized remanence to NRM (Fig. 19), which is a measure of the coercivity of the remanence. If we assume that the magnetic mineralogy is dominated by magnetite, this decrease in the M(15)/NRM ratio indicates significant stabilities above 4 mbsf. Additional studies are necessary to determine the origin of the magnetic minerals and whether diagenetic processes have resulted in the dissolution of most of the magnetic minerals.

The bulk susceptibility also decreases below 4 mbsf from values of 2 to 4×10^{-5} SI to a mean value of 0.2×10^{-5} SI. Below 4 mbsf, the susceptibilities are mostly in the range of -0.5 to 0.5×10^{-5} SI. Thus, it was difficult to distinguish the sedimentary signal from the drift of the instrument (which can reach 1×10^{-5} SI) and from the susceptibility of the core liner (which can vary from -0.4 to 0.6×10^{-5}). Although identical features seem to correlate well from hole to hole, detailed correlations based on susceptibility alone would be problematic at this site.

SEDIMENTATION RATES

A sedimentary section nearly 400 m thick covering the time interval from the late Pleistocene to the bottom of the late Miocene was recovered at Site 849. Biostratigraphic age control was provided by all four of the chief planktonic microfossil groups.

The composite depth section for Site 849 is given in Table 7. This composite was formed by comparing shipboard measurements of GRAPE and percent reflectance (from the automated color analyzer) at adjacent holes. (Magnetic susceptibility measurements from adjacent holes were not used to form the composite section at this site.) These comparisons were then integrated to form a single composite depth section for the site (a detailed discussion on the construction of composite sections during Leg 138 is presented in Hagelberg et al., this volume).

For the holes and cores listed in Column 1 of Table 7, Column 2 gives the ODP sub-bottom depth of each core's top and bottom (in meters below seafloor, or mbsf). Note that the depth given in Column 2 corresponds to the depth of the bottom of the recovered core. This depth places the core-catchers in their correct positions in the composite depth section and is not the same as the standard ODP core-catcher depth. Column 3 shows the length of core recovered. Column 4 gives the composite depth of each core's top and bottom (in meters composite depth, or mcd). Column 5 indicates the amount of offset between the ODP depth and the composite depth. ODP sub-bottom depth can be converted to composite depth by adding the offset listed in Column 5 for the appropriate core.

Both GRAPE density and percentage of reflectance data produced records having high amplitudes and variability through much of the section in Holes 849A (1 core), 849B, 849C, and 849D at Site 849 (Fig. 20, back pocket). Magnetic susceptibility data were of low amplitude through much of the sequence, and in the XCB-cored

section problems with contamination was found (possibly from the drill pipe). This site was double-cored to basement at two holes (Holes 849B and 849D), with the objective of producing a continuous section with overlap to basement. In the XCB-cored section, both GRAPE and color data were sufficient to correlate these two holes down to basement at 388.09 mcd.

Analysis of the composite section indicates that overlap of adjacent holes was maintained down through all of the APC-cored interval (13 cores) and most of XCB-cored interval (22 cores) at Site 849. In the XCB-cored section, overlap was not maintained in only four locations: between Cores 138-849B-14X and -849D-14X, -849B-26X and -849D-26X, -849B-27X and 849D-27X, and -849B-30X and -849D-30X. In one location, between Cores 138–849B-26X and -849D-26X, comparison with the composite depth section at Site 846 indicated that at least 1.5 m of sediment was missing between these two cores. However, the composite depth section for Site 849 was not adjusted on the basis of this information from Site 846, because the integration of composite records between sites has been left for a more detailed study. When no overlap between adjacent holes was demonstrated, core depths were adjusted so as to leave no gap between cores.

Developing a satisfactory sedimentation rate record for Site 849 was hampered by the absence of a paleomagnetic record. However, all four microfossil groups provided good biostratigraphic information in different parts of the record. Table 8 gives the control points selected to generate the age-depth plots shown in Figure 21 (A–D). To generate a meaningful sedimentation rate plot it was necessary to use closely-spaced datums. The depth of 175.3 mcd was assigned the age 4.3 Ma; this is the shallowest sample containing the diatom *Nitzschia cylindrica*. This is the best constraint on the age-vs.-depth plot near the point where a marked change occurs in sedimentation rate, as neither the upper limit of *Amaurolithus delicatus* nor that of *Ceratolithus acutus* could be determined accurately at Site 849. At 278.5 mcd, the first appearance of *Amaurolithus primus* was used, but with an age of 6.42 Ma. The accepted age for the first appearance of this species is 6.7 Ma (see "Explanatory Notes" chapter, this volume). However, at Site 848, where paleomagnetic control is excellent, the first appearance is clearly later than this and may be estimated by interpolation at 6.42 Ma. To obtain sedimentation rates that are consistent through the western transect of Leg 138 sites, we have used the age as estimated at that site. At the bottom of the section, the nannofossil assemblage in Sample 138-849B-37X-CC has been assigned to Zone CN5b (i.e., older than 11.5 Ma) despite absence of the marker species *Cyclicargolithus floridanus*. The diatom marker species *Craspedodiscus coscinodiscus* is not present, implying an age of less than 10.6 Ma. The sample has been arbitrarily assigned an age of 10.5 Ma. Sedimentation rates vs. age (Fig. 22) and vs. depth (Fig. 23) are relatively constant, at around 30 m/m.y. from the Pleistocene through most of the Pliocene. In the basal Pliocene the rate is much higher; using biostratigraphic control the rate appears to be near 100 m/m.y. between about 4.3 and 5.0 Ma. The timing of the termination of this high accumulation rate interval is the same as was documented with more precise time control by magnetostratigraphy at Site 848. The pattern of change in rate is somewhat similar to that at Site 848 in the lower part of the section; differences, however, may be an artifact of the different degree of time control in the lower section.

INORGANIC GEOCHEMISTRY

Nineteen interstitial-water samples were collected at Site 849, three from Hole 849A at depths ranging from 1.5 to 7.5 mbsf and 16 from Hole 849B from 23.7 mbsf to just above basement at 346.3 mbsf (Table 9). Results from these two holes are considered to constitute a single depth profile in this report.

An interstitial water sample was taken from Sections 1, 3, and 5 of the solitary core making up Hole 849A. Core 138-849A-1H consisted of clayey foraminifer nannofossil ooze with diatoms through Section 138-

849A-1H-3 (see "Lithostratigraphy" section, this chapter). Below this section there is a shift in the dominant lithology to a light-gray clayey diatom nannofossil ooze with foraminifers.

Interstitial-water sampling in Hole 849B began with a sample from the third core (Sample 138-849B-3H-5), composed of white nannofossil ooze with diatoms and foraminifers. One interstitial water sample was taken from every third core through Core 138-849B-30X; every core was sampled below this depth. The sediments in these upper sections consisted of variations on nannofossil ooze.

A chert layer 2 to 3 cm thick occurs at the top of Section 138-849B-26X-2 (237 mbsf). The same deposit was resampled in Hole 849D (Section 138-849D-25X-4), the only other hole at this site to reach this depth. From XRF analyses of subsamples from these holes, we determined that this chert contains 7% to 11% calcium by weight. An irregular offset occurs in some of the pore-water profiles at the depth of this layer (Figs. 20, 21, and 22), indicating that this chert deposit acts as a semi-impervious barrier between higher porosity sediments above and lower porosity sediments below, as seen in measurements of GRAPE density, porosity, and water content (see "Physical Properties" section, this chapter). This transition is recorded as a steep, relatively high-amplitude break in the velocity log of Hole 849B (see "Downhole Measurements" section, this chapter).

Downhole indications of hydrothermal influence begin to appear in Core 138-849B-34X as dark banding and increased magnetic susceptibility. Darker sediments continue to be a minor component of the lithology down through Section 138-849B-36X-5, which also contains manganese oxide dendrites. The next and deepest core at this site (Core 138-849B-37X), contains manganese dendrites throughout and is characterized as oxide-rich nannofossil ooze with foraminifers (see "Lithostratigraphy" section, this chapter).

The smell of H_2S became noticeable in Core 138-849B-15X and increased through Core 138-849B-21X. The H_2S odor diminished below this depth, becoming faint by Core 138-849B-24X and unnoticeable by Core -849B-27X.

The chemistry of interstitial water at Site 849 (Table 9) is influenced by crystallization and diagenesis; alteration of crust seems to be less important than at other Leg 138 sites. Diffusive transport of some parameters at Site 849 is disrupted by the layer of diagenetic carbonate at 237 mbsf. This layer effectively seals off the bottom 100 m of sediment creating two sediment columns with somewhat different water chemistries. This shift in chemistry can be seen clearly in concentration-depth profiles of alkalinity (Fig. 24C), sulfate (Fig. 24D), calcium (Fig. 25B), strontium (Fig. 26B), and ammonia (Fig. 26C); those parameters most strongly influenced by diagenesis and recrystallization. This barrier also has a dramatic effect on the profile of methane at this site (see Organic Geochemistry section, this chapter). It is useful to consider these profiles as consisting of two zones separated at 237 mbsf. This approach is illustrated in Figures 27, 28, and 29.

Sodium (Fig. 27A) and chloride (Fig. 27B) concentrations do not change downcore or across the layer at 237 mbsf. This monotonous distribution indicates that these elements are not being produced or consumed in either zone. Deviations from simple burial can be accommodated within analytical uncertainties.

Profiles of alkalinity (Fig. 27C) and sulfate (Fig. 27D) are most easily explained as two distinct zones. Above 237 mbsf, microbial degradation of organic matter consumes sulfate, producing alkalinity (Claypool and Kaplan, 1974) that generates concave-downward and concave-upward profiles for sulfate and alkalinity, respectively. The downhole variations in sulfate production predicted by this analysis are consistent with the odorous record of H_2S. Below 237 mbsf, both parameters display linear trends to seawater values at basement.

Even the most reducing interstitial water at Site 849 is only mildly anoxic. Alkalinity in truly reducing sediments (i.e., 0 sulfate) can reach levels that are 10-fold higher than the highest concentration found at this site, such as those sampled by Harrison et al. (1982) at Sites 496 and 497 on the Middle America Trench slope during DSDP Leg 67.
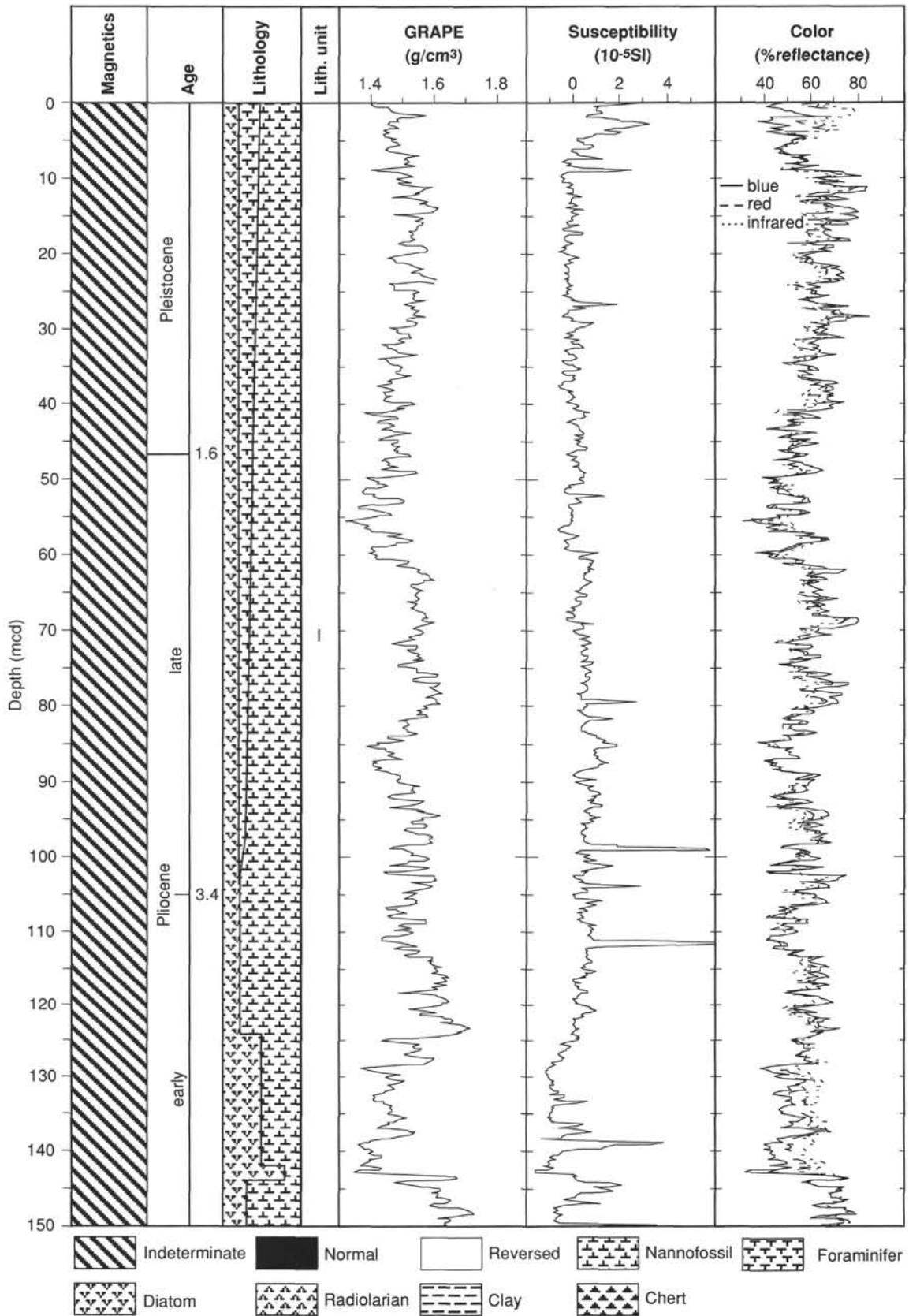
Figure 6. Composite summary of magnetics, age, graphic lithology, GRAPE density, magnetic susceptibility, and color reflectance for Site 849. Composite data consist of sections spliced together from multiple holes drilled at the site. Data are shown plotted vs. meters composite depth (mcd), the new depth scale used when constructing composite sections. GRAPE, susceptibility, and color data have been smoothed using a 20-point Gaussian filter.
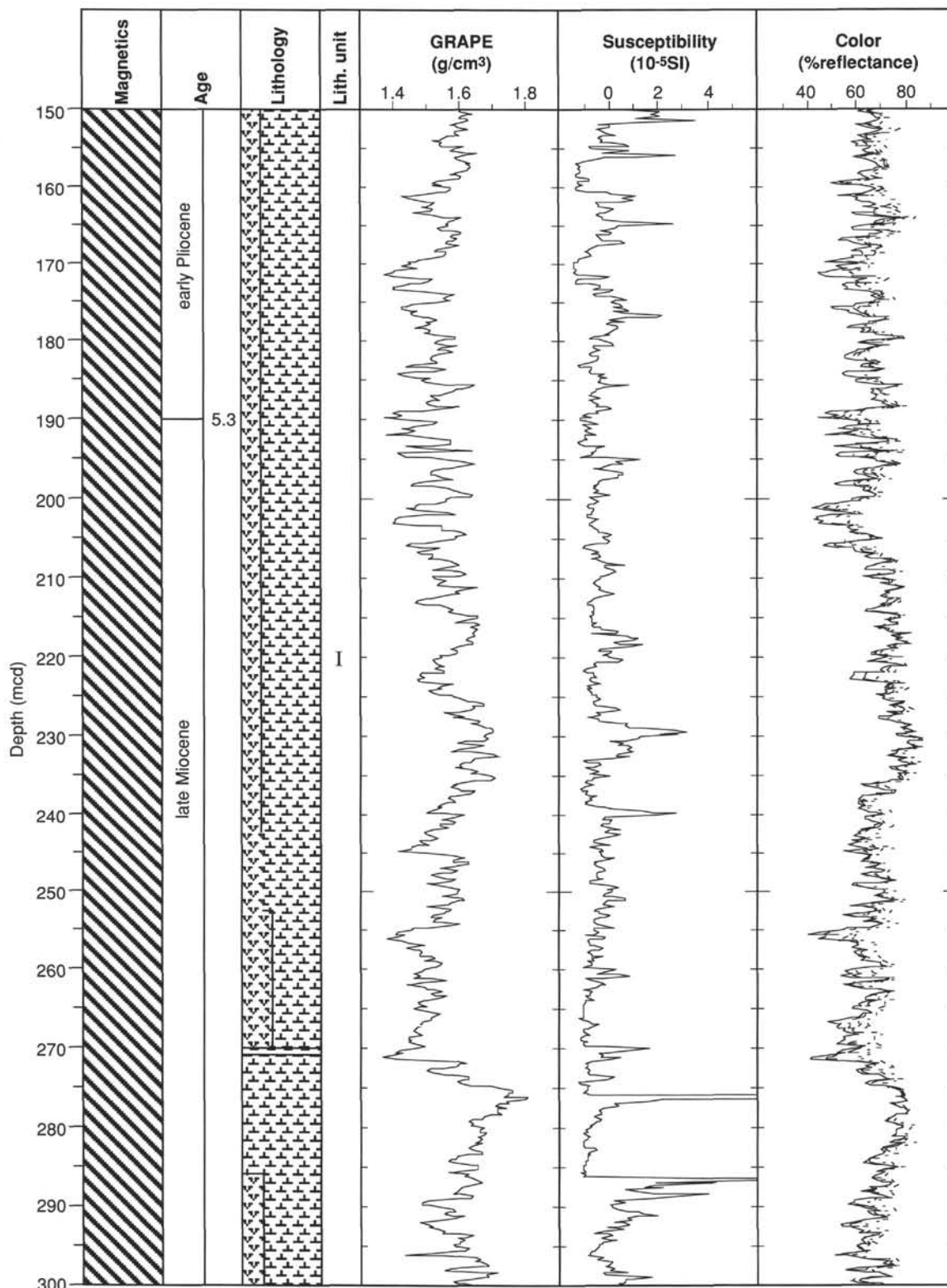
Figure 6 (continued).
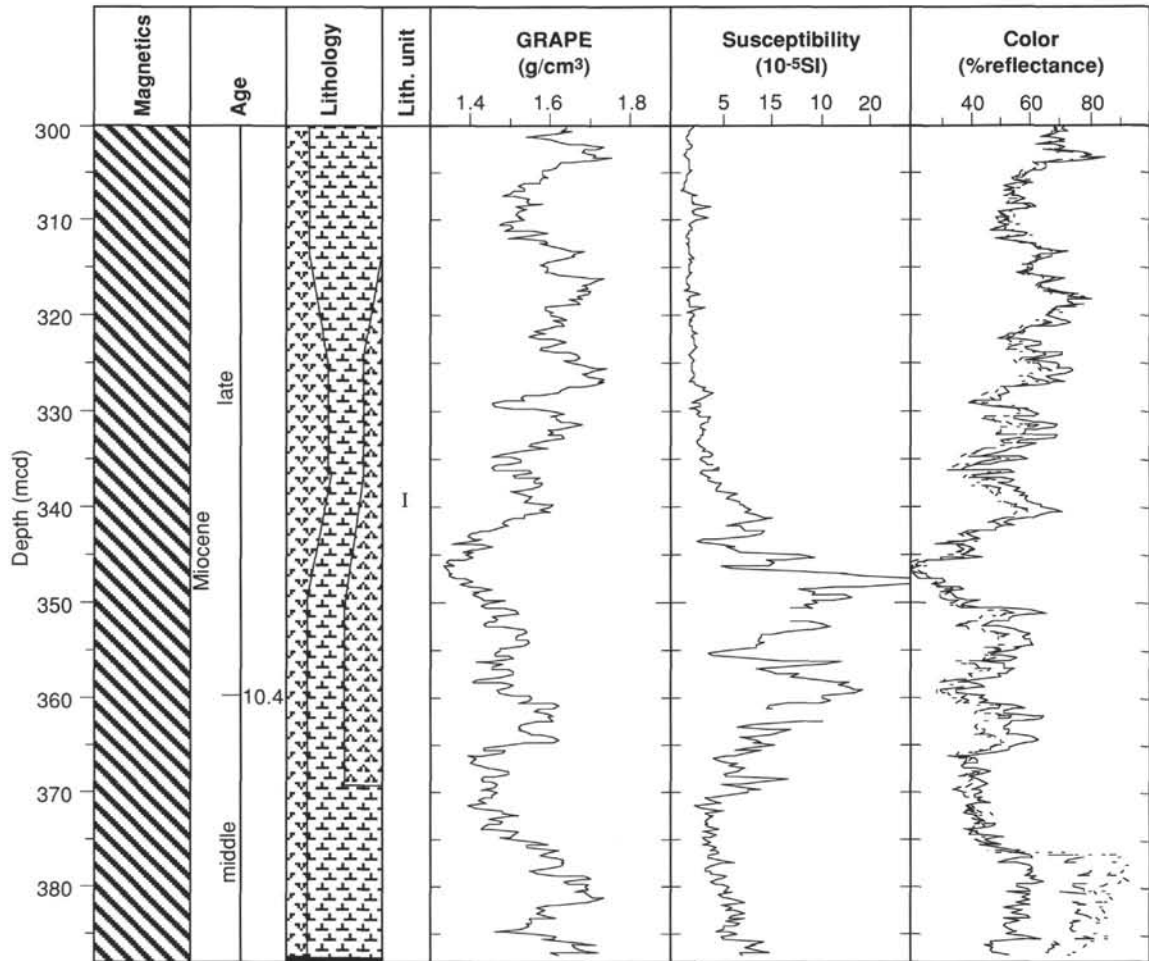
Figure 6 (continued).

Ammonia displays the greatest change across the 237 mbsf boundary (Fig. 29C), decreasing six-fold across this interval (Table 9). Ammonia is clearly being produced by microbial activity above the layer, but behaves more-or-less conservatively below.

Potassium (Fig. 28C) is statistically invariant downcore. Magnesium (Fig. 28A) and calcium (Fig. 28B), on the other hand, decrease downcore in the upper sections of the hole. Such changes occur when alkalinity is produced by microbial activity (Fig. 27C) initiating the precipitation of carbonate phases. The calcium-rich, chert layer at 237 mbsf appears relict in this view as this depth is not the focal point of calcium diagenesis at the present time.

Silica displays a regular increase with depth, which is consistent with reaction with biogenic silica (Kastner, 1981; Gieskes, 1974). There is a small maximum centered at 170 mbsf but no indication of substantial interaction with the layer at 237 mbsf or basement. This also suggests that the layer at 237 mbsf is inert, a fossil layer imposing physical constraints but not acting as a zone of reaction.

The strontium profile at this site (Figs. 26B and 29B) is similar to the strontium profile for nearby Site 572, as reported by Stout (1985). The increasing trend of strontium with depth observed at these and many other sites is known to be produced by recrystallization of biogenic calcite (Elderfield and Gieskes, 1982; Baker et al., 1982; Gieskes et al., 1986; Baker, 1986). The shape of the concentration-depth profile of lithium (Figs. 26A and 29A) in the upper sections of this hole suggests that this element is being removed by this same process, which is consistent with profiles of interstitial lithium re-

corded at other sites on this leg. In general, however, lithium geochemistry in deep-sea sediments is apparently more complex than these observations would imply, as it behaves quite differently at other DSDP/ODP sites (Gieskes, 1983). In fact, at this site, lithium and strontium seem to be decoupled below 237 mbsf.

In summary, a layer of diagenetic carbonate at 237 mbsf acts as an effective physical barrier, disrupting diffusive communication. The presence of this layer affects the concentration-depth profiles of alkalinity, sulfate, ammonia, calcium, and strontium. Profiles of alkalinity, sulfate, and ammonia are controlled by diagenesis above this layer and by diffusion below. Increasing alkalinity in the top sections, driven by microbial degradation of organic matter, precipitates carbonates and removes interstitial magnesium and calcium. Recrystallization of biogenic calcite above 200 mbsf releases strontium to the pore waters. This process also seems to remove dissolved lithium.

ORGANIC GEOCHEMISTRY

Carbonate and Organic Carbon

Concentrations of inorganic and organic carbon were measured in Hole 849B following the methods outlined in the "Explanatory Notes" chapter (this volume). From the inorganic carbon data, we calculated the weight percent of calcium carbonate ($\%CaCO_3$). Percentage of organic carbon ($\%C_{org}$) was determined in approximately two samples per core in Hole 849B. To determine concentrations of C_{org}, we measured the amount of carbon in the dried residues from Coulometer analyses after treatment with 2N HCl (see "Explanatory Notes" chapter,
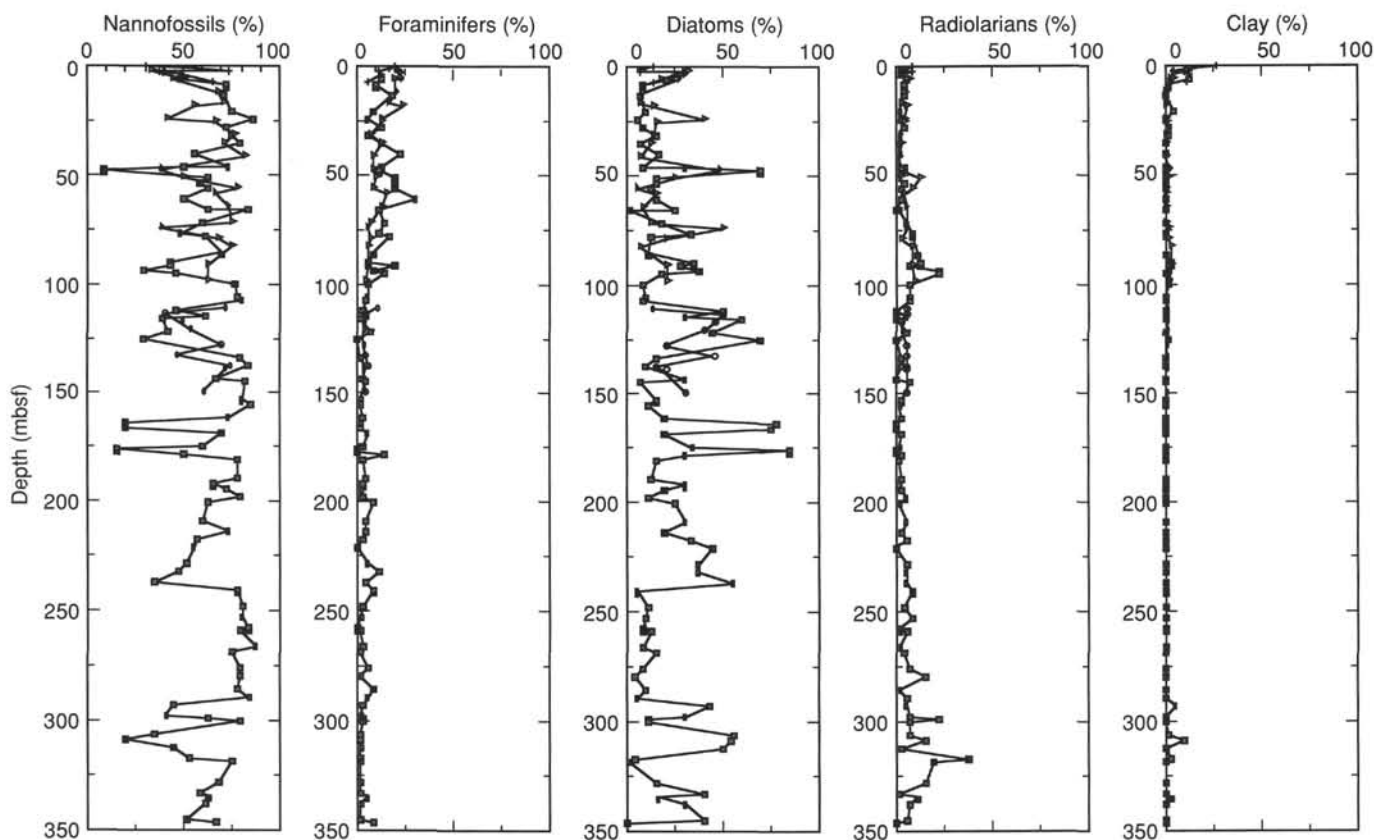
Figure 7. Summary of major-component smear slide data from Site 849. Hole 849 = crosses; Hole 849B = squares; Hole 849C = circles; Hole 849D = triangles.

this volume) to optimize results in sediments low in C_{org} and high in carbonate. The analytical results are listed in Table 10 (CD ROM, back pocket) with respect to both ODP depth (mbsf) and to composite depth (mcd; see "Sedimentation Rates" section, this chapter). Should a duplicate analysis be performed on a given sample, the mean value of the original analysis and the duplicate have been listed in Table 10 (CD ROM, back pocket). Duplicate %CaCO_3 analyses are listed in Table 11. The results indicate a reproduceability of 0.9%.

Figure 30 shows %CaCO_3 and %C_{org} in Hole 849B vs. depth (mbsf). Figure 31 shows %CaCO_3 and %C_{org} vs. composite depth and age, based on datum levels identified at Site 849 (see Sedimentation Rates and Paleomagnetism sections, this chapter). The %CaCO_3 record at Site 849 shows generally high values (near 75%) that are punctuated by several intervals of significantly lower %CaCO_3 (near 40%) (Fig. 30). All of the low %CaCO_3 intervals coincide with increased diatom percentages based on smear slides (see Lithostratigraphy section, this chapter), and most intervals are characterized by increased C_{org} content. A low %CaCO_3 interval around 310 mbsf (9 Ma) at Site 849 is approximately coeval with low carbonate intervals observed at other sites drilled during Leg 138. This interval has been interpreted as a severe carbonate dissolution event based on the poor preservation of calcareous nannofossils (see "Biostratigraphy" section, this chapter).

Accumulation Rates

Following the methodology outlined in the "Explanatory Notes" chapter (this volume), we calculated the average values of several sedimentary parameters in time intervals delimited by the chronostratigraphic levels discussed in the "Sedimentation Rates" section (this chapter). The average values of %CaCO_3, %C_{org}, linear sedimentation rate (LSR), dry-bulk density (DBD), bulk-sediment mass accumulation rate (bulk MAR), CaCO_3 MAR, and C_{org} MAR for 12

time intervals since 10.5 Ma are listed in Table 12. The mean values are presented vs. composite depth in Figure 32 and vs. age in Figure 33. Superimposed on the mean values are estimates of the instantaneous MAR calculated for each sample. The mean accumulation rates of bulk sediment reach up to 8 g/cm²/k.y. in the period from 8 to 4 Ma at Site 849, but do not exceed 2 g/cm²/k.y. in either the middle and lower Miocene or the Pleistocene. These rates are significantly higher than those encountered at Site 848 (maximum of 1.5 g/cm²/k.y.), where rates were highest in the time interval from 7 to 4 Ma. However, in contrast to Site 848 on the western transect, Site 849 lacks the increase in Pleistocene MARs. Despite low %C_{org}, the high sedimentation rates result in C_{org} accumulation rates that are comparable to those of Sites 845 and 846 (up to 10 mg/cm²/k.y.) on the eastern transect.

Gas Geochemistry

We took samples for gas analysis from each core of Hole 849B. Gas was released from a sediment sample (about 5 cm³) by thermal desorption (i.e., the headspace technique; see "Explanatory Notes" chapter, this volume) and the measured concentrations of hydrocarbons in the headspace volume (in ppm) were converted to μL/L of sediment. The results are shown plotted vs. depth in Figure 34 and are reported in Table 13 (CD-ROM, back pocket). Methane concentrations do not exceed 50 μL/L sediment; ethane and higher hydrocarbon gases are below detection limits. An intriguing feature of the methane concentration curve with depth (Fig. 34) is the steady increase in sorbed methane concentrations to a depth of approximately 230 mbsf, below which level concentrations per volume sediment decrease dramatically. A silicified calcareous concretion was observed in Section 138-849B-26X-2 (see "Lithostratigraphy" section, this chapter) at the depth interval that separates the two
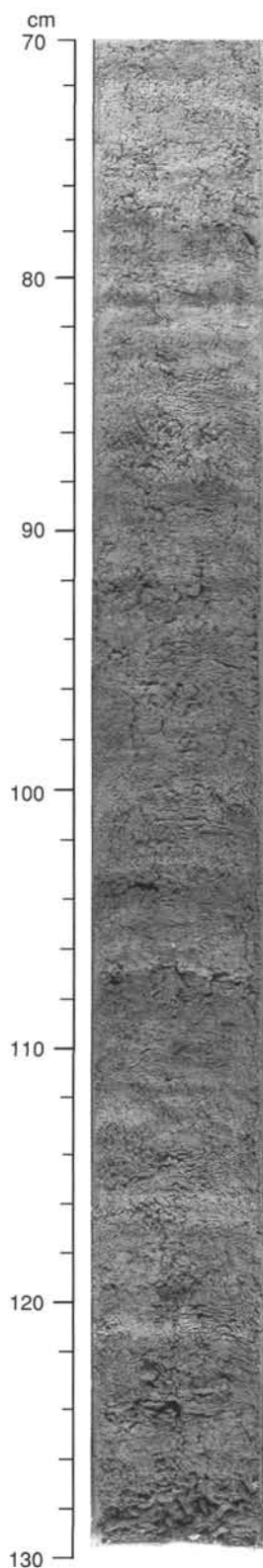
Figure 8. Diatom-rich interval from Section 138-849B-14X-3 at 70–130 cm. *Thalassiothrix longissima* is present throughout this interval.

distinctly different regimes of methane concentrations. A lithified layer yielding such concretions may exert a significant influence on the gas and pore-water geochemistry (see "Inorganic Geochemistry" section, this chapter). The shapes of the ammonia and methane concentration profiles (as well as those of other components involved in diagenesis) suggest that either diagenesis does not proceed in the sedimentary column under the silicified calcareous layer, or that the diagenetically produced cemented layer separates two distinctly different pore-water (and diagenetic) regimes. The methane concentration gradient between samples immediately above and below the silicified calcareous concretion is significant and suggests that the concretions near 232 mbsf may be impeding diffusion and mass exchange between the intervals above and below. The concentration gradient across the silicified calcareous layer also implies that it is of some lateral extent and thus cannot be nodular.

PHYSICAL PROPERTIES

Introduction

Physical properties measured on whole-round samples for cores recovered at Site 849 included GRAPE bulk-density, compressional-wave velocity (using the multisensor track, MST), and thermal conductivity. Measurements on split-cores included (1) index properties: wet-bulk density, dry-bulk density, water content, and porosity, (2) compressional-wave velocity using the digital sonic velocimeter (DSV), and (3) vane shear strength using the Wykeham-Farrance vane shear device. In Hole 849B, index properties, compressional-wave velocity, and vane-shear strength were measured twice per section in the APC-cored interval. In the XCB-cored intervals, index properties and compressional-wave velocity were measured twice per section, but vane-shear strengths were not measured. Thermal conductivity was measured for four sections (Sections 1, 3, 5, and 6 or 7) per core in Hole 849B. In Hole 849C, compressional-wave velocities and index properties were measured once per section in APC cores. Index property measurements were always taken at the same depth interval as those of velocity. The methods of analyses are described in the "Explanatory Notes" chapter (this volume).

Index Properties

The index property profiles are highly variable, reflecting the variation between calcareous and siliceous sediments described in the "Lithostratigraphy" section (this chapter). Wet-bulk density (Fig. 35; Table 14, CD-ROM, back pocket) ranges from 1.26 to 1.76 g/cm^3 and increases slightly with depth. Grain density (Fig. 36; Table 14, CD ROM, back pocket) ranges from 2.24 to 2.76 g/cm^3; water content (Fig. 37; Table 14, CD ROM, back pocket) from 52% to 227%; and porosity (Fig. 38; Table 14, CD ROM) from 58% to 85%. Both the water content and porosity decrease with depth.

Compressional-Wave Velocity

Compressional-wave velocity (Fig. 39; Table 15, CD-ROM, back pocket) was measured perpendicular to bedding and ranges from 1495 to 1606 m/s. In the upper 112 m of the sedimentary section, compressional-wave velocities generally increase with depth. A decrease in velocity occurs at 119.5 mbsf, where the compressional-wave velocity is offset by approximately 30 m/s. This offset occurs at the depth where XCB-coring began. From 119.5 to 338 mbsf, compressional-wave velocity again increases steadily with depth until 338 mbsf, where a sharp increase occurs.
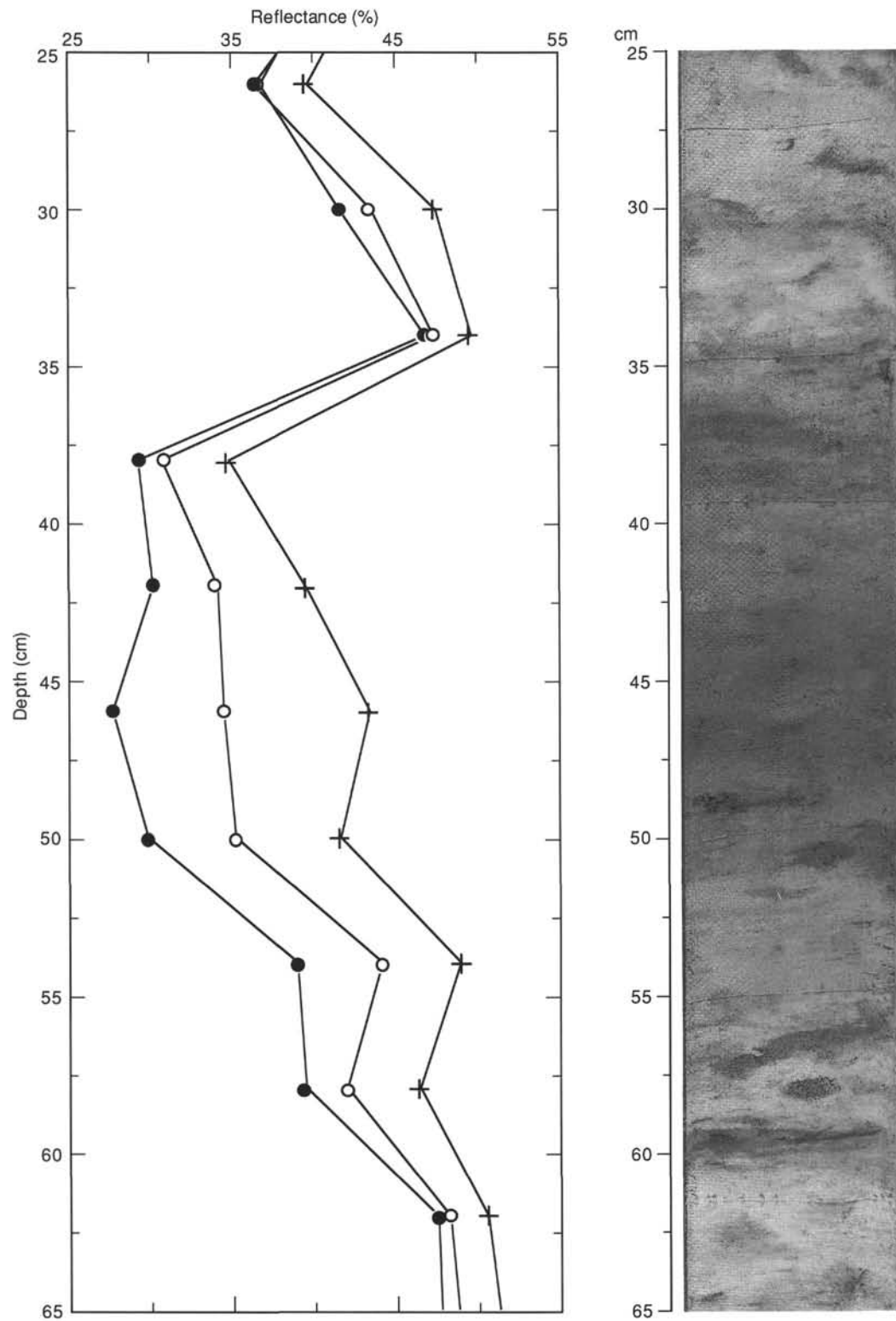
Figure 9. Example of digital color reflectance variation (left) associated with lithologic change (right) from Section 138-849B-6H-3 at 25–65 cm. Darker sediments show lower reflectance in near-infrared (crosses), red (open circles), and blue (filled circles) bands. Contact between more nannofossil-rich sediments (light colored) and more diatom-rich sediments (dark colored) is gradational.
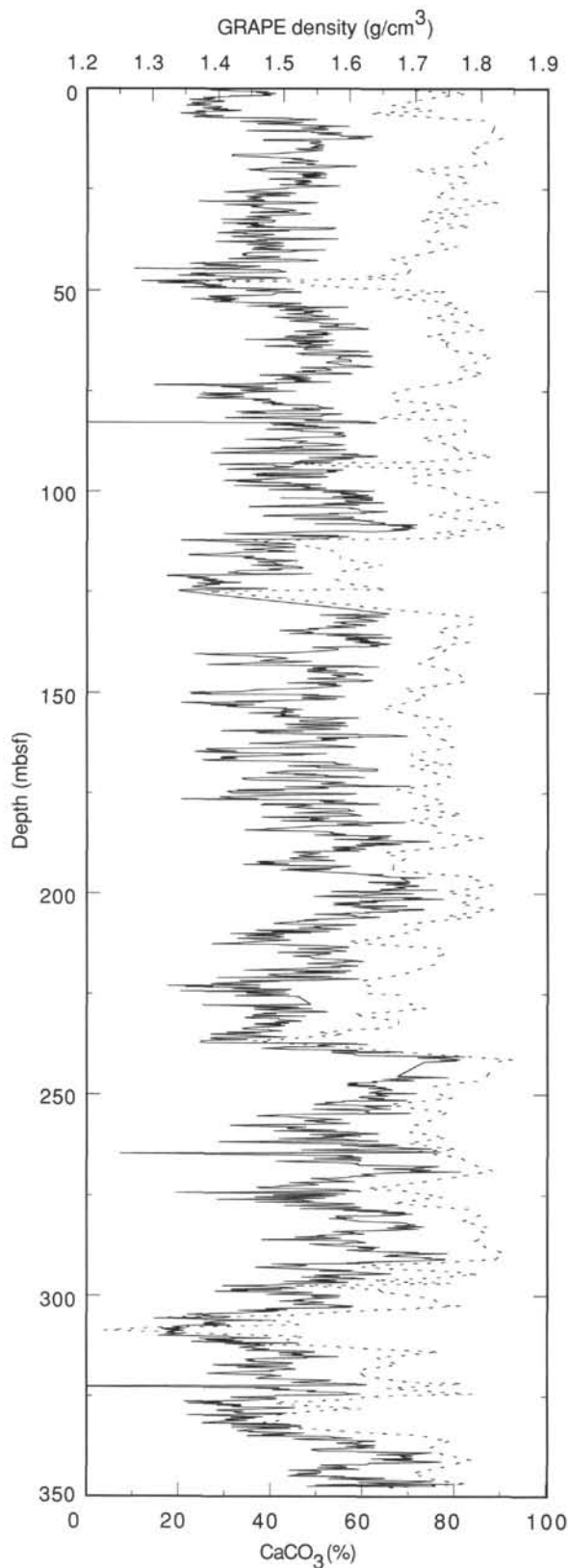
GRAPE density (g/cm³)

Figure 10. CaCO₃ (dashed line) and GRAPE density records (solid line) from Hole 849B, showing the level of carbonate variability throughout the sedimentary sequence.

Higher compressional-wave velocities occur in the intervals from 112 to 119 mbsf and from 308 to 312 mbsf. These siliceous-rich intervals (50% diatoms) have high porosity and low wet-bulk density values. The upper high velocity zone (112–119 mbsf) also has high shear strength values (>50 kPa). In contrast, the *in-situ* log velocities (see "Downhole Measurements" section, this chapter) are lower in these siliceous sediments. This difference indicates that the removal of sediment overburden affects the calcareous sediments more than the siliceous sediments. The high compressional-wave velocities at 338 mbsf are associated with calcareous sediments that contain 30% to 40% diatoms and are characterized by high wet-bulk density and low porosity.

Thermal Conductivity

Thermal conductivity (Fig. 40; Table 16, CD-ROM, back pocket) is highly variable and ranges from 0.77 to 1.46 W/(m • K). As thermal conductivity is a function of the density and water content of the sediment, the highly variable nature of the thermal conductivity profile reflects the downhole variation in calcareous and silicious sediments.

Shear Strength

Undrained shear strength (Fig. 41; Table 17, CD-ROM, back pocket) values range between 3.3 and 109.1 kPa and generally increase with depth below the seafloor. Shear strength increases steadily from 0 to 48 mbsf. From 48.0 to 52.3 mbsf, a sharp increase in shear strength values takes place, and then becomes highly variable from 70 mbsf to the base of the APC-cored interval (or 120 mbsf). The variability in shear-strength values results from numerous rapid changes in lithology from siliceous diatom ooze to calcareous nannofossil ooze. Peak shear strength values at 52.3 mbsf, 93.2 to 99.2 mbsf, and 112.3 mbsf occur in siliceous sediments containing up to 70% diatoms, and high shear-strength values between 92.3 and 99.2 mbsf occur in radiolarian-rich (25%) sediments. The marked low in shear strength values between 105 and 111 mbsf occurs in calcareous-rich sediment (75%–80% nannofossils).

Relationships of Physical Properties to Lithology

The results from Site 849 indicate that the downhole distribution of physical properties is controlled by normal compaction processes and sediment type. A comparison of the physical properties to the sedimentary section reveals that the siliceous sediments are characterized by low wet-bulk density and grain density and high water content, porosity, and shear strength. The calcareous sediments are characterized by relatively high wet-bulk density and grain density and low porosity and water content. These results reflect the fact that the grain density for biogenic silica ranges from 2.1 to 2.3 g/cm³ and that the grain density for biogenic calcite is 2.72 g/cm³ (Wilkens and Handyside, 1985) and that the interlocking nature of the diatom frustules tends to increase the framework strength and to keep the framework open (Hill and Marsters, 1990). The characteristic of high porosity/low wet-bulk density is well illustrated in the siliceous sediments from 110 to 120 mbsf and from 305 to 310 mbsf, where porosity reaches 80% and wet-bulk density values are as low as 1.30 g/cm³.

In the interval just above basaltic basement, which consists of calcareous nannofossil sediments with 35% to 40% diatoms, index properties are controlled by diagenetic alteration. In this interval, wet-bulk density is uncharacteristically high and porosity low for siliceous-rich sediments. Void-space reduction, resulting from hydrothermal alteration (see "Organic Geochemistry" section, this chapter), may account for these characteristics.

DOWNHOLE MEASUREMENTS

Quality of Data

Site 849 was plagued by poor hole conditions above 130 mbsf. The quality of the geophysical logs, particularly density, suffers as a
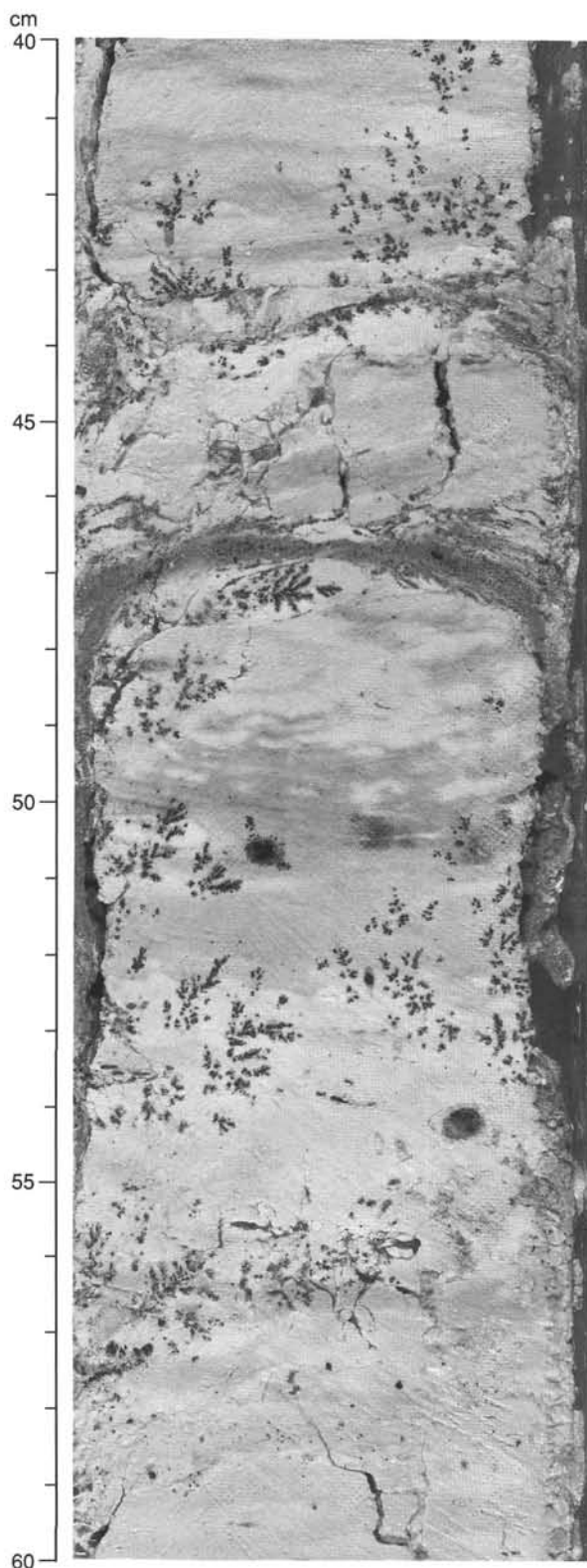
Figure 11. MnO dendrites in Section 138-849B-36X-5 at 40–60 cm.

result, although degradation of the geochemical logs was negligible. We noted a large number of drop-outs in the density log between 60 and 130 mbsf and several more below 300 mbsf (Fig. 42). In all subsequent figures and calculations (e.g., mean values and interproperty relationships), we used an edited density log in which all values <1.3 g/cm^3 (corresponding to a porosity of approximately 85%) were removed. Unless specified, density refers to this edited data. Resistivity, which is less affected by poor hole conditions, displays peaks that match edited density. The high-frequency density variations above 130 mbsf are probably noise.

Because log quality differs significantly above and below 130 mbsf, we correlated the two sections separately. Correlation of log and laboratory GRAPE and gravimetric density profiles was significantly lower in the upper part of this site, compared with the deeper part of the hole and previous Leg 138 sites. In the initial geophysical tool run, the interval from 116 to 134 mbsf had an anomalous velocity structure (Fig. 42). The steplike shape of the velocity vs. depth curve resulted from the tool sticking in the borehole at several depths (see "Operations" section, this chapter). A repeat run over this part of this depth resulted in significant improvement in the log (Fig. 42). This repeat section was spliced into the original log and has been used in subsequent figures and calculations.

FMS images and calculated dips are excellent. Contact of all four pads existed throughout the log, with the exception of one short interval from 123 to 130 mbsf. Although the heave compensator was not operating at this site, very little evidence of "chattering" (or vertical striations) was present in the Site 849 logs. The depths of logged intervals have been compiled in Table 18.

Log Stratigraphic Units

We identified one log unit at Site 849 that was divided into two subunits. The subunits have been defined on the basis of changes in the character of the velocity log.

Subunit 1A (49–147 mbsf; 1.52–4.55 Ma)

With the exception of an anomalous interval from 120 to 136 mbsf, log Subunit 1A is characterized by low velocity values (Table 19, Fig. 43). In addition, the velocity profile displays very low variability in the intervals above and below the anomalous interval (to the base of Subunit 1A). The trend observed in velocity values is characteristic of the top 100 to 200 mbsf of the velocity logs at all previous Leg 138 sites, except Site 844.

Although similarities among density, resistivity, and velocity were observed deeper in the hole, these properties are not well correlated in the upper subunit (Fig. 43). The only interval in which good correlation exists is the zone of anomalously high velocity at 120 to 136 mbsf. Density and resistivity are high in this interval; resistivity reaches its maximum value in Subunit 1A at approximately the same depth as the velocity maximum. Comparisons of physical property logs with data from the geochemical tool string (hydrogen yield and PHIG, the uncalibrated porosity from neutron flux) provide further evidence that the peaks in the physical properties in this interval are not artifacts of poor hole conditions. Low values of both porosity estimated by the neutron geochemistry tool (PHIG) and hydrogen yield (which correlates with the amount of water in the deposit, and therefore pore volume) between 120 and 136 mbsf indicate that high values of velocity, density, and resistivity observed in this interval result from low porosity values (Fig. 44), which are in turn related to the high carbonate content (see below).
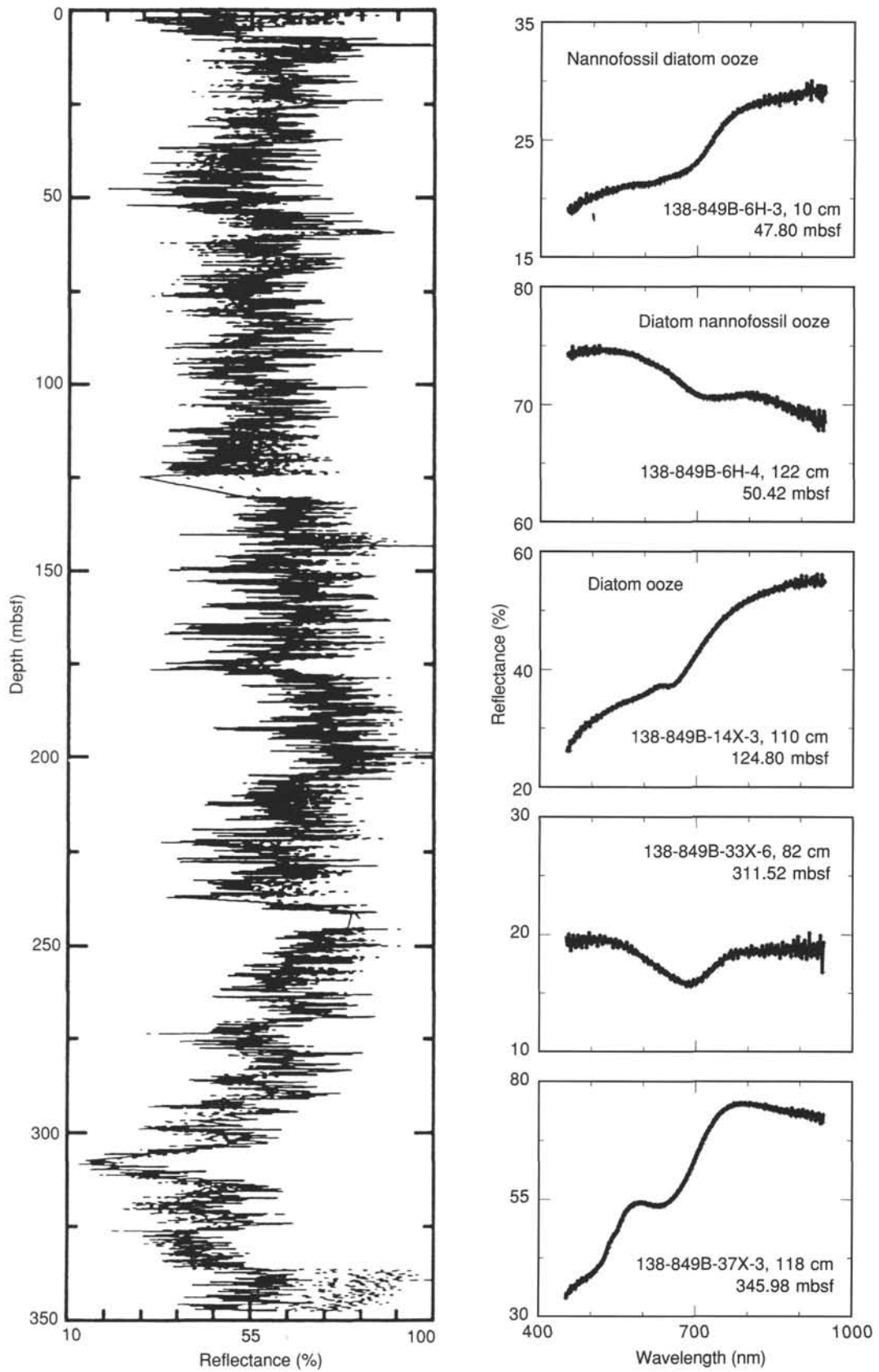
Figure 12. Summary of color variation in Hole 849B (left). Examples of reflectance spectra characteristic of the major lithologies are shown at right.
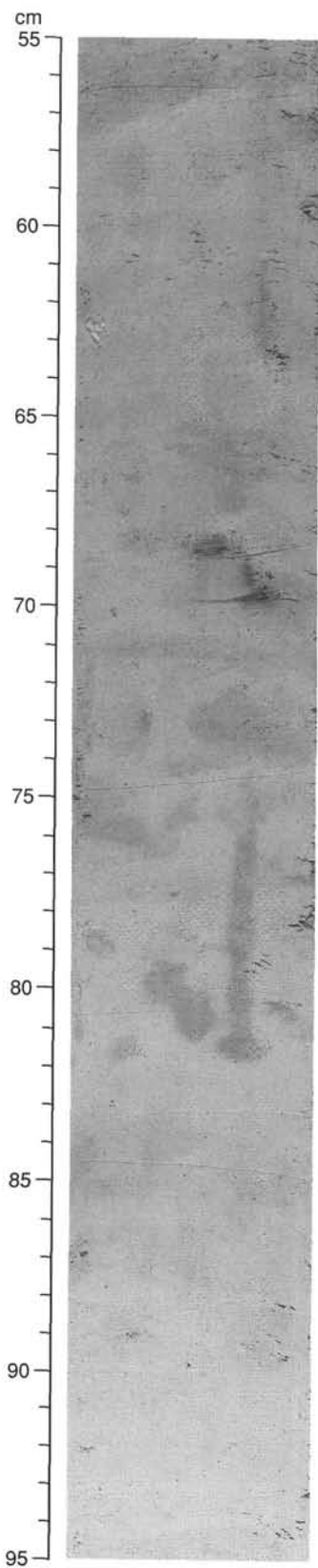
Figure 13. *Planolites* and *Skolithos* (76–81 cm)) in Section 138-849D-6H-2 at 55–95 cm.
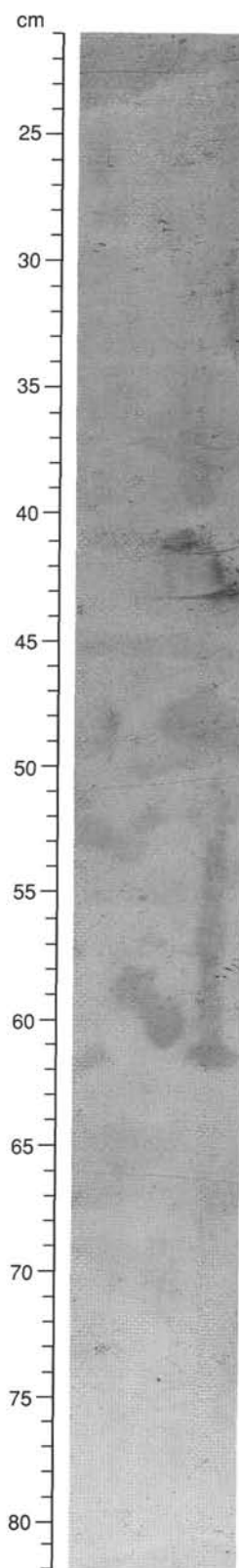
Figure 14. Interbedding of radiolarian- and clay-rich beds, with paler, more nannofossil-rich beds highlighting the burrowing in Section 138-849D-32X-5 at 21–82 cm.

cm
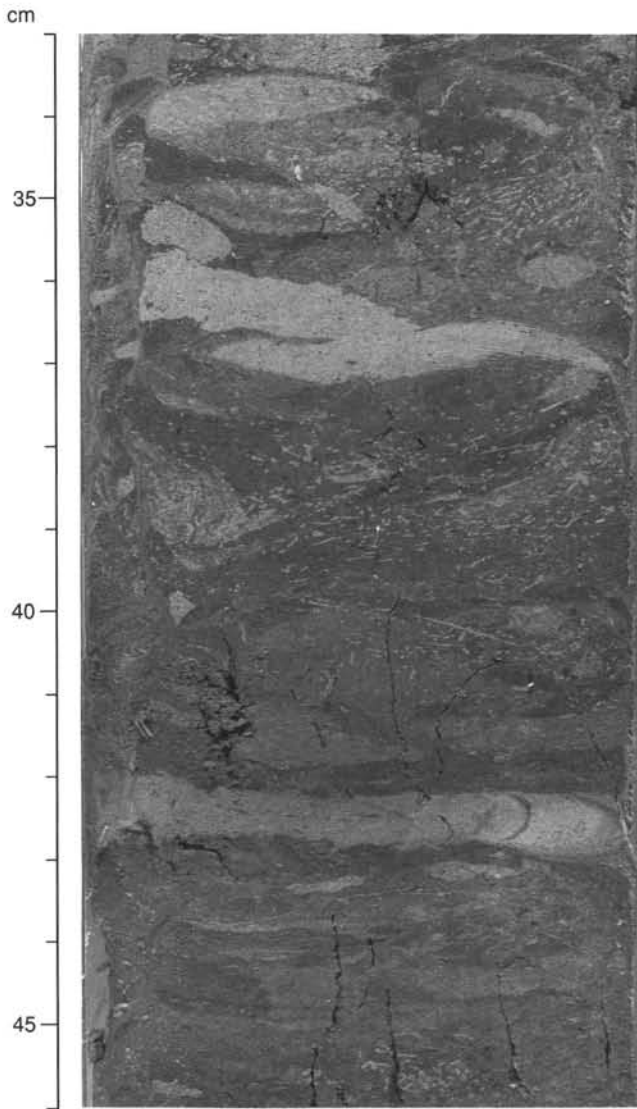
Figure 15. Abundant trace fossils including *Planolites* (36 cm), *Zoophycos* (43 cm), and *Chondrites* in Section 138-849C-32X-7 at 33–46 cm.

Subunit 1B (147–350 mbsf; 4.55–9.1 Ma)

The boundary between Subunits 1A and 1B is marked by abrupt changes in velocity, density, and resistivity (Figs. 43 and 45). Minimums in carbonate content and Ca-yield also occur at this depth (Fig. 46A). The primary difference between the two subunits is the higher velocity values and greater velocity variability in Subunit IB (Table 19, Fig. 43). Subunit 1B is also distinguished from Subunit 1A by the higher degree of correlation observed between trends in density, resistivity, and velocity (Figs. 43 and 45). An anomalous zone from 240–304 mbsf also occurs in Subunit 1B, with higher average velocity, density, and resistivity values and lower gamma-ray, PHIG, and hydrogen-yield values than surrounding sediments (Table 19, Figs. 43 and 45). This zone is also differentiated by consistently higher measurements of Ca yield and carbonate content (Fig. 46A; Table 19; "Organic Geochemistry" section, this chapter).

cm
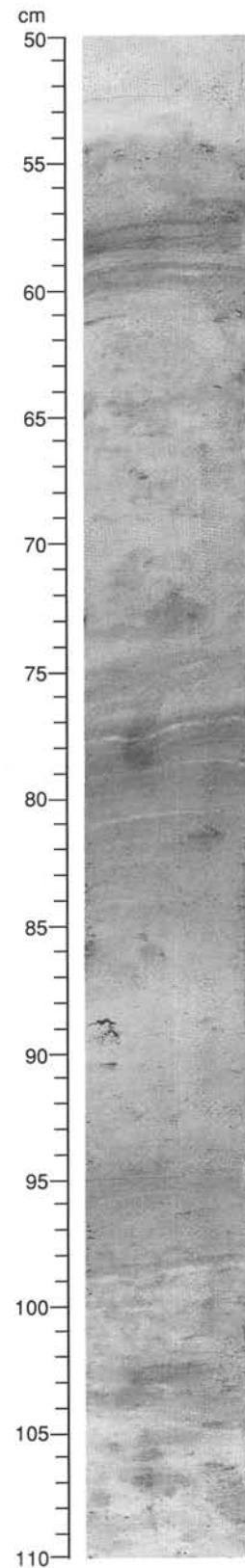
Figure 16. Example of post-depositional gray laminations and thin bands from Section 138-849D-4H-4 at 50–110 cm. Note the superposition of these structures over solid burrows.
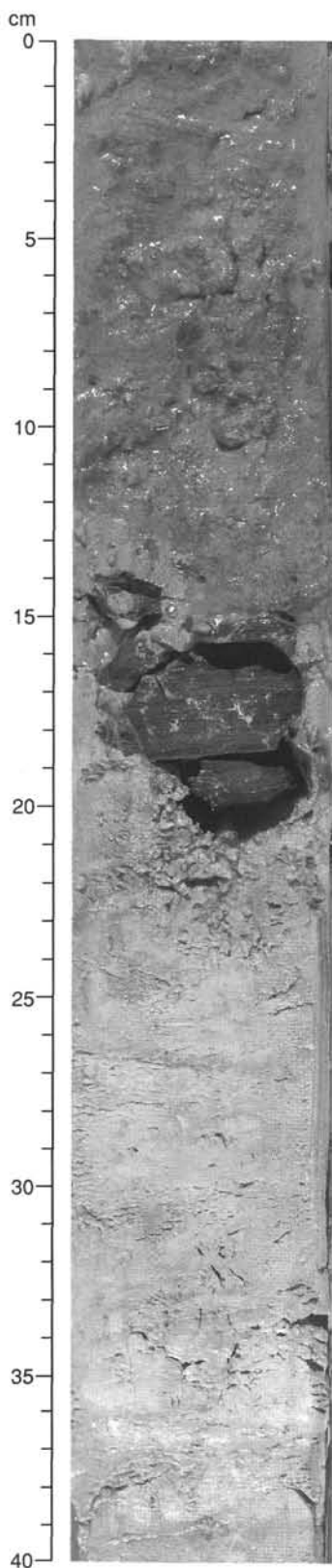
Figure 17. Silicified carbonate layer in Section 138-849D-25X-4 at 0–40 cm, separating diatom-rich ooze above from nannofossil-rich ooze below.

FMS Logs

Variability in resistivity/porosity can be seen in the FMS logs on several different scales, which correlate with the other resistivity logs. On a large scale, the borehole can be separated into a shallow section above 240 mbsf with low resistivity, and a deeper portion, between 240 and 300 mbsf, with highest resistivity, and a lower section with resistivity intermediate between the two upper units. The zone of high resistivity between 240 and 300 mbsf corresponds to the anomalous interval identified with the geophysical and geochemical logs. The most striking feature in the FMS log is an interval of high resistivity from 237 to 244 mbsf (Fig. 47), which includes thin layers of less-resistive sediment. Also within this zone are layers of very high resistivity, at least one of which occurs at the same depth as siliceous calcareous concretions recovered in the core (see Lithostratigraphy section, this chapter).

The caliper log shows an abrupt change in the shape of the borehole at 116 mbsf. Hole deviation and azimuth also change abruptly at this depth; hole diameter is very large, greater than 50 cm (Fig. 47). The geophysical tool string was stuck in the borehole at 116 mbsf and an APC core required significant overpull to recover the core barrel at this depth (see "Operations" section, this chapter), suggesting that repeated contact of these objects with the borehole wall resulted in damage to the wall and extreme elongation. The effect of standoff, where the drill string is raised in the borehole while the core is brought to the surface, also results in damage to the borehole, although to a lesser degree. This effect is clearly evident in the caliper log as enlarged hole diameters approximately every 9.5 m (Fig. 47).

Lithologic Controls on Log Properties

Much of the variability observed in the log properties can be related to carbonate content. The boundary between Subunits 1A and 1B coincides with sharp decreases in the $CaCO_3$ measures, including Ca yield, smear-slide calcareous microfossil estimates, and laboratory-determined carbonate content (Fig. 46). In addition, the two zones that have anomalous physical properties correspond to intervals of high carbonate content. Carbonate-rich intervals at Site 849 are marked by low porosity, and high density, resistivity, and velocity, compared with other lithologies. The majority of noncarbonate material consists of siliceous microfossils (see "Lithostratigraphy" section, this chapter), which have open microstructures. Sediments rich in siliceous microfossils have high porosity, and consequently low density and velocity (Bryant et al., 1981). With the exception of the interval from 120 to 142 mbsf that has anomalously high Ca yields (average value = 0.124±0.02), log Subunit IA is characterized by slightly lower average carbonate and Ca yield values than Subunit IB. Mean values of density, resistivity and velocity, consequently, are slightly lower (Table 19).

Major features in the smear-slide estimates of carbonate microfossils correlate well to Ca yield (Fig. 46B). A similar correspondence was observed between Ca yield and laboratory carbonate measurements (Fig. 46A; "Organic Geochemistry" section, this chapter). Correlations between Ca yield and both smear-slide microfossil estimates and laboratory-determined carbonate in the top 130 mbsf are poor. Similarly, correlations between density and carbonate content also are poor in this interval (Fig. 48).

Good correlations exist between density, resistivity, and velocity logs and smear-slide estimates of the dominant sedimentary components, nannofossils and diatoms (Lithostratigraphy section, this chapter; Fig. 49), further evidence of the strong influence of lithology on sediment physical properties at this site.

Table 3. Sample (core and section) and depth (mbsf and mcd) constraints of calcareous nannofossil events for Site 849.

Event	Hole 849B			Hole 849C		
	Interval (cm)	Depth (mbsf)	Depth (mcd)	Interval (cm)	Depth (mbsf)	Depth (mcd)
T *Pseudoemiliania lacunosa*	2H-3, 60–2H-4, 60	10.30–11.80	12.25–13.75			
B *Gephyrocapsa* sp. 3	3H-4, 60–3H-5, 60	21.30–22.80	25.35–26.85			
T *Gephyrocapsa* spp. >5.5µm	4H-3, 60–4H-4, 60	29.30–30.80	34.35–35.85			
B *Gephyrocapsa* spp. >5.5µm	4H-6, 60–4H-7, 60	33.80–35.30	38.85–40.35			
T *Calcidiscus macintyrei*	5H-2, 60–5H-3, 60	37.30–38.80	43.75–45.25	4H-6, 100–4H-6, 140	38.00–38.40	45.10–45.50
B *Gephyrocapsa oceanica* s.l.	5H-4, 60–5H-5, 60	40.30–41.80	46.75–48.25	5H-1, 13–5H-1, 80	39.13–39.80	47.28–47.95
T *Discoaster brouweri*	6H-5, 60–6H-6, 60	51.30–52.80	58.86–60.36			
T *Discoaster surculus*	7H-5, 60–7H-6, 60	60.80–62.30	70.25–71.75			
T *Discoaster tamalis*	8H-2, 60–8H-3, 60	65.80–67.30	76.50–78.00	7H-6, 60–7H-6, 90	66.10–66.40	77.05–77.35
T *Sphenolithus* spp.	10H-5, 60–10H-6, 60	89.30–90.80	101.10–102.60			
T *Reticulofenestra pseudoumbilicus*	10H-CC–11H-1, 60	92.49–92.80	104.29–106.40	10H-3, 120–10H-3, 140	90.70–90.90	105.15–108.35
B *Ceratolithus rugosus*	15X-5, 60–15X-6, 60	136.90–138.40	156.20–157.70			
T *Triquetrorhabdulus rugosus*	17X-1, 60–17X-2, 60	150.30–151.80	173.25–174.75			
B *Ceratolithus acutus*	17X-1, 60–17X-2, 60	150.30–151.80	173.25–174.75			
T *Discoaster quinqueramus*	18X-5, 50–18X-6, 50	165.80–167.30	190.75–192.25			
T *Amaurolithus amplificus*	21X-5, 60–21X-6, 60	193.90–195.40	223.80–225.30			
B *Amaurolithus amplificus*	21X-CC–22X-1, 60	196.61–197.60	226.51–228.75			
B *Amaurolithus primus*	27X-1, 60–27X-2, 60	245.90–247.40	277.70–279.20			
B *Discoaster berggreni*	29X-3, 81–29X-4, 40	268.51–269.60	302.91–304.00			
T *Mihylitha convallis*	32X-5, 60–32X-5, 97	300.20–300.57	337.20–337.57			
T *Discoaster hamatus*	32X-CC–33X-1, 60	303.37–303.80	340.37–341.80			
T *Coccolithus miopelagicus*	34X-6, 56–34X-7, 40	320.96–322.30	359.86–361.20			
B *Discoaster hamatus*	34X-6, 56–34X-7, 40	320.96–322.30	359.86–361.20			

T = top occurrence; B = bottom occurrence.

Table 4. Sample (core and section) and depth (mbsf and mcd) constraints of planktonic foraminifers events for Site 849.

Event	Hole 844B		
	Interval	Depth (mbsf)	Depth (mcd)
T *Globorotalia limbata*	6H-CC–7H-CC	54.54–64.26	62.04–73.71
T *Dentoglobigerina altispira*	9H-CC–10H-CC	83.29–92.49	94.94–104.29
T *Sphaeroidinellopsis* spp.	9H-CC–10H-CC	83.29–92.49	94.94–104.29
B *Globorotalia tumida*	16X-CC–17X-CC	149.53–159.44	170.03–182.39
T *Globoquadrina dehiscens*	20X-CC–21X-CC	187.16–196.61	216.01–226.51
B *Globorotalia plesiotumida*	30X-CC–31X-CC	283.87–293.69	318.17–329.74

T = top occurrence; B = bottom occurrence.

Log Density Compared with Laboratory Density

We compare log density with laboratory density here with the caveat that inaccuracies probably exist in the top 130 mbsf. Higher variability in the log density minus laboratory density values in log Subunit 1A (Fig. 50), for example, probably results partially from anomalously low log density measurements. Because log quality differs significantly above and below 130 mbsf, we correlated the two sections separately. Correlation of log and laboratory GRAPE and gravimetric density measurements is significantly lower in the upper part of this site, compared with the deeper part of the hole and previous Leg 138 sites.

Log Subunit 1B is marked by both lower variability and generally lower differences between log and laboratory density values, particularly with respect to gravimetric measurements (Table 20, Fig. 50). As observed at previous Leg 138 sites, the differences between log and GRAPE density values are less than log density-gravimetric density because of difficulties calibrating the GRAPE measurements. Correlations between density differences and Ca yield or laboratory-determined carbonate content are low (correlation coefficients <0.3), possibly because the depths of the various measurements are not identical. The agreement among log and laboratory densities in carbonate-rich intervals may be the result of a lower degree of porosity

rebound in carbonate sediments (Hamilton, 1976). This result is contrary to the effects predicted by Hamilton, who estimated a higher porosity rebound in carbonate vs. siliceous deposits, but supports other recent research on carbonate rebound (Urmos et al., in press). The absence of a monotonic downhole increase in density-difference values at Site 849 suggests that the effects of increasing overburden stress on porosity rebound discussed by Hamilton (1976) are less significant in this deposit than are the effects of lithologic changes.

SEISMIC STRATIGRAPHY

Modeling Procedure

Synthetic seismograms were generated from velocity and density models for Site 849 to correlate reflectors in the seismic section to stratigraphic changes.

The density model was created by merging laboratory density to *in-situ* logging density. The logging density was unreliable to about 150 mbsf because of extensive washing-out of the hole. Depth-shifted logging density (by correlation with the Hole 849B GRAPE density) was used over the interval 146.2–332.7 m (150.0–336.6 mbsf) (see "Downhole Measurements" section, this chapter). Over the interval from 0 to 150.0 mbsf, 10-point boxcar-filtered GRAPE density primarily from Hole 849B was merged with the depth-shifted logging

Table 3 (continued).

	Hole 849D		
Event	Interval (cm)	Depth (mbsf)	Depth (mcd)
T *Pseudoemiliania lacunosa*			
B *Gephyrocapsa* sp. 3			
T *Gephyrocapsa* spp. >5.5µm			
B *Gephyrocapsa* spp. >5.5µm			
T *Calcidiscus macintyrei*			
B *Gephyrocapsa oceanica* s.l.			
T *Discoaster brouweri*	5H-3, 140–5H-4, 35	43.40–43.85	54.85–55.30
T *Discoaster surculus*			
T *Discoaster tamalis*			
T *Sphenolithus* spp.			
T *Reticulofenestra pseudoumbilicus*			
B *Ceratolithus rugosus*	14-CC–15X-1, 46	134.57–135.26	152.47–155.76
T *Triquetrorhabdulus rugosus*	16X-5, 60–16X-5, 105	151.10–151.55	173.70–174.15
B *Ceratolithus acutus*	18X-3, 75–18X-3, 100	167.05–167.30	194.45–194.70
T *Discoaster quinqueramus*			
T *Amaurolithus amplificus*			
B *Amaurolithus amplificus*			
B *Amaurolithus primus*			
B *Discoaster berggreni*	28X-CC–29X-1, 25	268.44–268.85	306.29–307.2
T *Mihylitha convallis*			
T *Discoaster hamatus*			
T *Coccolithus miopelagicus*	33X-CC–34X-2, 20	317.31–319.70	359.01–361.70
B *Discoaster hamatus*			

density. A large decrease in density occurred at 120.7 mbsf in Hole 849B, corresponding to a switch from the APC to the XCB. Thus, missing and poor data from 120.7 to 130.3 mbsf from Hole 849B were replaced by the corresponding data from Hole 849D (121.5–131.7 mbsf). In addition, no attempt was made to align density values at 150.0 mbsf, even though a sharp shift exists, because a sharp excursion in the GRAPE density occurred at about 150.5 mbsf in Hole 849B that does not exist in the logging density near this depth. Beyond 336.6 mbsf, to the depth of basement (350.55 mbsf), a constant density of 1.50 g/cm^3 was used.

The velocity model was created in a similar manner as above. From 150.0–333.5 mbsf, depth-shifted logging velocity was employed. To fill the gap in the upper part of the section, laboratory velocities collected with the DSV were corrected to *in-situ* conditions for changes of sound speed as a function of temperature and pressure, assuming a temperature gradient of 7.8°C/km and a bottom-water temperature of 1.53°C determined from the temperature log. As above, Hole 849D DSV values were used from 120.7 to 130.3 mbsf. Linear least-square fits of the corrected DSV values from 0 to 120 and 120 to 200 mbsf were made to match the APC and XCB values at 120.7 mbsf, and this process resulted in an upward shift in XCB values by 12.8 m/s. From 333.5 to 350.5 mbsf, a constant velocity equal to the final log velocity (1635.0 m/s) was used.

The accuracy of the traveltime-to-depth conversion can be evaluated by the generation of synthetic seismograms and the subsequent comparison to the seismic record collected over the site. Synthetic seismograms were generated using the above merged velocity and density data. These data were resampled at a 1-ms sample interval (approximately 60 cm) and then used to calculate acoustic impedance and reflection coefficients and finally, a synthetic seismogram. Density and velocity values typical of basalt (2.5 g/cm^3 and 3000 m/s, respectively) were added at the basement depth (350.5 mbsf) to generate a basement reflector in the synthetic. The model used to generate the synthetic seismogram assumes plane waves, no multiples, and no signal attenuation; the model is described in Mayer et al. (1985). The final synthetic seismogram was filtered from 70 to 250 Hz, the same filter parameters as the field record collected during the Site 849 survey.

Results

A comparison of the synthetic seismogram with the seismic profile collected at Site 849 shows a good match between the two (Fig. 51). There is nearly a one-to-one correspondence between major reflectors with an excellent match at basement. This suggests that the traveltime-to-depth conversion is fairly accurate.

Given an acceptable velocity model, the origin of some of the reflectors at Site 849 can be analyzed. We emphasize that these are preliminary results that will undoubtedly be modified after more careful analysis. Seventeen major reflectors or reflector packages were identified. These reflectors were selected on the basis of amplitude and lateral coherency in the seismic record in the immediate area of Site 849. The two-way traveltime on the synthetic seismogram of the top and bottom of each reflector was measured and, by using the assumed-velocity model, the depth range of each reflector was determined.

The velocity, density, and acoustic impedance models were compared to the depth ranges calculated from the traveltime to determine the changes in physical properties causing the selected seismic reflectors. In general, within 1.5 m of each calculated depth range, a large change in density and/or velocity can be associated with each reflector (Fig. 52). Reflectors for the upper 150 m (reflectors 0–5) are solely related to large changes in density. Beyond 150 m, the reflectors are due to synchronous, large fluctuations in velocity and density. The depths (synthetic, mbsf, and mcd) and ages (based on magnetostratigraphy and biostratigraphy of Site 849; see "Sedimentation Rates" section, this chapter) of these reflectors are presented in Table 21. A detailed understanding of the lithologic, biostratigraphic, and ultimately, the paleoceanographic significance of these events must await shore-based studies at this time.

SUMMARY AND CONCLUSIONS

Site 849 is the second site drilled along the Leg 138 western transect. This transect, situated along 110°W, was designed to sample the various elements of the equatorial circulation system in an area far removed from the influence of the eastern boundary of the Pacific

Table 5. Sample (core and section) and depth (mbsf and mcd) constraints of radiolarian events for Site 849.

Event	Hole 849B			Hole 849C		
	Interval	Depth (mbsf)	Depth (mcd)	Interval	Depth (mbsf)	Depth (mcd)
T *Stylatractus universus*	2H-5–2H-CC	13.80–15.63	16.09–17.58			
B *Collosphaera tuberosa*	2H-CC–3H-3	15.63–20.30	17.58–23.45	1H-CC–2H-CC	10.68–20.45	11.43–23.45
T *Lamprocyrtis neoheteroporos*	3H-5–3H-CC	23.30–25.21	27.36–29.26			
T *Anthocyrtidium angulare*	3H-CC–4H-3	25.21–29.80	29.26–34.85			
T *Theocorythium vetulum*	3H-CC–4H-3	25.21–29.80	29.26–34.85			
B *Lamprocyrtis nigriniae*	4H-5–4H-CC	32.80–35.47	37.85–40.52			
B *Theocorythium trachelium*	4H-CC–5H-1	35.47–36.70	40.52–43.15			
B *Pterocorys minythorax*	4H-CC–5H-1	35.47–36.70	40.57–43.15			
B *Anthocyrtidium angulare*	5H-3–5H-5	39.30–42.30	48.03–48.75			
T *Pterocanium prismatium*	5H-3–5H-5	39.30–42.30	48.03–48.75			
T *Lamprocyrtis heteroporos*	5H-1–5H-3	36.70–39.30	43.15–44.93	3H-CC–4H-CC	29.30–37.83	35.66–44.93
T *Anthocyrtidium jenghisi*	7H-3–7H-5	58.70–61.30	70.17–71.15			
B *Theocalyptra davisiana*	7H-CC–8H-3	64.26–67.80	73.71–78.50			
T *Stichocorys peregrina*	7H-CC–8H-3	64.26–67.80	73.71–78.50			
T *Anthocyrtidium pliocenica*	9H-3–9H-5	77.30–80.30	89.24–91.95	8H-CC–9H-CC	77.44–86.58	89.24–99.18
B *Lamprocyrtis neoheteroporos*	9H-3–9H-5	77.30–80.30	88.95–89.24	7H-CC–8H-CC	68.03–77.44	78.98–89.24
B *Lamprocyrtis heteroporos*	9H-3–9H-5	77.30–80.30	88.95–89.24	7H-CC–8H-CC	68.03–77.44	78.98–89.24
T *Phormostichoartus fistula*	10H-5–10H-CC	89.80–92.49	102.66–104.29			
T *Lychnodictyum audax*	10H-CC–11H-3	92.49–96.30	104.34–109.90	9H-CC–10H-CC	86.58–96.62	99.18–111.07
T *Spongaster pentas*	11H-3–11H-5	96.30–99.30	109.90–111.07	9H-CC–10H-CC	86.58–96.62	99.18–111.07
T *Phormostichoartus doliolum*	10H-CC–11H-3	92.49–96.30	104.34–109.90			
B *Amphirhopalum ypsilon*	11H-3–11H-5	96.30–99.30	109.90–111.07	9H-CC–10H-CC	86.58–96.62	99.18–111.07
B *Spongaster tetras*	11H-CC–12H-3	102.16–105.80	115.76–120.25			
T *Didymocyrtis penultima*	11H-CC–12H-3	102.16–105.80	115.76–120.25			
B *Pterocanium prismatium*	14X-3–14X-CC	124.80–143.16	142.80–143.16			
T *Spongaster berminghami*	15X-5–15X-CC	137.40–139.71	156.70–159.01			
B *Spongaster pentas*	17X-5–17X-CC	156.80–159.44	179.75–182.39			
T *Solenosphaera omnitubus*	17X-3–17X-5	153.80–156.80	176.75–179.75			
T *Siphostichartus corona*	18X-3–18X-5	163.44–166.44	188.39–191.36			
T *Acrobotrys tritubus*	24X-3–24X-5	220.40–223.40	254.76–256.30			
T *Stichocorys johnsoni*	23X-3–23X-5	210.69–213.69	244.19–245.79			
Stichocorys delmontensis > *S. peregrina*	26X-3–26X-4	236.85–237.80	274.10–275.05			
T *Calocycletta caepa*	23X-3–23X-5	210.69–213.69	242.79–244.19			
B *Solenosphaera omnitubus*	26X-CC–27X-3	242.00–249.40	276.25–281.20			
T *Diartus hughesi*	29X-CC–30X-3	274.38–278.40	308.78–312.70			
B *Acrobotrys tritubus*	30X-3–30X-5	278.40–281.40	312.70–315.70			
B *Spongaster berminghami*	31X-3–31X-5	288.00–291.00	324.05–327.05			
T *Stichocorys wolffii*	32X-3–32X-5	297.70–300.70	337.20–337.70			
T *Botryostrobus miralestensis*	30X-CC–31X-3	283.87–288.00	318.17–324.05			
T *Diartus pettersoni*	31X-5–31X-CC	291.00–293.69	327.57–329.74			
B *Lithopera bacca*	34X-3–34X-5	326.70–329.70	355.90–358.90			
Diartus pettersoni > *Diartus hughesi*	31X-5–31X-CC	291.00–293.69	327.57–329.74			
B *Diartus hughesi*	32X-3–32X-5	297.70–300.70	334.70–337.20			
T *Cyrtocapsella japonica*	33X-CC–34X-3	313.06–326.70	351.06–355.90			
T *Lithopera thornburgi*	33X-CC–34X-3	313.06–326.70	351.06–355.09			
T *Carpocanium cristata*	35X-3–35X-5	326.70–329.70	366.55–369.56			

T = top occurrence; B = bottom occurrence; > = evolutionary transition.

Ocean. The transect also serves as the eastern end member of a series of studies (Legs 85 and 130) aimed at understanding the regional and global response of the equatorial Pacific Ocean to climatic change. The present location of Site 849 is within the equatorial divergence zone; thus, the site was selected to provide the latest Neogene history of the oceanic conditions within this highly productive region.

Site 849 is located about 860 km west of the East Pacific Rise on crust generated about 11–12 Ma. The backtracked path of the site is straightforward, constrained by the movement of the Pacific Plate, which can be reconstructed from the numerous hot-spot traces of the Pacific Ocean and from sediment distribution in the equatorial region (van Andel et al., 1975; see Fig. 2 in "Background and Scientific Objectives" section, this chapter). From an original ridge crest depth of approximately 2700 m, the site has subsided to its present depth of 3850 m and in doing so has intercepted a regionally and temporally variable lysocline. Throughout its history, Site 849 has been above the CCD.

The pattern of sedimentation at Site 849 is now a familiar one for pelagic sediments within this region of the equatorial Pacific Ocean.

The first sediment to accumulate above the newly formed Site 849 was a nannofossil ooze containing a substantial component of iron-oxides and clays. Initial sedimentation rates at the site are around 50 m/m.y. As with many sites in the equatorial region, sedimentation rates decreased after 10 Ma. Sedimentation rates during the time interval 10–8 Ma are the lowest in the section, estimated at 15 m/m.y. (Fig. 53A). At this time the estimated backtrack of this site places the site at about 2°–2.5° south of the Equator (Table 22). These reduced sedimentation rates are not too different from the present-day sedimentation rates of Site 848 now at 2°59'S. This interval of reduced sedimentation rate is characterized by increased dissolution of calcium carbonate and coincides with a similar event seen at all Leg 138 sites and seems to represent a major dissolution event within the Pacific Ocean.

At about 8 Ma, an overall increase in sedimentation rates took place until about 40 m/m.y., which is reflected in an increase in mass accumulation rates of calcium carbonate, organic carbon, and noncarbon material (see Fig. 33 in "Organic Geochemistry" section, this chapter). As at other sites drilled during Leg 138, the

Table 5 (continued).

| | Hole 849D | | |
Event	Interval	Depth (mbsf)	Depth (mcd)
T *Stylatractus universus*			
B *Collosphaera tuberosa*			
T *Lamprocyrtis neoheteroporos*			
T *Anthocyrtidium angulare*			
T *Theocorythium vetulum*			
B *Lamprocyrtis nigriniae*			
B *Theocorythium trachelium*			
B *Pterocorys minythorax*			
B *Anthocyrtidium angulare*	4H-CC–5H-CC	41.48–51.90	48.03–60.35
T *Pterocanium prismatium*	4H-CC–5H-CC	41.48–51.90	48.03–60.35
T *Lamprocyrtis heteroporos*			
T *Anthocyrtidium jenghisi*	5H-CC–6H-CC	51.90–60.92	60.35–70.17
B *Theocalyptra davisiana*			
T *Stichocorys peregrina*			
T *Anthocyrtidium pliocenica*			
B *Lamprocyrtis neoheteroporos*			
B *Lamprocyrtis heteroporos*			
T *Phormostichoartus fistula*	9H-CC–10H-CC	89.76–99.05	102.66–113.30
T *Lychnodictyum audax*			
T *Spongaster pentas*			
T *Phormostichoartus doliolum*			
B *Amphirhopalum ypsilon*			
B *Spongaster tetras*			
T *Didymocyrtis penultima*			
B *Pterocanium prismatium*			
T *Spongaster berminghami*			
B *Spongaster pentas*			
T *Solenosphaera omnitubus*			
T *Siphostichartus corona*			
T *Acrobotrys tritubus*	23X-CC–24X-CC	220.86–230.53	254.76–266.88
T *Stichocorys johnsoni*	22X-CC–23X-CC	211.09–220.86	244.19–254.76
Stichocorys delmontensis > *S. peregrina*			
T *Calocycletta caepa*	21X-CC–22X-CC	201.14–211.09	232.64–244.19
B *Solenosphaera omnitubus*			
T *Diartus hughesi*			
B *Acrobotrys tritubus*			
B *Spongaster berminghami*			
T *Stichocorys wolffii*	30X-CC–31X-CC	288.07–297.70	327.57–337.20
T *Botryostrobus miralestensis*			
T *Diartus pettersoni*	29X-CC–30X-CC	278.44–288.07	316.79–327.57
B *Lithopera bacca*			
Diartus pettersoni > *Diartus hughesi*	29X-CC–30X-CC	278.44–288.07	316.79–327.57
B *Diartus hughesi*	30X-CC–31X-CC	288.07–297.70	327.57–337.20
T *Cyrtocapsella japonica*			
T *Lithopera thornburgi*			
T *Carpocanium cristata*			

latest Miocene and early Pliocene were marked by extremely high sedimentation rates. At Site 849, rates of more than 100 m/m.y. have been estimated for the time interval from 4.0 to 5 Ma. At this time, the site had moved well into the equatorial divergence zone. Although still within the equatorial divergence zone during the Pliocene and Pleistocene, sedimentation rates decreased to a relatively constant 30 m/m.y., indicating a temporal change in oceanic conditions. Ultimately, comparisons with other sites along the 110°W transect combined with analysis of biogenic silica and detailed microfossil analysis will allow us to evaluate whether this decrease in sedimentation rates reflects a change in the north-south gradients across the Equator.

Mass accumulation rates of organic carbon and calcium carbonate during the latest Miocene are also three times greater than during the Pliocene and Pleistocene (see Fig. 33 in "Organic Geochemistry" section, this chapter). It is not possible at this time to evaluate the effect of changing dissolution for controlling this marked change in sediment accumulation. However, sediment trap studies from the equatorial divergence at 140°W suggest that even if the entire present-day flux of carbonate were preserved in the geologic record, about

a two- to three-fold increase in carbonate accumulation rates might be explained in terms of only carbonate preservation (Murray, 1987). Assuming that these present-day fluxes at 140°W are representative of those at 110°W and given the evidence of carbonate dissolution at Site 849, we infer that the high accumulation during the latest Miocene must reflect increased production.

One indication of increased production at this site is the presence of very diatom-rich layers. Structurally, these layers are laminated and contain a very high percentage of diatom tests of, usually, a single species, *Thalassiothrix longissima*. These intervals are most prominent at 3.5 to 4.6 Ma, 4.9 to 5.3 Ma, and 6 to 6.7 Ma. While it is not yet possible to determine the mode of formation of these laminated intervals, they have been found in a number of sites and seem to occur within similar time intervals.

The interstitial-water chemistry at Site 849 is unusual in that the diffusive transport of many constituents appears to be disrupted by a layer of diagenetically silicified calcite at 237 mbsf (approx. 6.2 Ma). The layer (represented by a calcite nodule in the core and clearly discernable in the logs) appears to seal off the bottom 100 m of the

Table 6. Sample and depth constraints of diatom events for Site 849.

Event	Hole 849B			Hole 849C		
	Interval	Depth (mbsf)	Depth (mcd)	Interval	Depth (mbsf)	Depth (mcd)
T *Nitzschia reinholdii*						
T *Nitzschia fossilis*	2H-CC–3H-3	15.63–19.90	17.58–23.95			
T *Rhizosolenia praebergonii* var. *robotus*	5H-4–5H-6	40.40–43.40	46.85–49.85	4H-CC–5H-CC	37.83–49.03	44.93–57.18
B *Pseudoeunotia doliolus*	6H-3–6H-5	47.85–51.40	55.35–62.05	5H-CC–6H-CC	49.03–57.40	57.18–67.00
T *Thalassiosira convexa* var. *convexa*	7H-3–7H-CC	57.80–64.26	66.80–73.71	6H-CC–7H-CC	57.40–68.03	67.00–78.98
T *Nitzschia jouseae*	8H-2–8H-4	65.80–68.80	76.50–79.50	6H-CC–7H-CC	57.40–68.03	67.00–78.98
B *Rhizosolenia praebergonii*	9H-2–9H-4	75.30–78.30	86.95–89.95	7H-CC–8H-CC	68.03–77.44	78.98–89.24
B *Thalassiosira convexa* var. *convexa*	10H-CC–11H-2	92.49–94.40	104.29–108.00	9H-CC–10H-CC	86.58–96.62	99.18–111.07
T *Nitzschia cylindrica*	11H-CC–12H-6	107.50–116.00	114.75–123.75			
B *Nitzschia jouseae*	16X-1–16H-CC	140.70–149.53	161.20–170.03			
T *Nitzschia miocenica*	20X-CC–21H-CC	187.16–196.61	216.01–226.51			
T *Nitzschia miocenica* var. *elongata*	20X-CC–21H-CC	187.16–196.61	216.01–226.51			
T *Thalassiosira praeconvexa*	20X-CC–21H-CC	187.16–196.61	216.01–226.51			
B *Thalassiosira miocenica*	24X-3–24X-6	219.90–224.40	252.80–257.30			
B *Thalassiosira convexa*	24X-3–24X-6	219.90–224.40	252.80–257.30			
B *Thalassiosira praeconvexa*	26X-CC–27H-2	242.00–247.50	276.25–279.30			
B *Nitzschia miocenica*	28X-4–28H-7	260.10–264.40	294.25–298.55			
T *Actinocyclus ellipticus* var. *javanicus*	28X-CC–29H-CC	264.68–274.38	298.83–308.78			
B *Nitzschia cylindrica*	30X-4–30X-5	279.35–280.50	313.65–315.85			
T *Thalassiosira yabei*	30X-4–30X-5	279.35–280.50	313.65–315.85			
T *Denticulopsis hustedtii*	32X-2–33X-4	295.80–308.25	332.80–346.25			

T = top occurrence; B = bottom occurrence.

sediment column, disrupting diffusive transport between the material above and below. The effect of this layer is seen in the profiles of alkalinity, sulfate, ammonia, calcium, and strontium; above the layer these profiles were controlled by diagenesis, below it, they were controlled by diffusion. The position of this layer is associated with a very rapid shift in the carbonate curve (Fig. 53C) and a regional seismic reflector. This same shift has been noted at a number of Leg 138 sites, implying that it represents a regional oceanographic event; the diagenetic layer may be a local response to this event. Methane concentration also increases steadily with depth to the level of the silicified calcite.

Throughout much of its history, Site 849 has been within the highly productive waters of the equatorial divergence, a fact reflected in the generally high sedimentation rates and carbonate percentages that characterize this site. As seen in the GRAPE-predicted carbonate curve (Fig. 53C), superimposed on this trend is a tremendous amount of high-frequency variability in the carbonate system. This variability is correlatable from site to site over thousands of kilometers. Mapping of this variability thus can provide a powerful new means of stratigraphic correlation as well as provide important insight into the interactions of the ocean/climate systems.

REFERENCES

Baker, P. A., 1986. Pore water chemistry of carbonate-rich sediments, Lord Howe Rise, Southwest Pacific Ocean. *In* Kennett, J. P., von der Borch, C. C., et al., *Init. Repts. DSDP*, 90: Washington (U.S. Govt. Printing Office), 1249–1256.

Baker, P. A., Gieskes, J. M., and Elderfield, H., 1982. Diagenesis of carbonates in deep-sea sediments-evidence from Sr/Ca ratios and interstitial dissolved Sr^{2+} data. *J. Sediment. Petrol.*, 52:71–82.

Bryant, W. R., Bennett, R. H., and Katherman, C. E., 1981. Shear strength, consolidation, porosity, and permeability of oceanic sediments. *In* Emiliani, C. (Ed.), *The Sea* (Vol. 7): New York (Wiley), 1555–1616.

Claypool, G. E., and Kaplan, I. R., 1974. The origin and distribution of methane in marine sediments. *In* Kaplan, I. R. (Ed.), *Natural Gases in Marine Sediments*. Mar. Sci., 3:99–140.

Elderfield, H., and Gieskes, J. M., 1982. Sr isotopes in interstitial waters of marine sediments from Deep Sea Drilling Project cores. *Nature*, 333:493–497.

Gieskes, J. M., 1974. Chemistry of interstitial waters of marine sediments. *Annu. Rev. Earth Planet. Sci.*, 3:433–394.

————, 1983. The chemistry of interstitial waters of deep sea sediments: interpretation of deep sea drilling data. *In* Riley, J. P., and Chester, R. (Eds.), *Chemical Oceanography* (Vol.8): London (Academic Press), 221–269.

Gieskes, J. M., Elderfield, H., and Palmer, M. R., 1986. Strontium and its isotopic composition in interstitial waters of marine carbonate sediments. *Earth Planet. Sci. Lett.*, 77:229–235.

Hamilton, E. L., 1976. Variations of density and porosity with depth in deep-sea sediments. *J. Sediment. Petrol.*, 46:280–300.

Harrison, W. E., Hesse, R., and Gieskes, J. M., 1982. Relationship between sedimentary facies and interstitial water chemistry of slope, trench, and Cocos Plate sites from the Middle America Trench transect, active margin off Guatemala, Deep Sea Drilling Project Leg 67. *In* Aubouin, J., von Huene, R., et al., *Init. Repts. DSDP*, 67: Washington (U.S. Govt. Printing Office), 603–613.

Hill, P. R., and Marsters, J. C., 1990. Controls on physical properties of Peru continental margin sediments and their relationship to deformation styles. *In* Suess, E., von Huene, R., et al., *Proc. ODP, Sci. Results*, 112: College Station, TX (Ocean Drilling Program), 623–632.

Johnson, D. A., and Nigrini, C. A., 1985. Synchronous and time-transgressive Neogene radiolarian datum levels in the equatorial Indian and Pacific Oceans. *Mar. Micropaleontol.*, 9:489–523.

Johnson, D. A., Schneider, D. A., Nigrini, C. A., Caulet, J. P., and Kent, D., 1989. Pliocene-Pleistocene radiolarian events and magnetostratigraphic calibrations for the tropical Indian Ocean. *Mar. Micropaleontol.*, 14:33–66.

Kastner, M., 1981. Authigenic silicates in deep-sea sediments: formation and diagenesis. *In* Emiliani, C. (Ed.) *The Sea* (Vol.7): *The Oceanic Lithosphere*: New York (Wiley), 915–980.

Mammerickx, J., 1989. The Eastern Pacific Ocean and Hawaii. *In* Winterer, E. L., et al. (Eds.), *The Geology of North America* (Vol. N). Geol. Soc. Am.

Martini, E., 1971. Standard Tertiary and Quaternary calcareous nannoplankton zonation. *Proc. 2nd Planktonic Conf. Roma*. Rome (Ed. Tecnosci.), 739–785.

Mayer, L. A., 1979. The origin of fine scale acoustic stratigraphy in deep-sea carbonates. *J. Geophys. Res.*, 84:6177–6184.

Mayer, L. A., Shipley, T. H., Theyer, F., Wilkens, R. W., and Winterer, E. L., 1985. Seismic modelling and paleoceanography at DSDP Site 574. *In* Mayer, L. A., Theyer, F., Thomas, E., et al., *Init. Repts. DSDP*, 85: Washington (U.S. Govt. Printing Office), 947–970.

Murray, D., 1987. Spacial and temporal variations in sediment accumulation in the central tropical Pacific [Ph.D. dissert.]. Oregon State Univ., Corvallis.

Okada, H., and Bukry, D., 1980. Supplementary modification and introduction of code numbers to the low-latitude coccolith biostratigraphic zonation (Bukry, 1973; 1975). *Mar. Micropaleontol.*, 5:321–325.

Stout, P. M., 1985. Interstitial water chemistry and diagenesis of biogenic sediments from the eastern equatorial Pacific, Deep Sea Drilling Project

Table 6 (continued).

Event	Interval	Depth (mbsf)	Depth (mcd)
		Hole 849D	
T *Nitzschia reinholdii*	1H-CC–2H-CC	8.36–22.97	11.66–26.87
T *Nitzschia fossilis*	2H-CC–3H-CC	22.97–32.79	26.87–36.64
T *Rhizosolenia praebergonii* var. *robotus*	4H-CC–5H-CC	41.48–51.90	48.03–60.35
B *Pseudoeunotia doliolus*	5H-CC–6H-CC	51.90–60.92	60.35–70.17
T *Thalassiosira convexa* var. *convexa*	6H-CC–7H-CC	60.92–70.93	70.17–90.38
T *Nitzschia jouseae*	6H-CC–7H-CC	60.92–70.93	70.17–90.38
B *Rhizosolenia praebergonii*	7H-CC–8H-CC	70.93–79.20	70.17–90.38
B *Thalassiosira convexa* var. *convexa*	9H-CC–10H-CC	89.76–99.05	102.66–113.30
T *Nitzschia cylindrica*			
B *Nitzschia jouseae*	15X-CC–16X-CC	144.41–154.20	164.91–176.80
T *Nitzschia miocenica*	20X-CC–21X-CC	191.70–201.14	222.60–232.64
T *Nitzschia miocenica* var. *elongata*	20X-CC–21X-CC	191.70–201.14	222.60–232.64
T *Thalassiosira praeconvexa*	20X-CC–21X-CC	191.70–201.14	222.60–232.64
B *Thalassiosira miocenica*	23X-CC–24X-CC	220.86–230.56	254.76–266.88
B *Thalassiosira convexa*	23X-CC–24X-CC	220.86–230.56	254.76–266.88
B *Thalassiosira praeconvexa*			
B *Nitzschia miocenica*	27X-CC–28H-CC	259.27–268.44	295.92–306.29
T *Actinocyclus ellipticus* var. *javanicus*	28X-CC–29X-CC	268.44–278.44	306.29–316.79
B *Nitzschia cylindrica*	29X-CC–30X-CC	278.44–288.07	316.79–327.57
T *Thalassiosira yabei*	29X-CC–30X-CC	278.44–288.07	316.79–327.57
T *Denticulopsis hustedtii*	31X-CC–32X-CC	297.70–307.49	337.20–348.39

Leg 85. *In* Mayer, L., Theyer, F., Thomas, E., et al., *Init. Repts. DSDP*, 85: Washington (U.S. Govt. Printing Office), 805–820.

Urmos, J., Wilkens, R., Bassinot, F., Lyle, M., Marsters, J., and Mayer, L., in press. Laboratory and well-log velocity and density measurements from the Ontong Java plateau: new in situ corrections to laboratory data for pelagic carbonates. *In* Kroenke, L. W., Berger, W. H., Janacek, T. R., et al., *Proc. ODP, Init. Repts.*, 130: College Station, TX (Ocean Drilling Program).

van Andel, T. J., Heath, G. R., and Moore, T. C., Jr., 1975. Cenozoic tectonics, sedimentation, and paleoceanography of the central equatorial Pacific. *Mem. Geol. Soc. Am.*, 143.

Wilkens, R. H., and Handyside, T., 1985. Physical properties of equatorial Pacific sediments. *In* Mayer, L., Theyer, F., Thomas, E., et al., *Init. Repts. DSDP*, 85: Washington (U.S. Govt. Printing Office), 839–847.

Ms. 138A-114

NOTE: For all sites drilled, core description forms ("barrel sheets") and core photographs have been reproduced on coated paper and can be found in Section 8, beginning on page 1099. Forms containing smear-slide data can be found in Section 9, beginning on page 1435.

Formation microscanner images for this site are presented on microfiche in the back of Part 2.
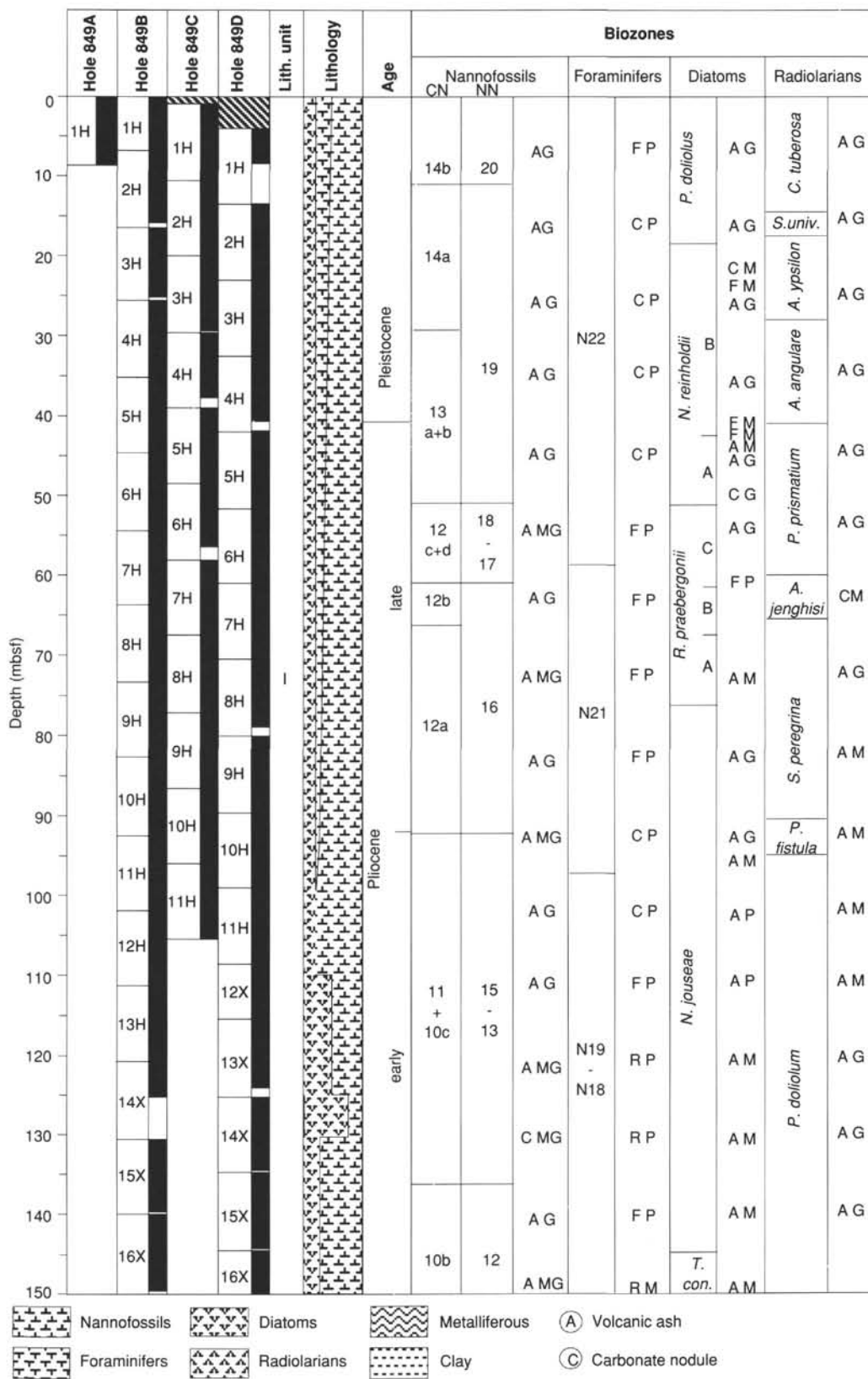
Figure 18. Stratigraphic summary for Site 849. Depth is in meters below seafloor (mbsf) and composite depth in meters composite depth (mcd). Hatched area represents intervals where specimens of a particular microfossil group are rare or absent, which hindered our assigning of zones. Dashed lines represent uncertainty in placement of a zonal boundary. Microfossil abundances recorded as A = abundant; C = common; F = few; R = rare; B = barren. Microfossil preservation recorded as G = good; M = moderate; P = poor. This figure is a general overview of the stratigraphic results at Site 849. Placement of specific stratigraphic boundaries may differ slightly among holes. Data presented here were based on results from Hole 849B.
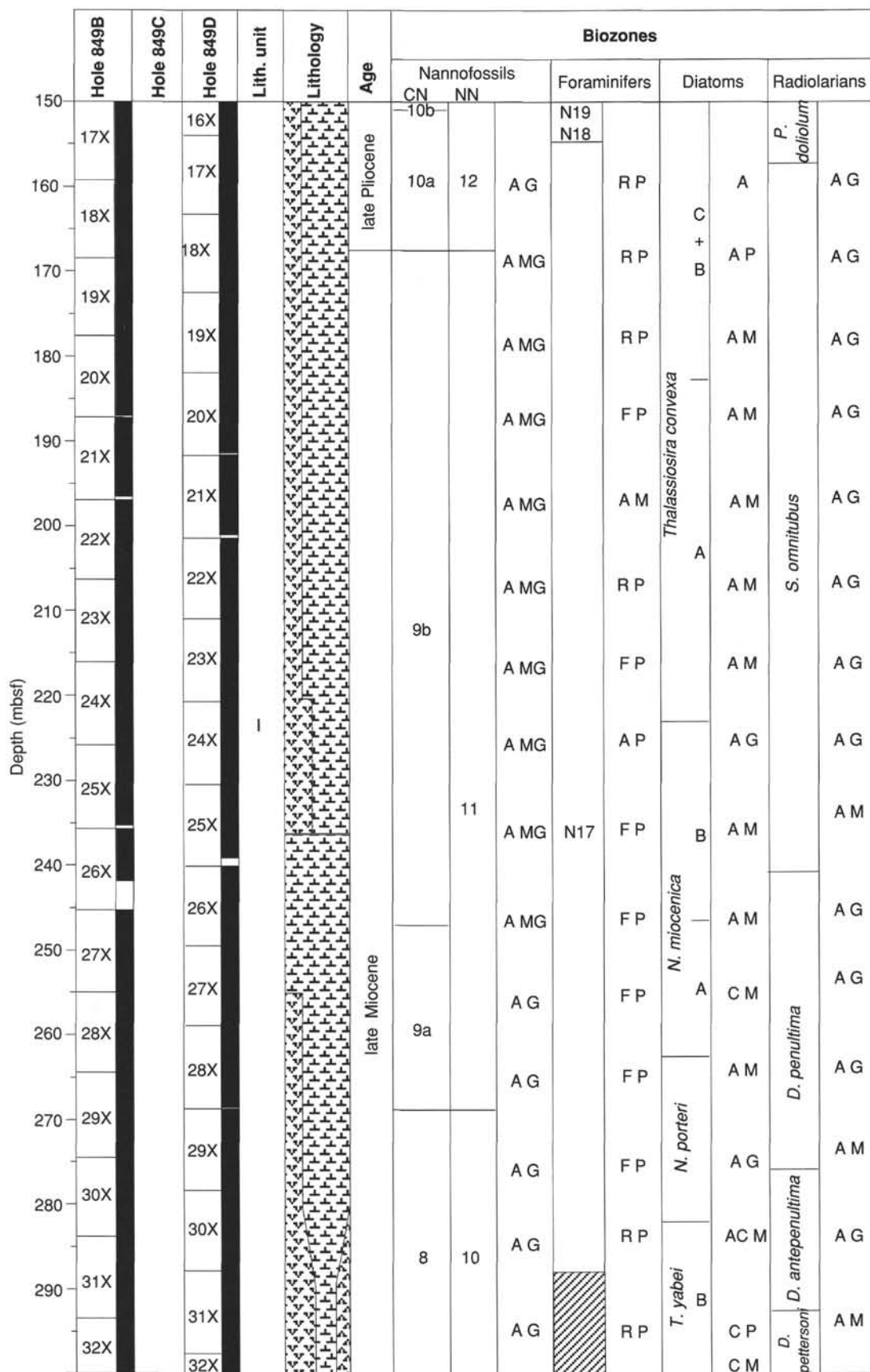
Figure 18 (continued).
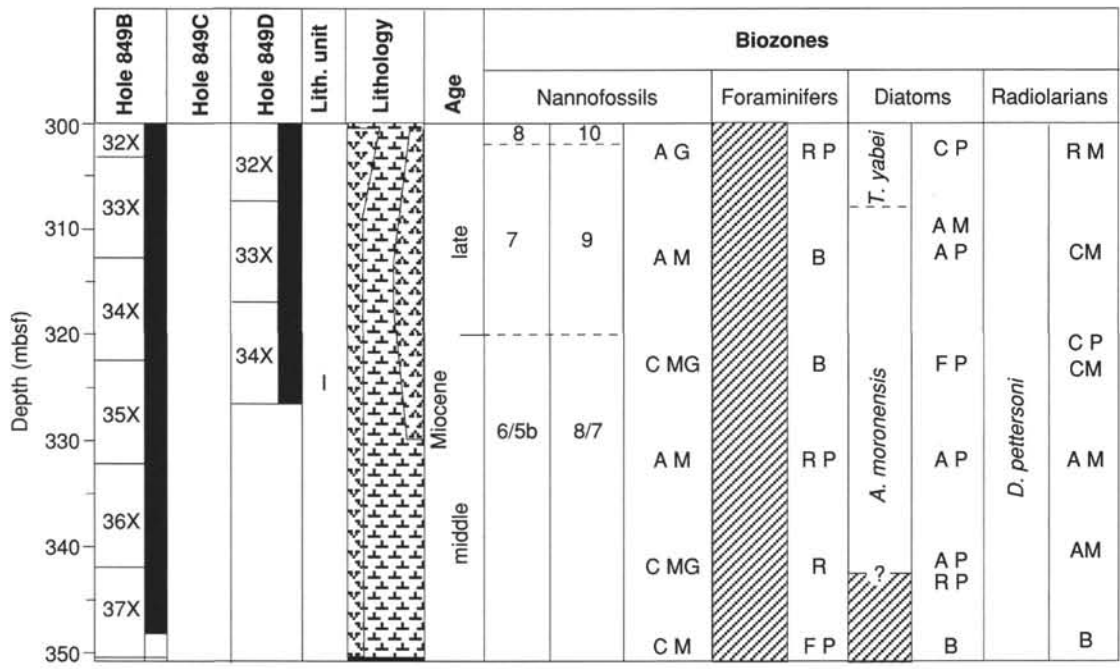
Figure 18 (continued).
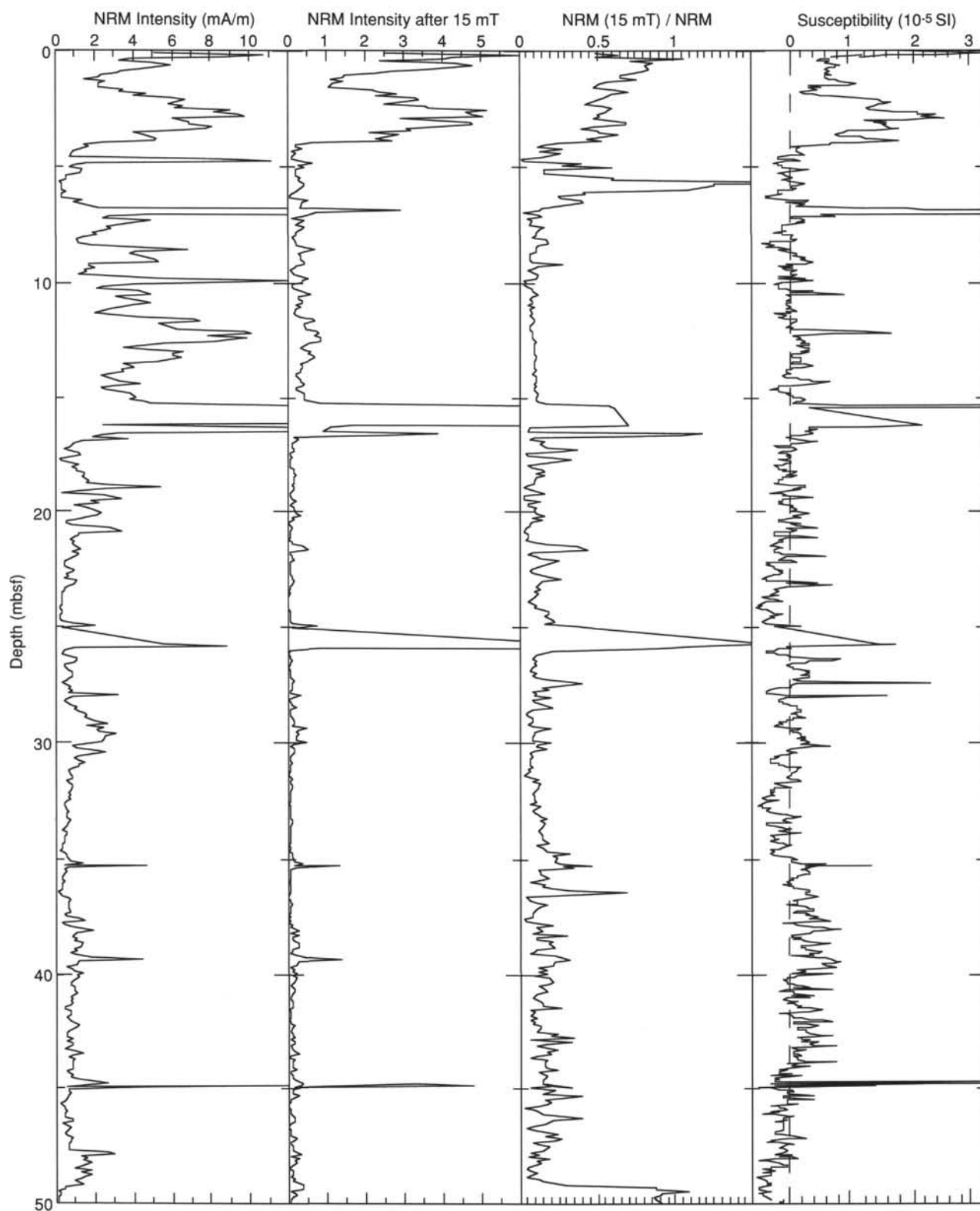
Figure 19. Downhole variations in Hole 849B of the natural remanent magnetization (NRM) intensity, AF demagnetized remanence at 15 mT, ratio of these two parameters, and low-field susceptibility. The NRM(15 mT)/NRM ratio indicates significantly higher remanence stabilities above 4 mbsf.

Table 7. Depths of top and bottom of each core in Site 849 in the composite depth section.

Core	Depth (mbsf)	Core length (m)	Depth (mcd)	Delta (m)
138-849A-1H	0.00–8.69	8.69	0.00–8.69	0.00
138-849B-1H	0.00–6.78	6.78	0.00–6.78	0.00
2H	6.70–15.63	8.93	8.65–17.58	1.95
3H	16.20–25.21	9.01	20.25–29.26	4.05
4H	25.70–35.47	9.77	30.75–40.52	5.05
5H	35.20–45.25	10.05	41.65–51.70	6.45
6H	44.70–54.54	9.84	52.20–62.04	7.50
7H	54.20–64.26	10.06	63.65–73.71	9.45
8H	63.70–73.59	9.89	74.40–84.29	10.70
9H	73.20–83.29	10.09	84.85–94.94	11.65
10H	82.70–92.49	9.79	94.50–104.29	11.80
11H	92.20–102.16	9.96	105.80–115.76	13.60
12H	101.70–111.73	10.03	116.15–126.18	14.45
13H	111.20–121.09	9.89	127.75–137.64	16.55
14X	120.70–125.16	4.46	138.70–143.16	18.00
15X	130.30–139.71	9.41	149.60–159.01	19.30
16X	140.00–149.53	9.53	160.50–170.03	20.50
17X	149.70–159.44	9.74	172.65–182.39	22.95
18X	159.30–168.74	9.44	184.25–193.69	24.95
19X	168.50–178.23	9.73	194.90–204.63	26.40
20X	177.70–187.16	9.46	206.55–216.01	28.85
21X	187.30–196.61	9.31	217.20–226.51	29.90
22X	197.00–206.65	9.65	228.15–237.80	31.15
23X	206.60–216.34	9.74	238.70–248.44	32.10
24X	216.30–226.12	9.82	249.20–259.02	32.90
25X	226.00–235.25	9.25	260.05–269.30	34.05
26X	235.70–242.00	6.30	269.95–276.25	34.25
27X	245.30–254.96	9.66	277.10–286.76	31.80
28X	255.00–264.68	9.68	289.15–298.83	34.15
29X	264.70–274.38	9.68	299.10–308.78	34.40
30X	274.30–283.87	9.57	308.60–318.17	34.30
31X	283.90–293.69	9.79	319.95–329.74	36.05
32X	293.60–303.37	9.77	330.60–340.37	37.00
33X	303.20–313.06	9.86	341.20–351.06	38.00
34X	312.90–322.65	9.75	351.80–361.55	38.90
35X	322.60–332.48	9.88	362.45–372.33	39.85
36X	332.20–342.01	9.81	372.05–381.86	39.85
37X	341.80–348.24	6.44	381.65–388.09	39.85
138-849C-1H	1.00–10.68	9.68	1.75–11.43	0.75
2H	10.50–20.45	9.95	13.50–23.45	3.00
3H	20.00–29.26	9.26	26.40–35.66	6.40
4H	29.50–37.83	8.33	36.60–44.93	7.10
5H	39.00–49.03	10.03	47.15–57.18	8.15
6H	48.50–57.40	8.90	58.10–67.00	9.60
7H	58.00–68.03	10.03	68.95–78.98	10.95
8H	67.50–77.44	9.94	79.30–89.24	11.80
9H	77.00–86.58	9.58	89.60–99.18	12.60
10H	86.50–96.62	10.12	100.95–111.07	14.45
11H	96.00–105.88	9.88	111.20–121.08	15.20
138-849D-1H	4.00–8.36	4.36	7.30–11.66	3.30
2H	13.50–22.97	9.47	17.40–26.87	3.90
3H	23.00–32.79	9.79	26.85–36.64	3.85
4H	32.50–41.48	8.98	39.05–48.03	6.55
5H	42.00–51.90	9.90	50.45–60.35	8.45
6H	51.50–60.92	9.42	60.75–70.17	9.25
7H	61.00–70.93	9.93	70.45–80.38	9.45
8H	70.50–79.20	8.70	81.60–90.30	11.10
9H	80.00–89.76	9.76	92.90–102.66	12.90
10H	89.50–99.05	9.55	103.75–113.30	14.25
11H	99.00–108.90	9.90	113.85–123.75	14.85
12X	108.50–117.31	8.81	124.40–133.21	15.90
13X	115.50–124.08	8.58	132.70–141.28	17.20
14X	125.10–134.57	9.47	143.00–152.47	17.90
15X	134.80–144.41	9.61	155.30–164.91	20.50
16X	144.50–154.20	9.70	167.10–176.80	22.60
17X	154.10–163.84	9.74	178.80–188.54	24.70
18X	163.30–173.18	9.88	190.70–200.58	27.40
19X	172.50–182.23	9.73	201.10–210.83	28.60
20X	182.10–191.70	9.60	213.00–222.60	30.90
21X	191.80–201.14	9.34	223.30–232.64	31.50
22X	201.40–211.09	9.69	234.50–244.19	33.10
23X	211.10–220.86	9.76	245.00–254.76	33.90

Table 7 (continued).

Core	Depth (mbsf)	Core length (m)	Depth (mcd)	Delta (m)
24X	220.80–230.53	9.73	257.15–266.88	36.35
25X	230.50–239.16	8.66	266.85–275.51	36.35
26X	240.10–249.73	9.63	276.10–285.73	36.00
27X	249.80–259.27	9.47	286.45–295.92	36.65
28X	259.00–268.44	9.44	296.85–306.29	37.85
29X	268.60–278.44	9.84	306.95–316.79	38.35
30X	278.30–288.07	9.77	317.80–327.57	39.50
31X	288.00–297.70	9.70	327.50–337.20	39.50
32X	297.70–307.49	9.79	338.60–348.39	40.90
33X	307.40–317.31	9.91	349.10–359.01	41.70
34X	317.00–326.84	9.84	360.80–370.64	43.80

See text for details.

Table 8. Control points for sedimentation rates.

| Depth (mcd)	Rate (m/m.y.)	Age (Ma)	Remarks
0		0	Core top
45.3	31.2	1.45	T *Calcidiscus mcintyrei*
105.25	28.4	3.56	T *Reticulofenestra pseudoubilicus*
123.75	25.0	4.3	T *Nitzschia cylindrica*
156.95	92.2	4.66	B *Ceratolithus rugosus*
191.5	108.0	4.98	T *Discoaster quinqueramus*
278.5	60.4	6.42	B *Amaurolithus primus*
303.8	30.6	7.35	T *Actinocyclus ellipiticus* var. *javnicus*
314.75	35.0	7.55	T *Thalassiosira yabei*
337.5	42.6	8.1	T *Stychocoris wolffi*
360.4	12.5	9.94	T *Coccolithus miopelagicus*
388.09	49.4	10.5	Top Zone CN5b (see text)

B = bottom; T = top.
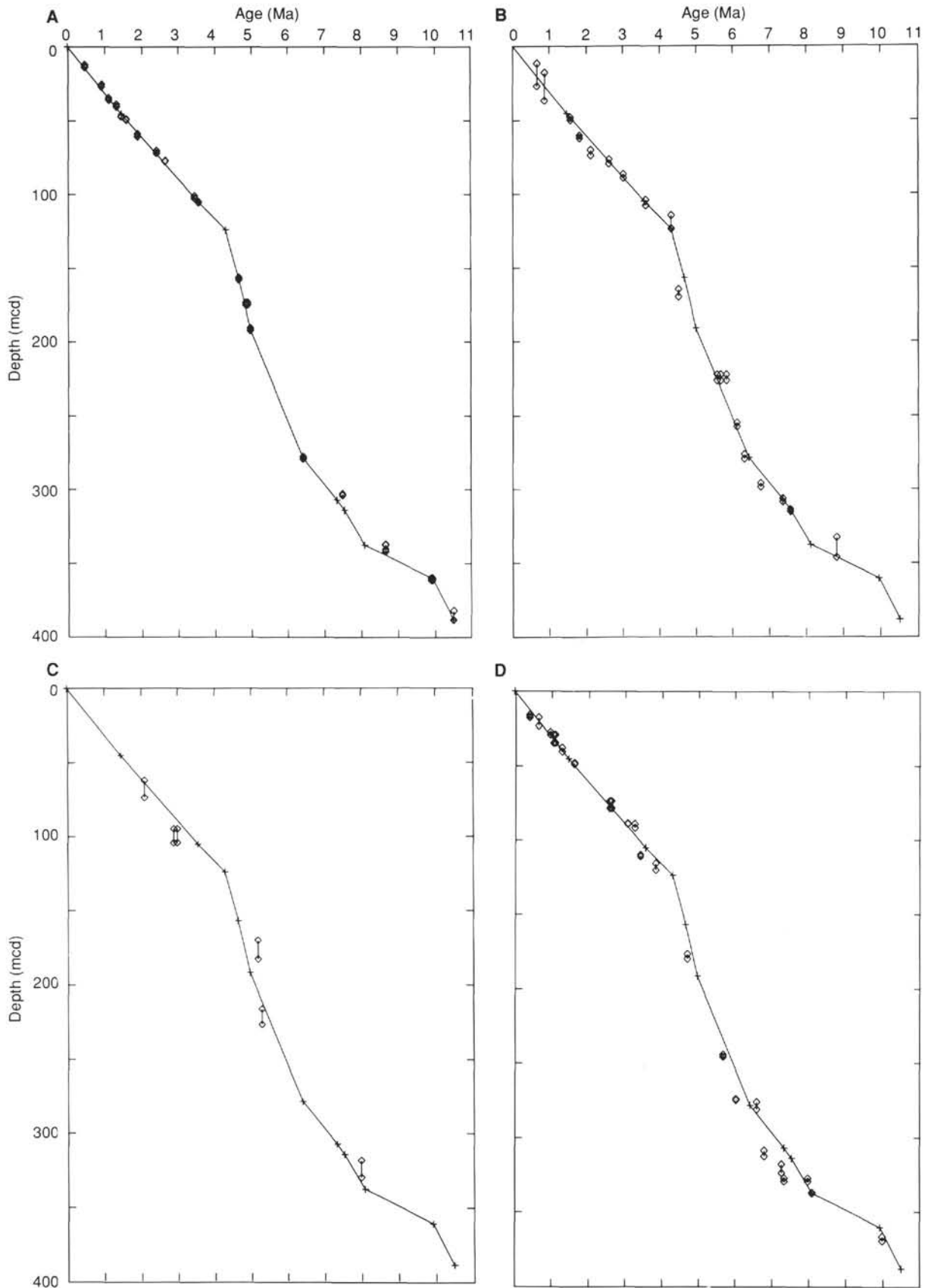
Figure 21. Plot of age vs. depth for Site 849, based on calibration points in Table 8, compared with microfossil datums. **A.** Nannofossils. **B.** Diatoms. **C.** Foraminifers. **D.** Radiolarians. For radiolarians, only datums that appeared consistent in earlier sites of Leg 138 have been shown. Age control points from Table 8 have been indicated by crosses. Depth range of each microfossil datum indicated by distance between paired symbols at each age level.
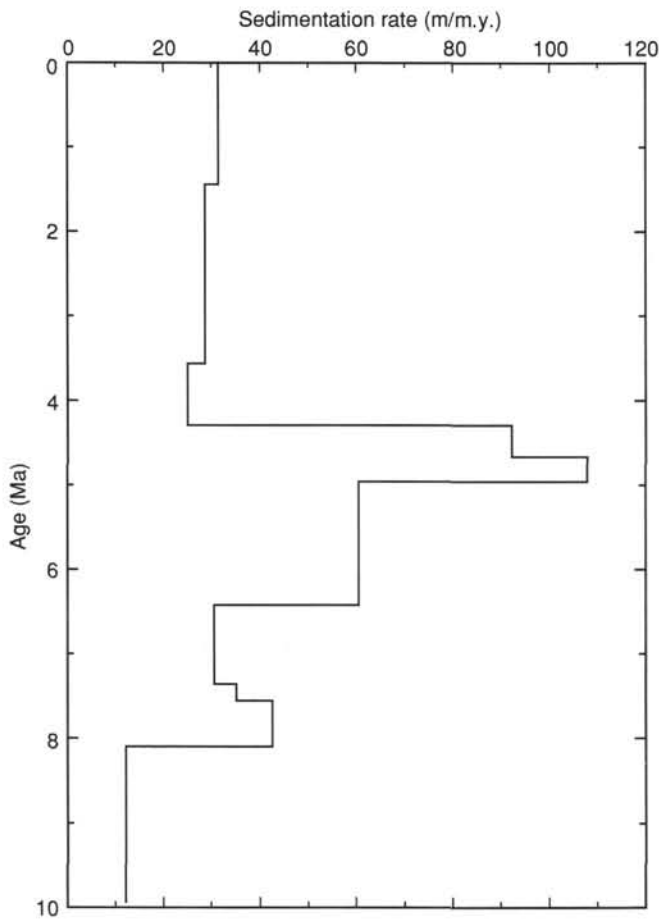
Figure 22. Linear sedimentation rate vs. age, based on data in Table 8.
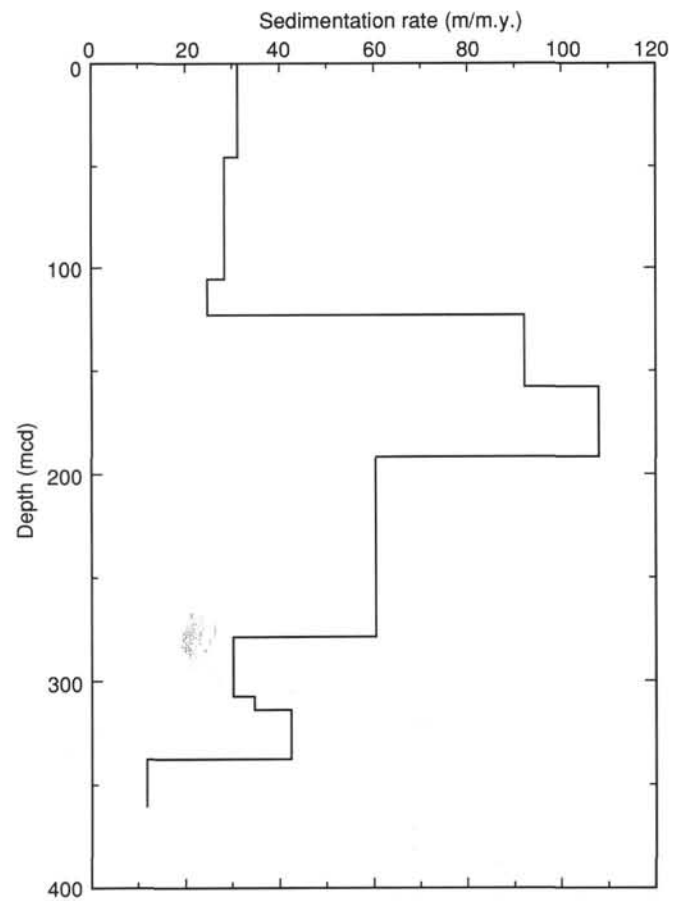
Figure 23. Linear sedimentation rate vs. composite depth, based on data in Table 8.

Table 9. Interstitial-water geochemical data for Holes 849A and 849B.

| Core, section	Interval (cm)	Depth (mbsf)	pH	Salinity (g\kg)	Chloride (mM)	Sodium (mM)	Alkalinity (mM)	Sulfate (mM)	Magnesium (mM)	Calcium (mM)	Potassium (mM)
138-849-A											
1H-1	145–150	1.5	7.46	35.0	555	482	2.866	28.05	54.20	10.28	10.8
1H-3	145–150	4.5	7.12	35.2	556	484	2.751	27.78	53.52	10.32	10.7
1H-5	145–150	7.5	7.31	35.5	557	485	2.892	27.14	52.94	10.10	11.1
138-849-B											
3H-5	145–150	23.7	7.26	35.5	558	483	3.549	26.13	53.55	9.89	10.9
6H-6	145–150	53.7	7.13	35.5	559	486	4.047	25.69	52.86	9.53	11.2
9H-6	145–150	82.2	7.42	36.0	556	484	4.504	24.93	51.93	9.25	11.1
12H-5	145–150	109.2	7.16	35.5	560	486	4.802	24.08	52.05	9.21	11.1
15X-6	145–150	139.3	7.24	34.8	561	485	5.127	23.37	51.94	9.48	10.9
18X-6	142–150	168.3	7.03	35.5	560	484	5.341	23.22	51.71	9.64	10.6
21X-6	144–150	196.3	7.06	—	562	485	5.533	22.89	51.43	9.75	10.7
24X-6	144–150	225.3	7.36	35.0	563	484	5.747	23.25	52.50	10.05	10.5
27X-6	144–150	254.3	7.06	35.0	555	481	4.203	25.05	51.31	10.92	10.1
30X-6	144–150	283.3	7.06	35.0	561	485	3.995	25.15	52.17	10.94	10.3
32X-6	144–150	302.6	7.14	35.5	556	481	3.510	26.18	52.71	10.97	10.7
33X-6	142–150	312.2	7.28	35.5	560	487	3.133	26.62	52.03	11.08	10.8
34X-6	142–150	321.9	7.18	35.8	559	486	2.458	27.24	52.37	11.14	10.9
35X-6	142–150	331.6	7.23	36.0	559	484	3.340	27.28	53.73	11.23	10.3
36X-6	142–150	341.6	7.33	35.5	560	488	2.942	27.18	52.87	10.48	10.5
37X-3	142–150	346.3	—	37.0	555	484	—	26.93	52.50	10.05	10.2

(—) indicates a missed analysis.
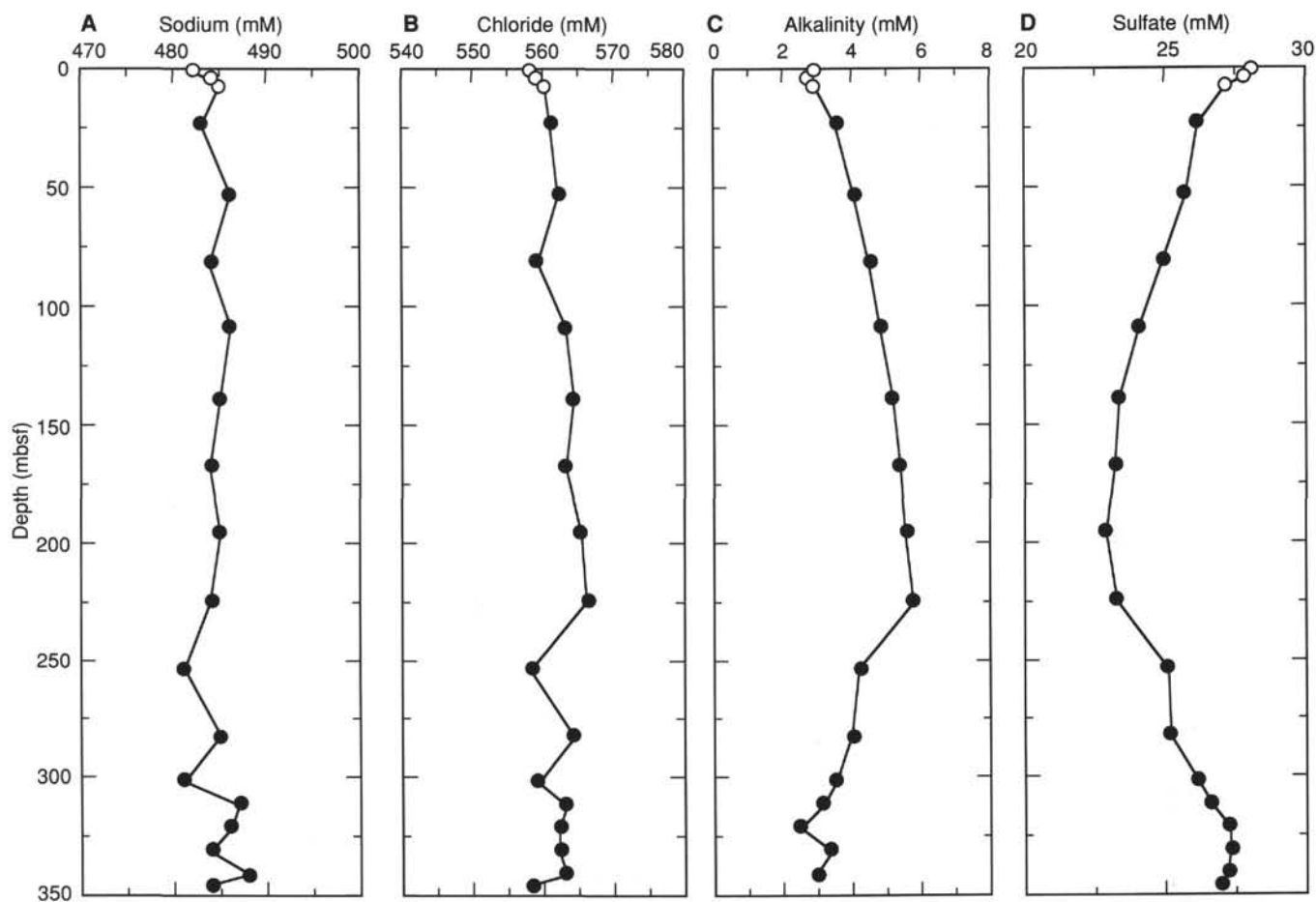
Figure 24. Interstitial-water geochemical data vs. depths (mbsf) for Holes 849A (open circles) and 849B (filled circles). **A.** Sodium. **B.** Chloride. **C.** Alkalinity. **D.** Sulfate.

Table 9 (continued).

Core, section	Strontium (μM)	Lithium (μM)	Silica (μM)	Ammonia (μM)
138-849-A				
1H-1	90	26.1	803	<10
1H-3	99	25.0	883	39
1H-5	127	24.5	955	61
138-849-B				
3H-5	155	21.7	853	111
6H-6	230	18.7	892	178
9H-6	298	15.6	907	230
12H-5	343	13.3	925	257
15X-6	396	11.7	973	255
18X-6	436	10.6	1036	254
21X-6	439	9.6	1005	285
24X-6	450	9.5	1027	302
27X-6	262	8.2	1010	53
30X-6	232	9.3	1042	52
32X-6	199	11.4	1025	48
33X-6	187	13.0	1116	43
34X-6	155	15.9	1023	20
35X-6	147	16.4	1062	13
36X-6	114	20.4	1049	11
37X-3	94.0	34.0	1036	<10
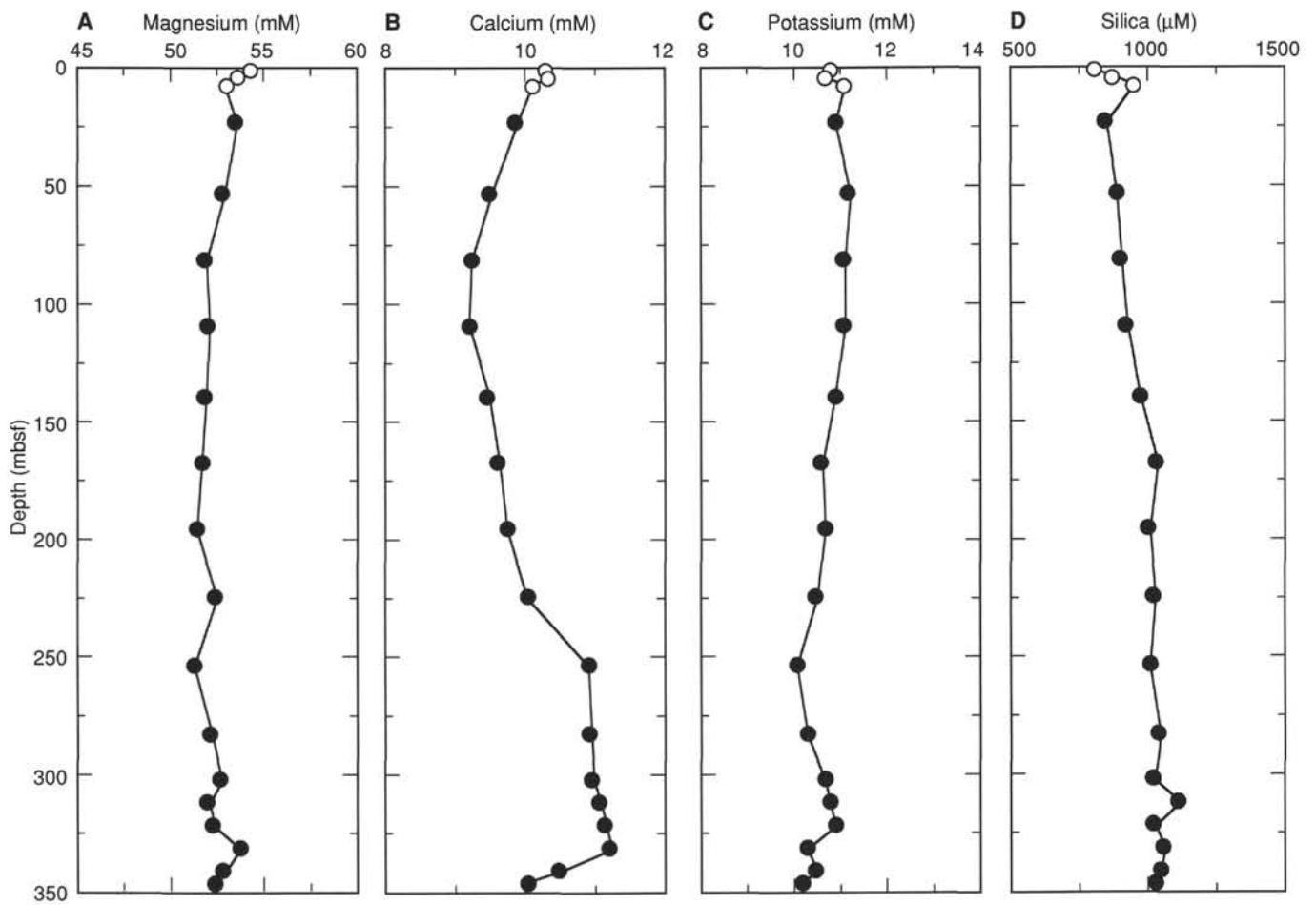
Figure 25. Interstitial-water geochemical data vs. depths (mbsf) for Holes 849A (open circles) and 849B (filled circles). **A.** Magnesium. **B.** Calcium. **C.** Potassium. **D.** Silica.
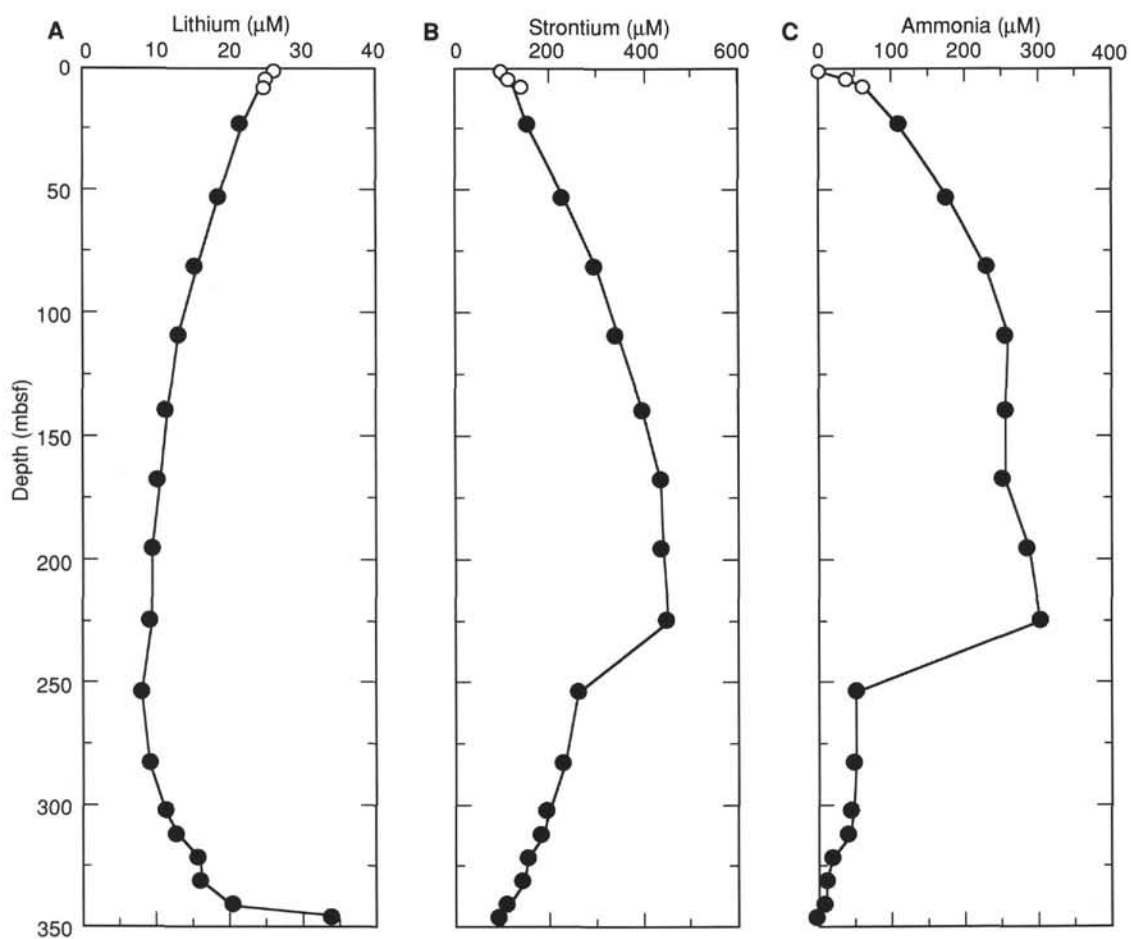
Figure 26. Interstitial-water geochemical data vs. depths (mbsf) for Holes 849A (open circles) and 849B (filled circles). **A.** Lithium. **B.** Strontium. **C.** Ammonia.
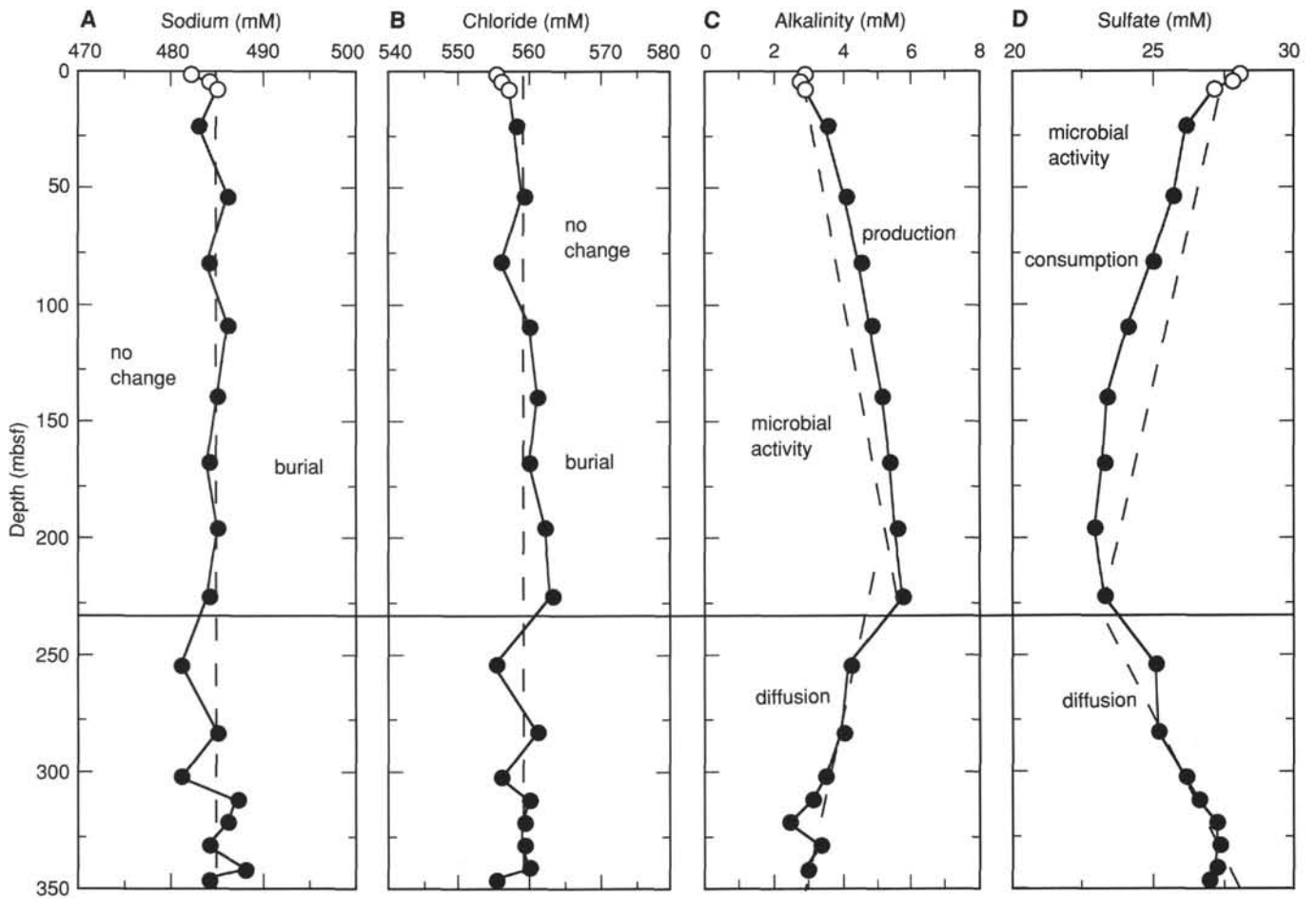
Figure 27. Interstitial-water trends and the geochemical implications of these trends for Holes 849A (open circles) and 849B (filled circles). **A.** Sodium. **B.** Chloride. **C.** Alkalinity. **D.** Sulfate. Horizontal line at 237 mbsf indicates depth of the chert layer.
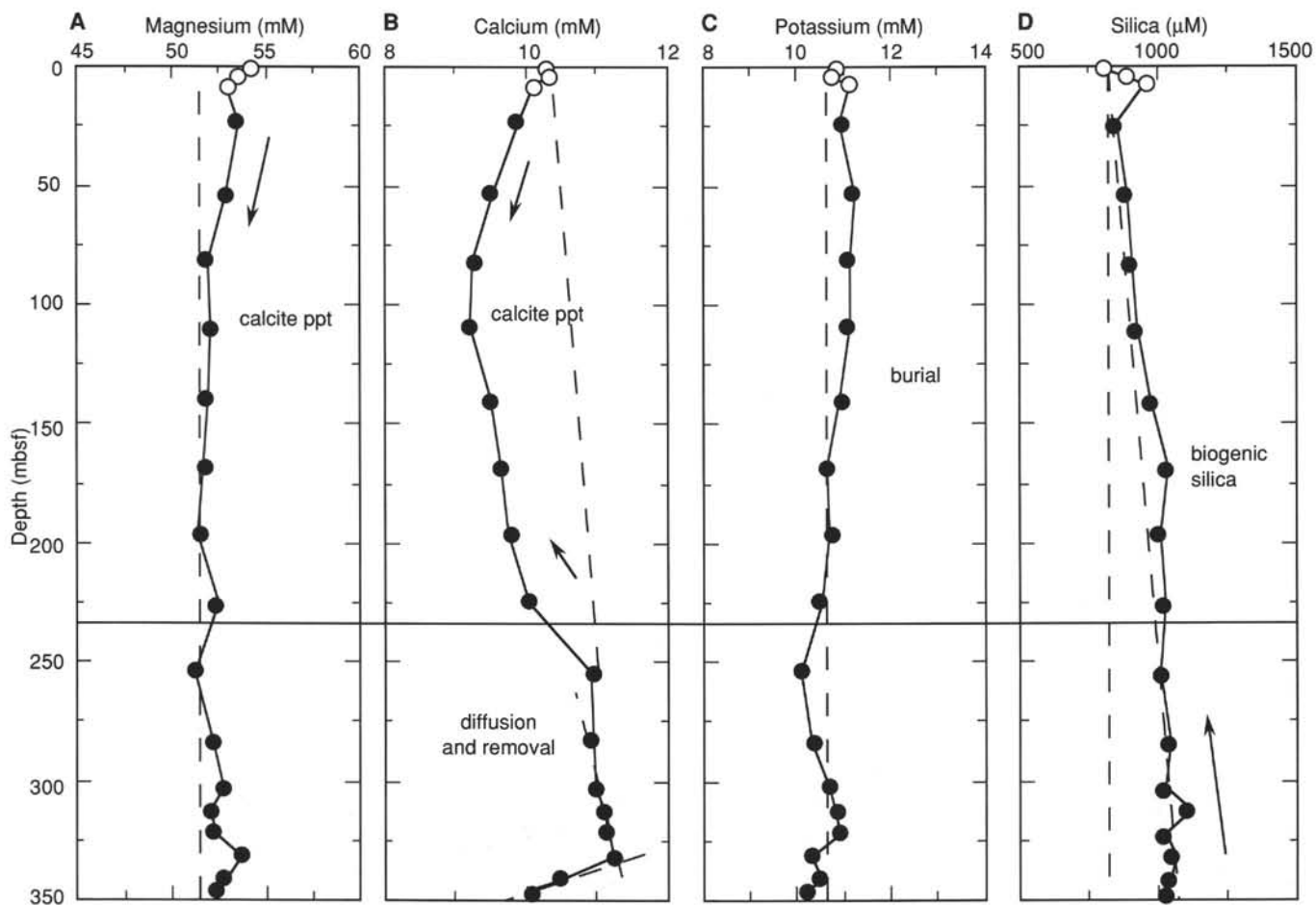
Figure 28. Interstitial-water trends and the geochemical implications of these trends for Holes 849A (open circles) and 849B (filled circles). **A.** Magnesium. **B.** Calcium. **C.** Potassium. **D.** Silica. Horizontal line at 237 mbsf indicates depth of the chert layer.
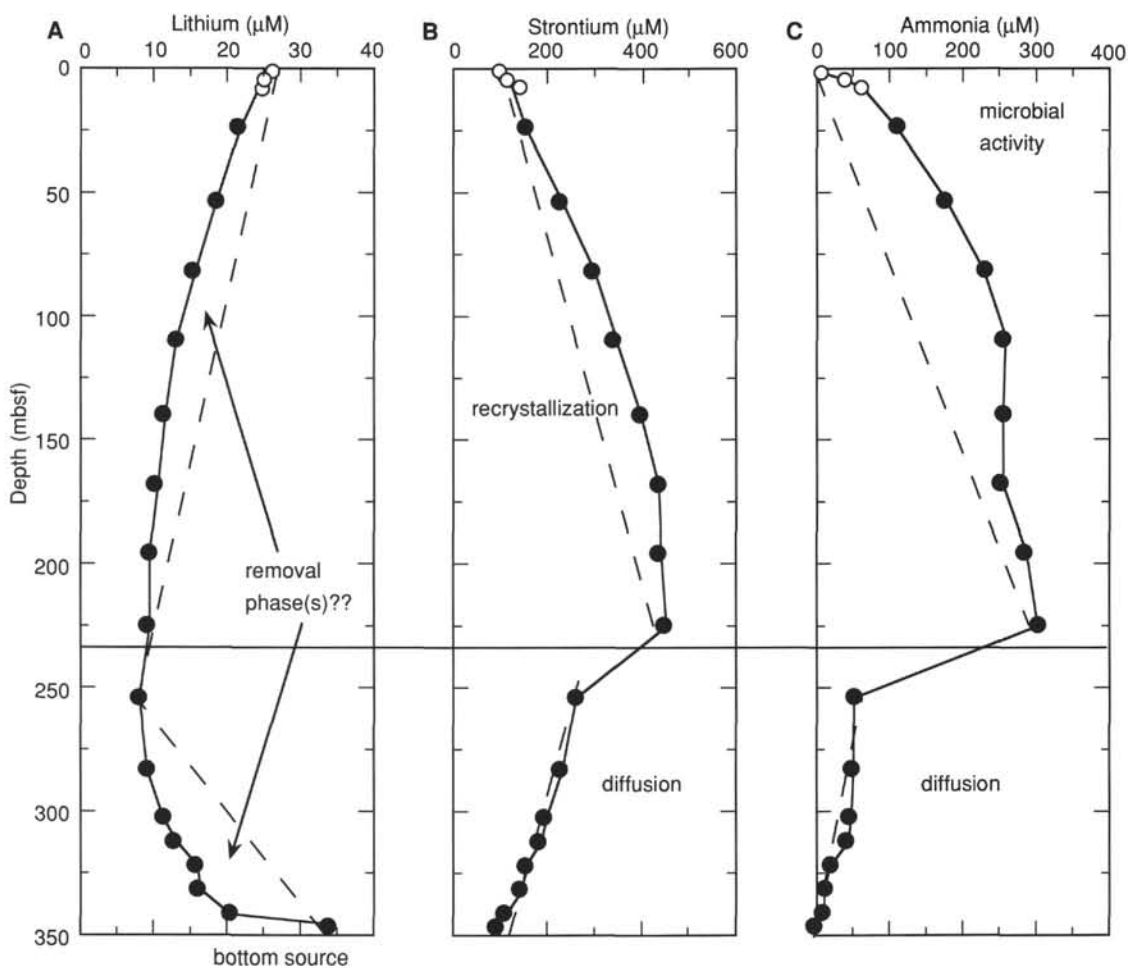
Figure 29. Interstitial-water trends and the geochemical implications of these trends for Holes 849A (open circles) and 849B (filled circles). **A.** Lithium. **B.** Strontium. **C.** Ammonia. Horizontal line at 237 mbsf indicates depth of the chert layer.

Table 11. Duplicate analyses of %CaCO₃ in samples from Site 849.

Core section 138-849B-	Interval (cm)	Depth (mbsf)	Depth (mcd)	First run CaCO₃ (%)	Second run CaCO₃ (%)	Third run CaCO₃ (%)	Absolute value of CaCO₃ (difference)
1H-1	30–32	0.31	0.31	71.64	70.72		0.92
1H-1	102–104	1.03	1.03	82.47	82.72		0.25
1H-3	105–107	4.06	4.06	65.72	66.81		1.08
3H-3	103–105	20.24	24.29	70.97	70.64		0.33
4H-2	103–105	28.24	33.29	89.63	88.38		1.25
6H-3	10–12	47.81	55.31	16.83	17.33		0.50
6H-3	112–114	48.83	56.33	47.06	47.48		0.42
10H-3	105–107	86.76	98.56	73.14	72.05		1.08
11H-1	101–103	93.22	106.82	44.90	42.48		2.42
12H-5	102–104	108.73	123.18	91.46	91.05		0.42
13H-1	103–105	112.24	128.79	35.74	36.82		1.08
13H-2	103–105	113.74	130.29	48.06	48.77		0.71
20X-2	101–103	180.22	209.07	81.55	81.80		0.25
23X-4	103–105	212.14	244.24	56.31	57.06		0.75
26X-1	99–101	236.70	270.95	36.24	36.32		0.08
26X-4	102–104	241.23	275.48	92.71	92.30		0.42
27X-5	105–107	252.36	284.16	66.14	65.78		0.36
29X-6	102–104	273.23	307.63	59.98	62.06		2.08
30X-1	102–104	275.33	309.63	76.97	77.80		0.83
30X-2	102–104	276.83	311.13	66.81	66.14		0.67
30X-3	102–104	278.33	312.63	83.38	82.63		0.75
31X-6	103–105	292.44	328.49	61.39	61.39		0.00
32X-2	102–104	296.13	333.13	61.64	63.64		2.00
32X-3	102–104	297.63	334.63	44.57	45.15		0.58
33X-2	103–105	305.74	343.74	14.91	14.68		0.23
33X-4	103–105	308.74	346.74	3.58	4.25		0.67
35X-1	105–107	323.66	363.51	73.64	73.39		0.25
35X-2	33–35	324.44	364.29	84.10	83.60		0.51
35X-2	104–106	325.15	365.00	60.23	60.65		0.43
35X-3	31–33	325.92	365.77	57.73	56.77		0.96
35X-3	106–108	326.67	366.52	41.40	39.98		1.42
35X-4	30–32	327.41	367.26	45.57	43.95		1.62
35X-4	101–103	328.12	367.97	59.81	59.55		0.25
35X-5	41–43	329.02	368.87	47.31	46.82		0.50
35X-5	114–116	329.75	369.60	39.40	41.65	43.44	4.04
35X-6	31–33	330.42	370.27	41.40	42.26		0.86
35X-6	77–79	330.88	370.73	41.07	43.82	42.77	2.75
35X-7	12–14	331.73	371.58	38.23	38.55		0.32
36X-1	12–14	332.33	372.18	45.29	46.59		1.29
36X-1	85–87	333.06	372.91	46.23	46.40		0.17
36X-5	109–111	339.30	379.15	77.30	76.39		0.91
36X-6	127–129	340.98	380.83	83.27	83.72		0.45
						Average	0.88

The average difference between the original and the duplicate analysis was 0.9% for %CaCO₃. The average value of the original and the duplicate analysis is reported in Table 10 (CD ROM).

Table 12. Averages values of sedimentary parameters calculated over time intervals defined by chronostratigraphic levels.

Depth (mcd)	Age (Ma)	Mean CaCO$_3$ (%)	Mean C$_{org}$ (%)	Sed. rate (m/m.y.)	Mean DBD (g/cm^3)	Mean Bulk MAR (g/cm^2/k.y.)	Mean CaCO$_3$ MAR (g/cm^2/k.y.)	Mean Non-CaCO$_3$ MAR (g/cm^2/k.y.)	Mean C$_{org}$ MAR (mg/cm^2/k.y.)
0.00	0.00								
		79.51	0.09	32.37	0.63	2.03	1.61	0.42	1.9
46.93	1.45								
		73.60	0.10	27.59	0.65	1.80	1.33	0.48	1.8
105.15	3.56								
		78.07	0.08	25.14	0.77	1.92	1.50	0.42	1.4
123.75	4.30								
		64.05	0.17	92.22	0.64	5.90	3.78	2.12	10.3
156.95	4.66								
		74.79	0.06	106.41	0.72	7.62	5.70	1.92	4.4
191.00	4.98								
		75.21	0.08	57.14	0.78	4.47	3.36	1.11	3.6
255.00	6.10								
		66.85	0.09	73.44	0.72	5.26	3.52	1.75	4.8
278.50	6.42								
		76.24	0.06	30.65	0.86	2.62	2.00	0.62	1.5
307.00	7.35								
		71.18	0.22	35.00	0.76	2.67	1.90	0.77	5.7
314.00	7.55								
		76.48	0.10	42.64	0.88	3.75	2.86	0.88	3.6
337.45	8.10								
		50.41	0.16	12.47	0.61	0.76	0.38	0.38	1.2
360.39	9.94								
		62.43	0.07	49.46	0.77	3.79	2.37	1.42	2.6
388.09	10.50								

DBD = Dry-Bulk Density; MAR = Mass Accumulation Rate.

Table 13. Concentrations of methane in samples from Hole 849B.

Core, section	Interval (cm)	Depth (mbsf)	Methane (μL/L)
138-849B-			
1H-4	145–150	5.95	5.8
2H-5	145–150	14.15	8.1
3H-5	140–145	23.60	14.3
4H-6	145–150	34.65	15.8
5H-6	145–150	44.15	19.0
6H-6	140–145	53.60	23.0
7H-6	145–150	63.15	20.0
8H-6	145–150	72.65	19.9
9H-6	140–145	82.10	19.9
10H-7	0–5	91.70	25.9
11H-6	145–150	101.15	22.5
12H-5	140–145	109.10	27.9
13H-6	145–150	120.15	35.0
14X-3	124–129	124.94	20.7
15X-6	140–145	139.20	28.9
16X-6	145–150	148.95	33.8
17X-6	145–150	158.65	34.3
18X-6	137–142	168.17	30.0
19X-6	145–150	177.45	32.1
20X-6	145–150	186.65	37.6
21X-6	140–145	196.20	36.7
22X-6	145–150	205.95	34.7
23X-6	145–150	215.55	42.2
24X-6	139–144	225.19	46.1
25X-6	145–150	234.95	22.5
26X-4	145–150	241.65	8.6
27X-6	139–144	254.19	10.7
28X-6	145–150	263.95	9.7
29X-6	145–150	273.65	8.4
30X-6	139–144	283.19	9.2
31X-6	145–150	292.85	7.3
32X-6	139–144	302.49	4.7
33X-5	137–142	312.07	2.8
34X-6	137–142	321.77	2.8
35X-6	137–142	331.41	1.6
36X-6	137–142	341.07	0.5
37X-4	145–150	347.75	3.4

Table 18. Depth intervals over which logging data are considered reliable.

Log type	Depth in Hole 849B (mbsf)[a]
Resistivity	53.9–346.2
Bulk density	61.2–338.3
Sonic velocity	48.7–327.9
Sonic waveforms	48.7–327.9
Gamma-ray/U-Th-K	0–348.3
Aluminum	0–337.5
Geochemistry	0–345.7
Caliper	61.3–350.2
Formation microscanner	108.6–350.2
LDGO temperature	0–346.2

[a]Assumes depth below rig floor is 3850.8 m; mbsf was calculated assuming mbrf (meters below rig floor) = 3850.8; Geophysical logs are shifted -1.47 m; geochemical logs are shifted -3.16 m; FMS logs are shifted 1.77 m.
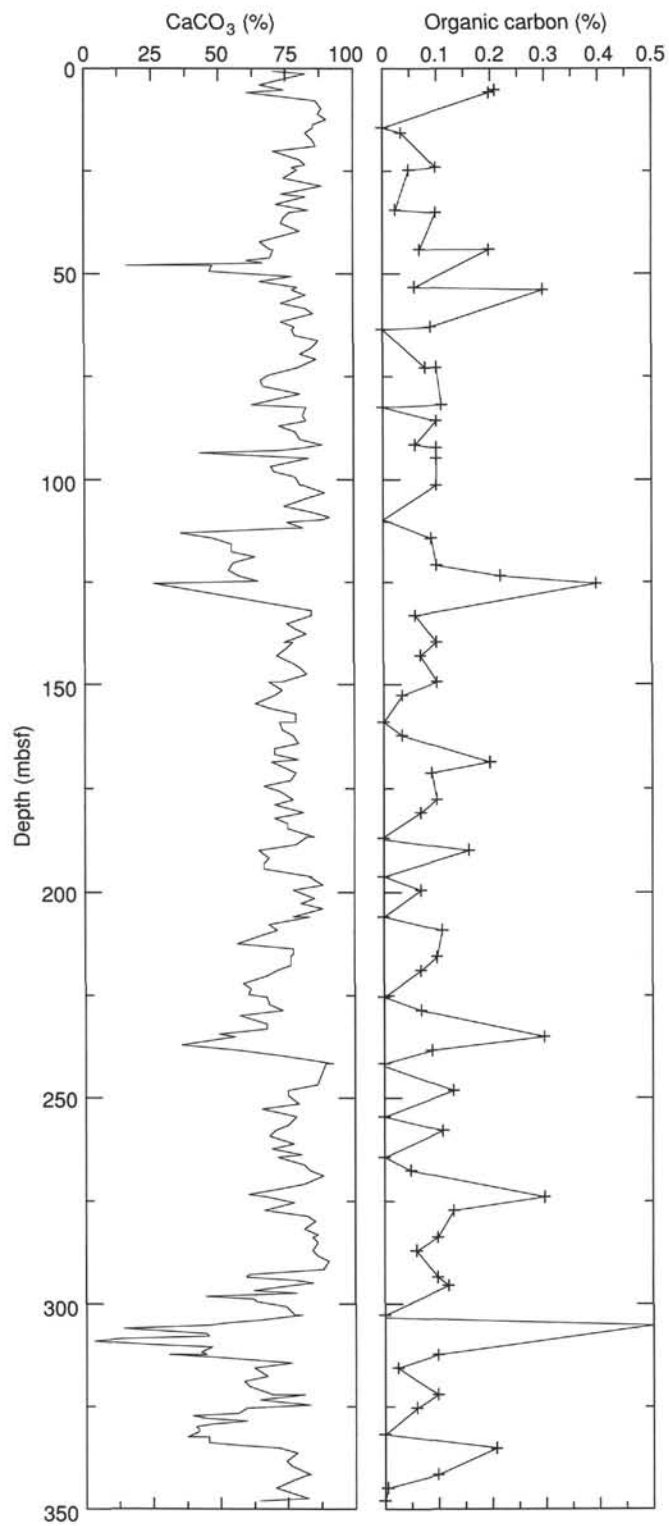
Figure 30. Downhole records of percentages of CaCO₃ and C_org vs. ODP depth for Hole 849B.
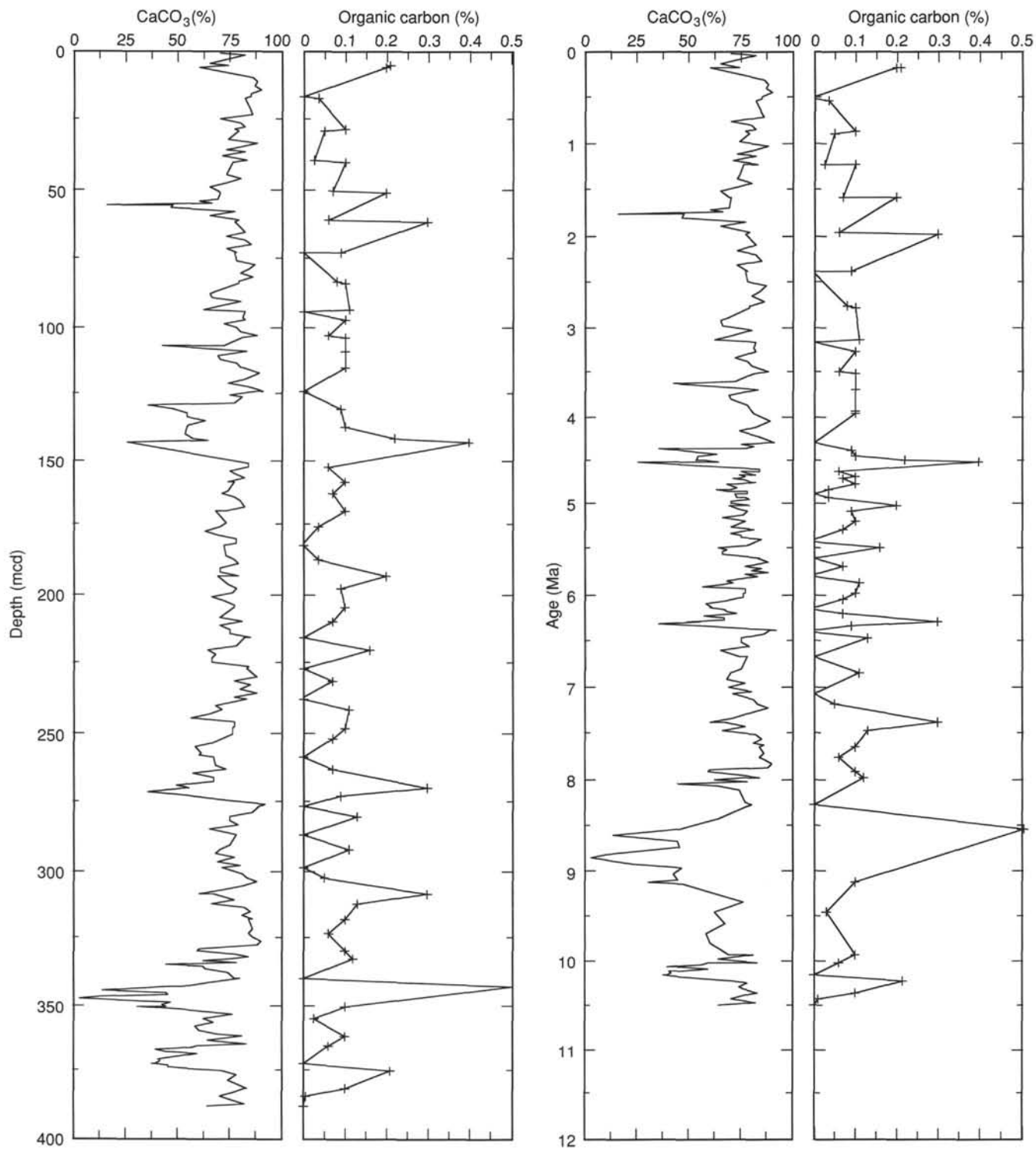
Figure 31. Percentages of CaCO$_3$ and C$_{org}$ vs. composite depth and age for Hole 849B.
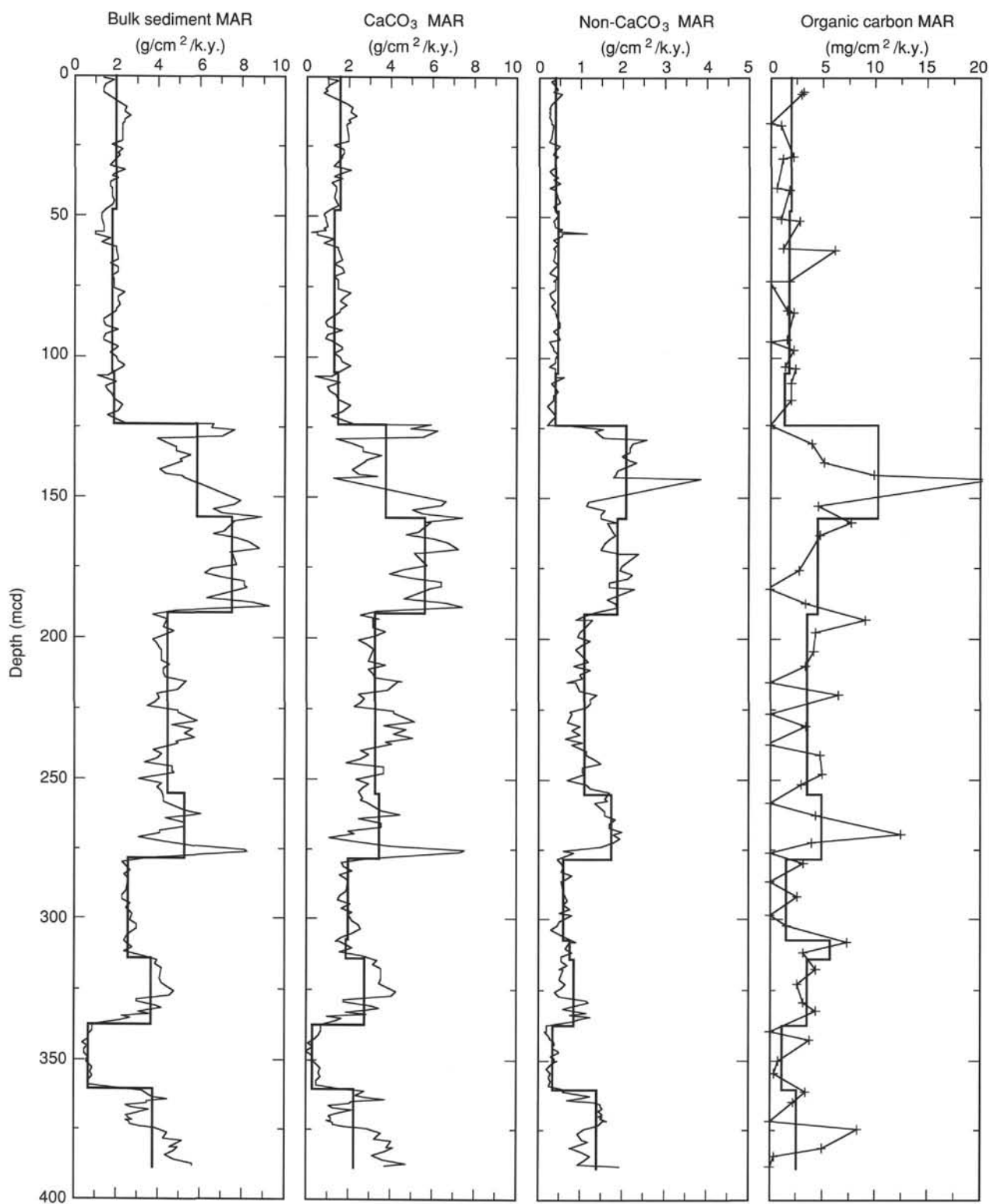
Figure 32. Mass accumulation rates of bulk sediment, CaCO₃, non-CaCO₃, and C_org sedimentary components vs. composite depth at Site 849. Note different units for C_org. Thick line indicates mean value between each stratigraphic datum plane from data in Table 8. Thin line shows discrete accumulation rates calculated for each sample.
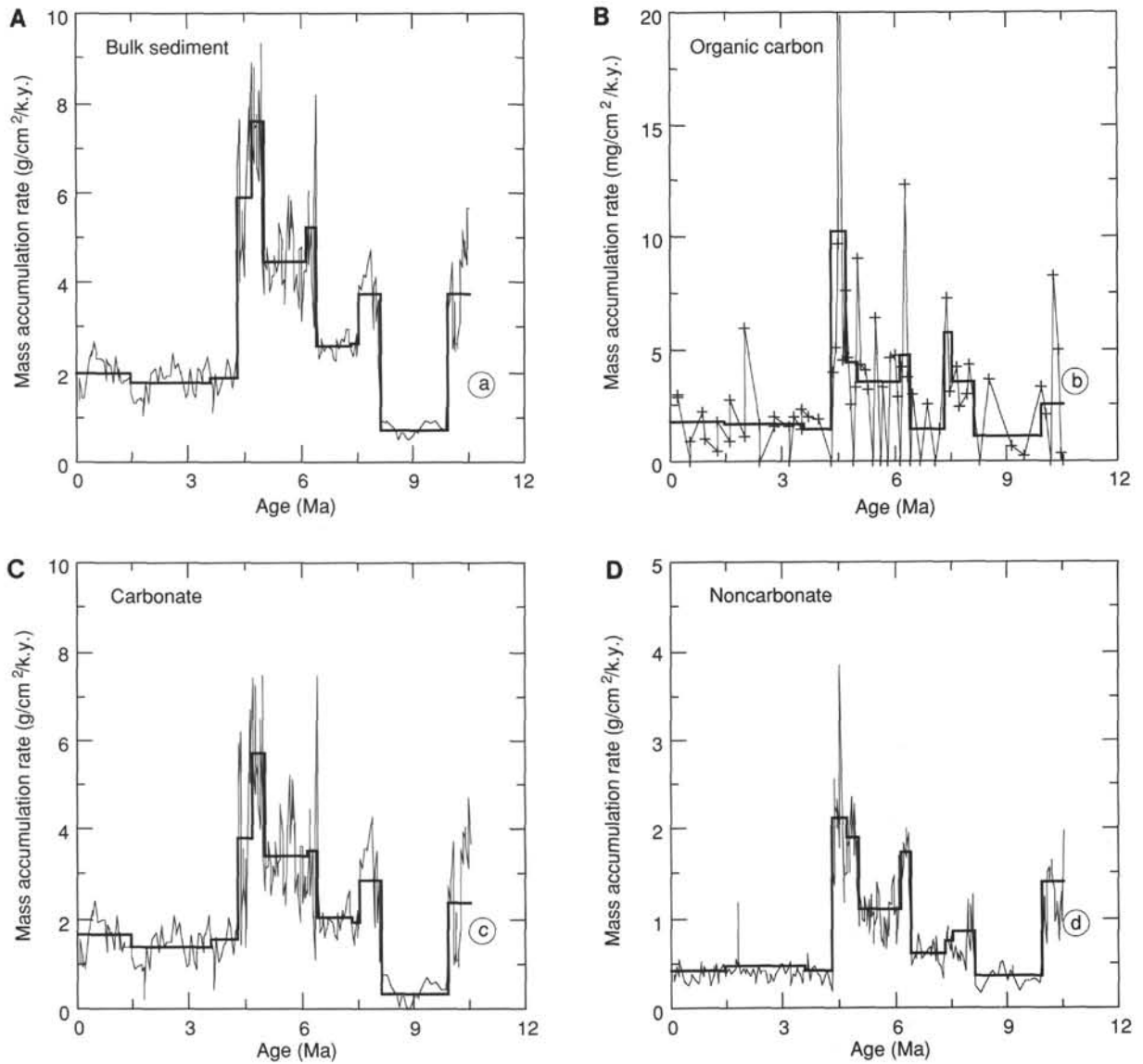
Figure 33. Accumulation rates of bulk sediment (**A**), C$_{org}$ (**B**), CaCO$_3$ (**C**), and non-CaCO$_3$ (**D**) vs. age in sediments from Site 849. Thick line indicates mean value between each stratigraphic datum plane from data in Table 8. Thin line shows discrete accumulation rates calculated for each sample.

Table 19. Means and standard deviations of log properties.

	Log Subunit 1A	High carbonate interval (120–136 mbsf)	Log Subunit 1B	High carbonate interval (240–304 mbsf)
Geophysical tool string				
Intermediate resistivity (ohm-m)	0.65 ± 0.053	0.71 ± 0.06	0.74 ± 0.07	0.76 ± 0.045
Shallow resistivity (ohm-m)	0.59 ± 0.051	0.66 ± 0.06	0.67 ± 0.055	0.7 ± 0.046
Gamma-ray (API units)	5.32 ± 1.34	5.85 ± 0.86	5.46 ± 1.25	5.15 ± 1.2
Wet-bulk density (g/cm^3)	1.47 ± 0.093	1.55 ± 0.11	1.56 ± 0.094	1.6 ± 0.061
Velocity (km/s)	1.53 ± .047	1.62 ± 0.052	1.67 ± 0.063	1.73 ± 0.058
Calculated porosity (%)	76.8 ± 9.2	64 ± 7.2	66.7 ± 4.6	63.4 ± 3.5
Geochemical tool string				
Calcium-yield	0.09 ± 0.031	0.12 ± 0.02	0.10 ± 0.034	0.12 ± 0.031
Silicon-yield	0.01 ± 0.017	0.005 ± 0.014	0.0012 ± 0.017	0.01 ± 0.016
Hydrogen-yield	0.28 ± 0.009	0.27 ± 0.01	0.27 ± 0.01	0.27 ± 0.008
PHIG (Porosity estimate)	1598 ± 1421	220 ± 421	848 ± 1042	284 ± 689
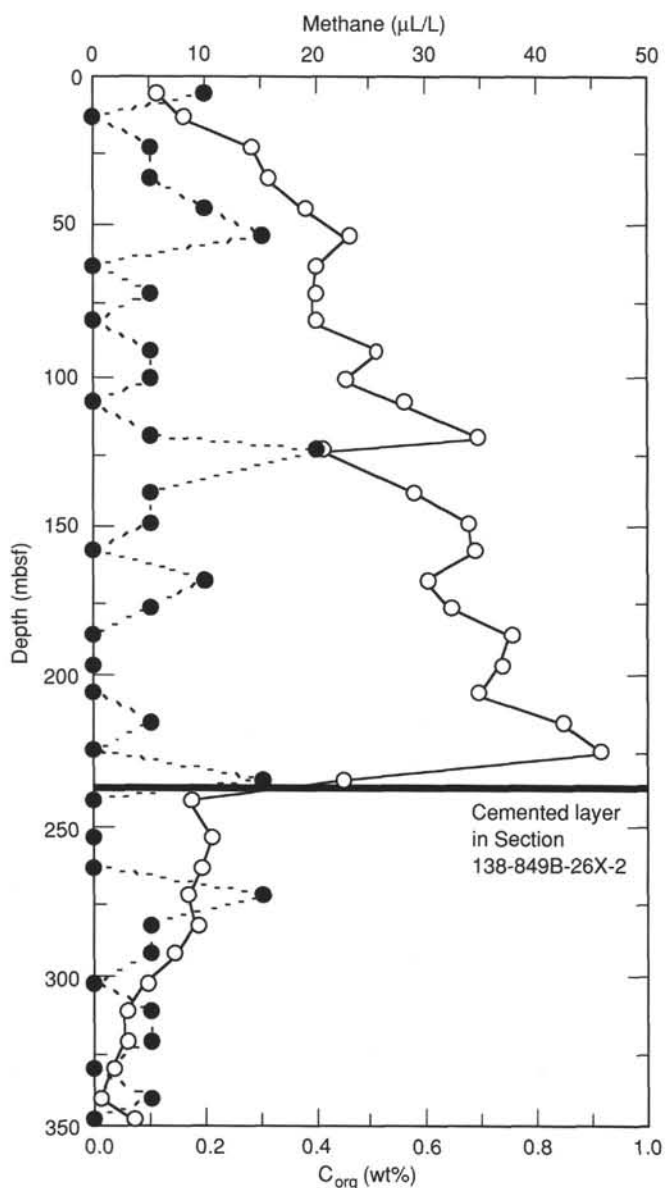
Figure 34. Concentrations of sorbed methane (circles) and C_{org} (dots) vs. depth in Hole 849B. A chert layer recognized as pebbles in Core 138-849B-26X marks the position of a distinct boundary that separates an upper interval (characterized by ongoing diagenesis) and a lower sediment interval (unaffected by diagenesis). The steep gradient across the inferred cemented layer implies that no or little exchange occurs between the two regimes.

Table 20. Means and standard deviations of delta density (log density minus laboratory density) values.

	Log density minus GRAPE density		Log density minus gravimetric density	
	Mean	Std. dev.	Mean	Std. dev.
Subunit 1A	−0.084	0.1	−0.0003	0.111
Subunit 1B	−0.0043	0.064	0.041	0.061
High carbonate interval (240–304 mbsf)	0.0087	0.056	0.038	0.055
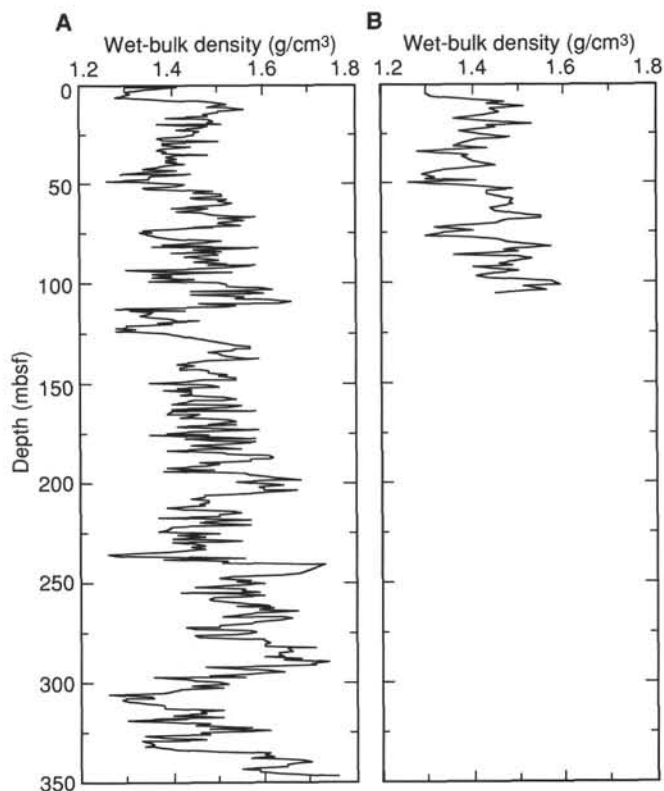
Figure 35. Wet-bulk density vs. depth for Holes 849B (**A**) and 849C (**B**).
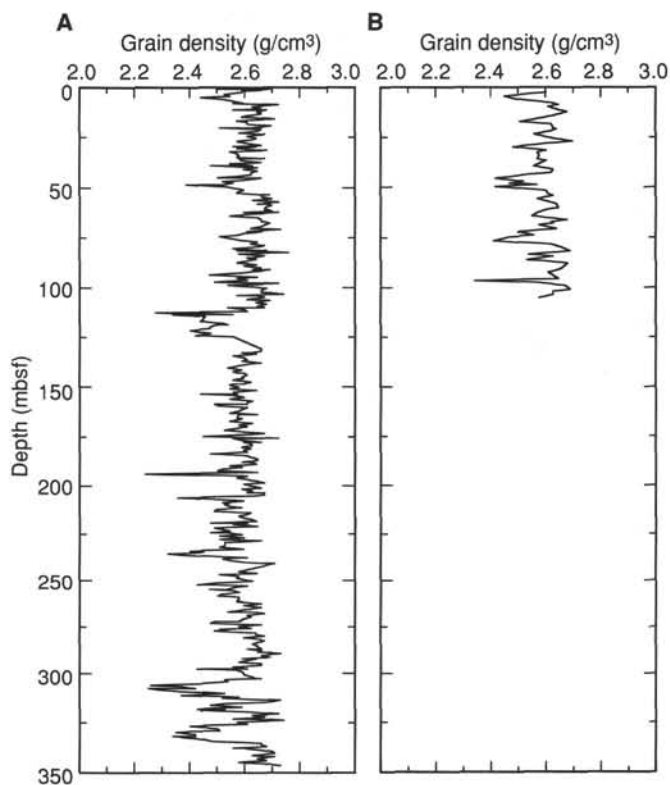
Figure 36. Grain density vs. depth for Holes 849B (**A**) and 849C (**B**).
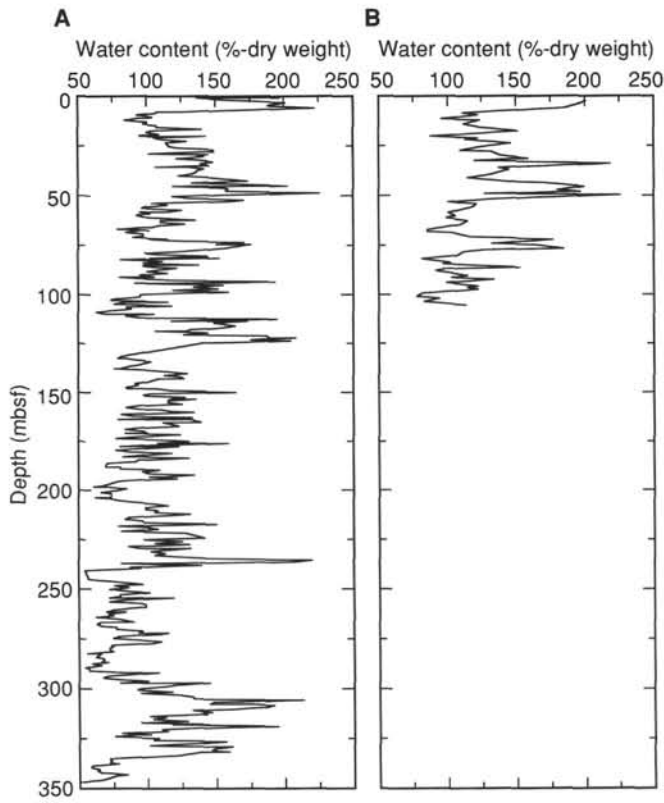
Figure 37. Water content vs. depth for Holes 849B (**A**) and 849C (**B**).
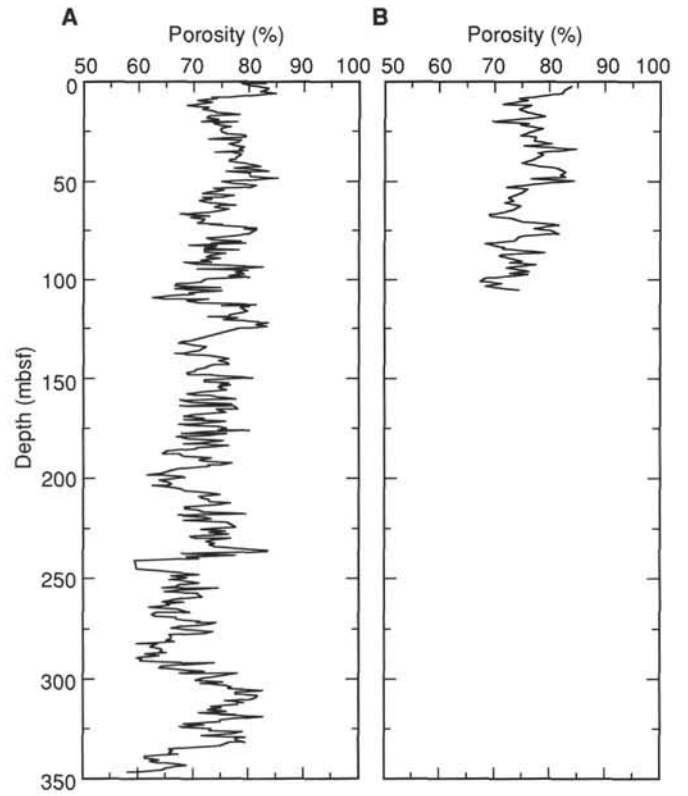
Figure 38. Porosity vs. depth for Holes 849B (**A**) and 849C (**B**).
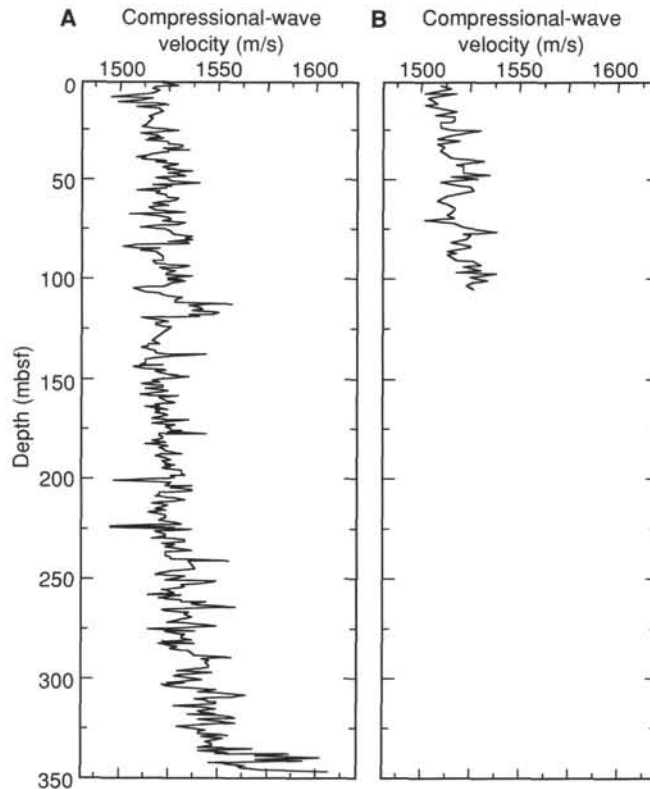
Figure 39. Velocity vs. depth for Holes 849B (**A**) and 849C (**B**).
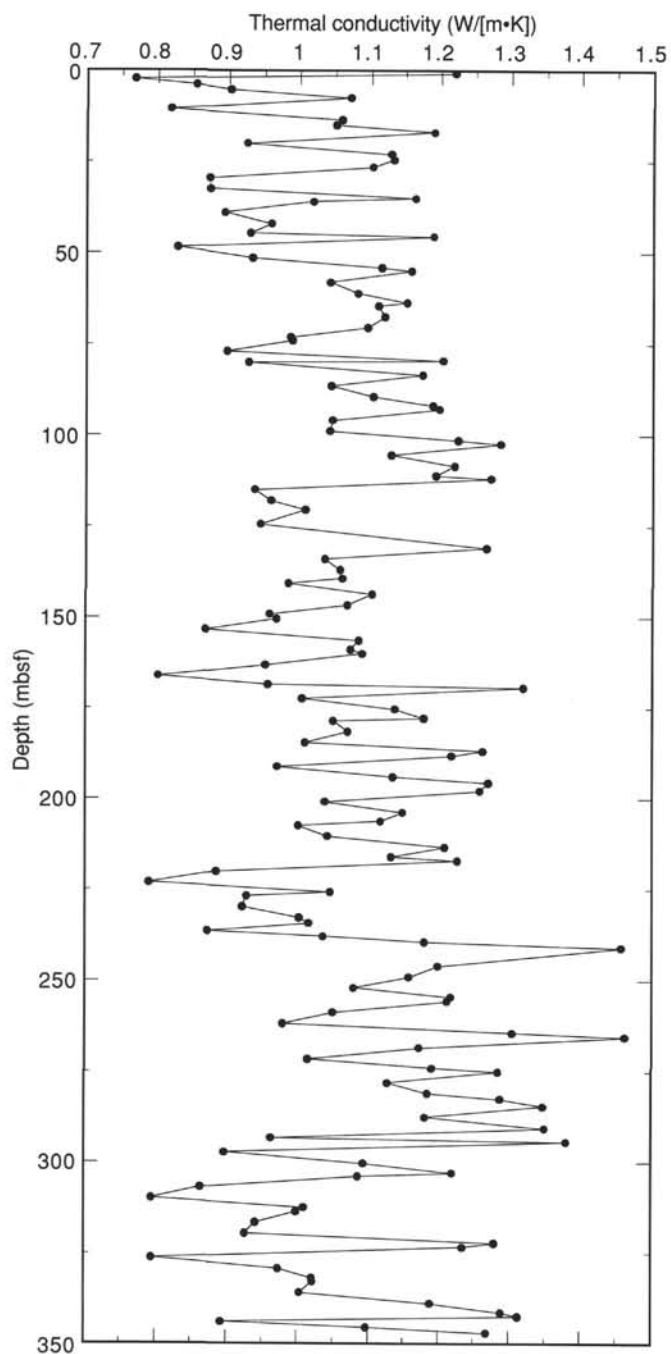
Figure 40. Thermal conductivity data vs. depth for Hole 849B.
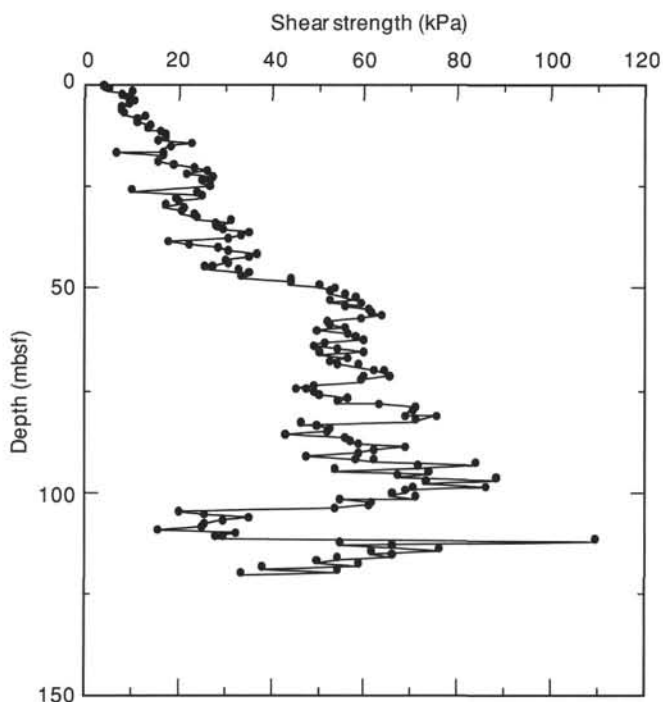
Figure 41. Undrained shear strength data vs. depth for Hole 849B.

Table 21. Summary of traveltimes, depths, and ages for Site 849 reflectors.

Reflector	Traveltime (s)	Synthetic depth (m)	Depth (mbsf)	Depth (mcd)	Age (Ma)
R1	0.021	15.90	15.40	17.40	0.56
	0.027	20.40	18.00	22.10	0.71
R4	0.065	49.20	49.30	56.90	1.86
	0.068	51.40	51.60	59.10	1.94
R6	0.077	58.20	57.70	67.20	2.22
	0.081	61.30	59.90	69.40	2.30
R7	0.083	62.80	63.90	74.60	2.48
	0.090	68.00	66.20	76.90	2.56
R8	0.100	75.70	76.70	88.35	2.97
	0.105	79.50	80.00	91.65	3.08
R9	0.113	85.60	86.20	98.00	3.30
	0.116	88.60	87.70	99.50	3.36
R11	0.130	98.50	98.20	111.80	3.82
	0.135	102.30	99.90	113.50	3.89
R13	0.142	107.60	105.90	120.40	4.17
	0.145	109.90	107.00	121.50	4.21
R18	0.187	142.10	141.50	162.00	4.71
	0.191	145.10	143.60	164.10	4.73
R22	0.219	167.30	167.30	192.30	4.99
	0.226	172.90	172.30	198.70	5.10
R27	0.255	196.70	197.00	228.20	5.59
	0.260	201.00	201.60	232.80	5.66
R30	0.276	214.20	213.40	245.50	5.87
	0.279	216.70	217.00	249.90	5.95
R31	0.291	226.50	230.60	264.70	6.19
	0.294	229.00	231.90	266.00	6.21
R32	0.305	237.90	236.50	270.80	6.29
	0.312	243.90	241.80	276.10	6.38
R37	0.343	270.60	269.20	303.60	7.34
	0.346	273.30	271.50	309.90	7.46
R40	0.365	289.70	288.90	325.00	7.80
	0.369	293.40	293.10	329.10	7.90
R41	0.373	296.80	296.60	333.60	8.01
	0.377	300.20	300.20	337.20	8.09
R44	0.404	322.20	323.00	362.90	9.99
	0.409	326.50	326.90	366.80	10.07
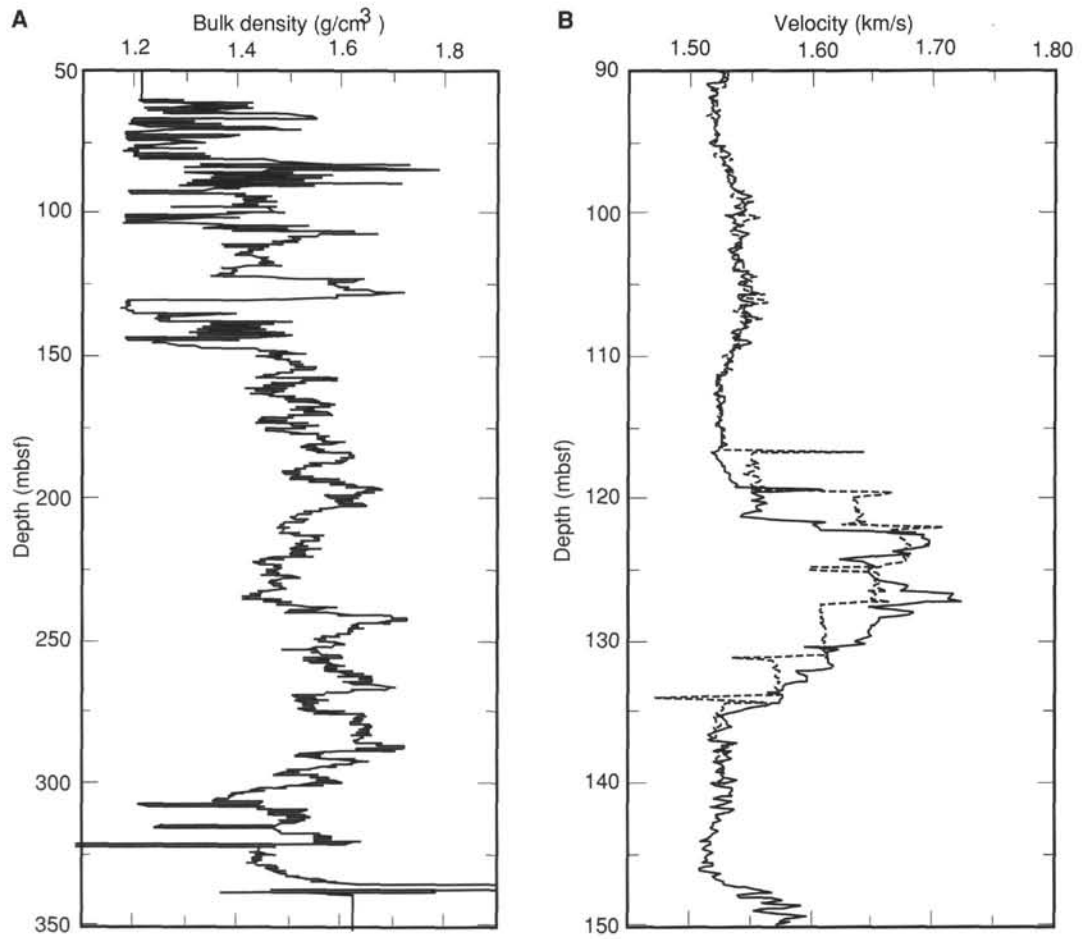
Figure 42. Plots of log bulk density (**A**) and velocity (**B**) vs. depth in Hole 849B. In (**A**), note the numerous drop-outs in density values, particularly above 130 mbsf. In (**B**), dashed line indicates the velocity log that resulted from the initial run of the GST; stepped pattern is a result of this tool sticking in the borehole. Solid line shows results from a repeat run, indicating that the peak in velocity observed in the initial log is real, but that the structure was induced by tool problems.

Table 22. Backtracked path for Site 849.

Age (Ma)	Latitude (°S)	Longitude (°W)
1	0.15	109.74
2	0.40	108.97
3	0.65	108.20
4	0.89	107.44
5	1.13	106.67
6	1.37	105.90
7	1.61	105.13
8	1.84	104.36
9	2.07	103.59
10	2.30	102.82
11	2.52	102.04
12	2.74	101.27

Pole of rotation: 0–12 Ma; 67.0°N, 59.0°W.
Angular velocity: 0.84°/m.y.
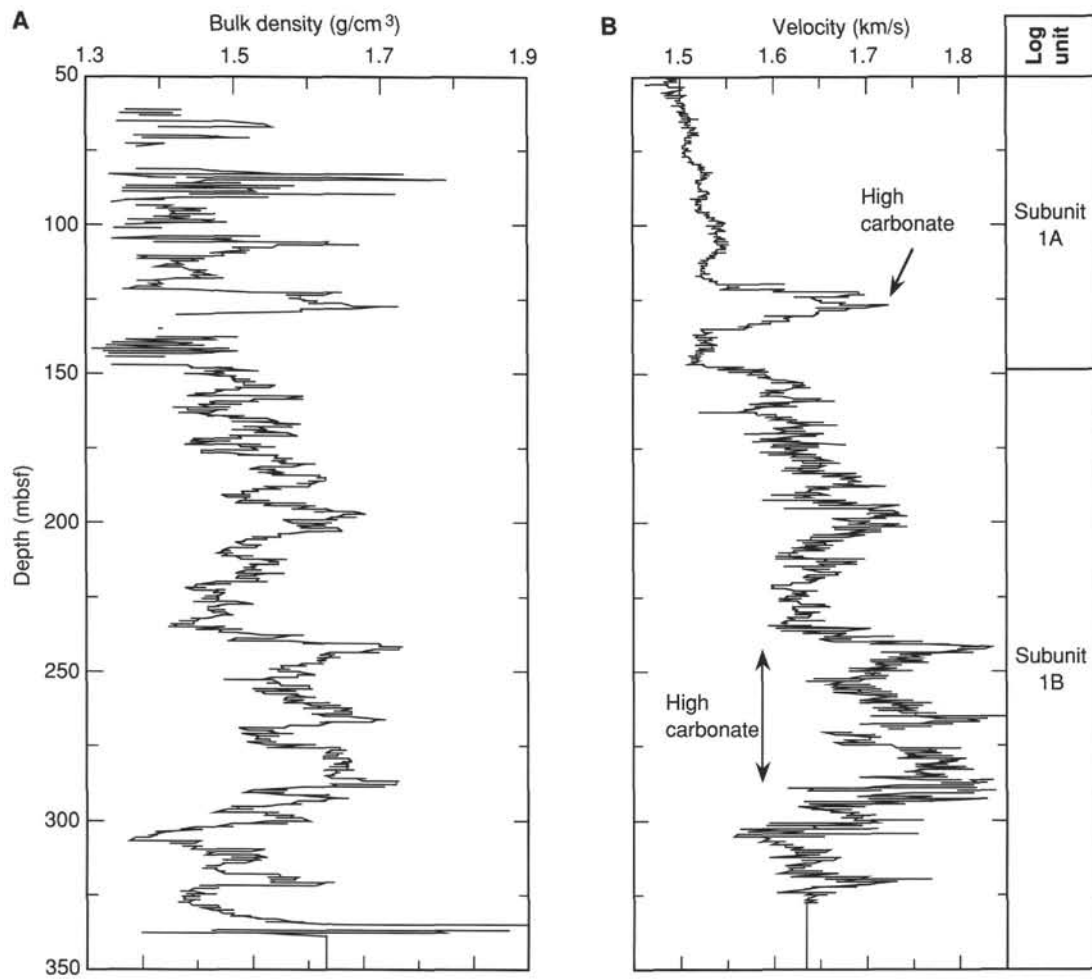
Figure 43. Plots of edited bulk density (**A**) and velocity (**B**) vs. depth; all density values <1.3 g/cm^3 have been eliminated. Log units shown on right.
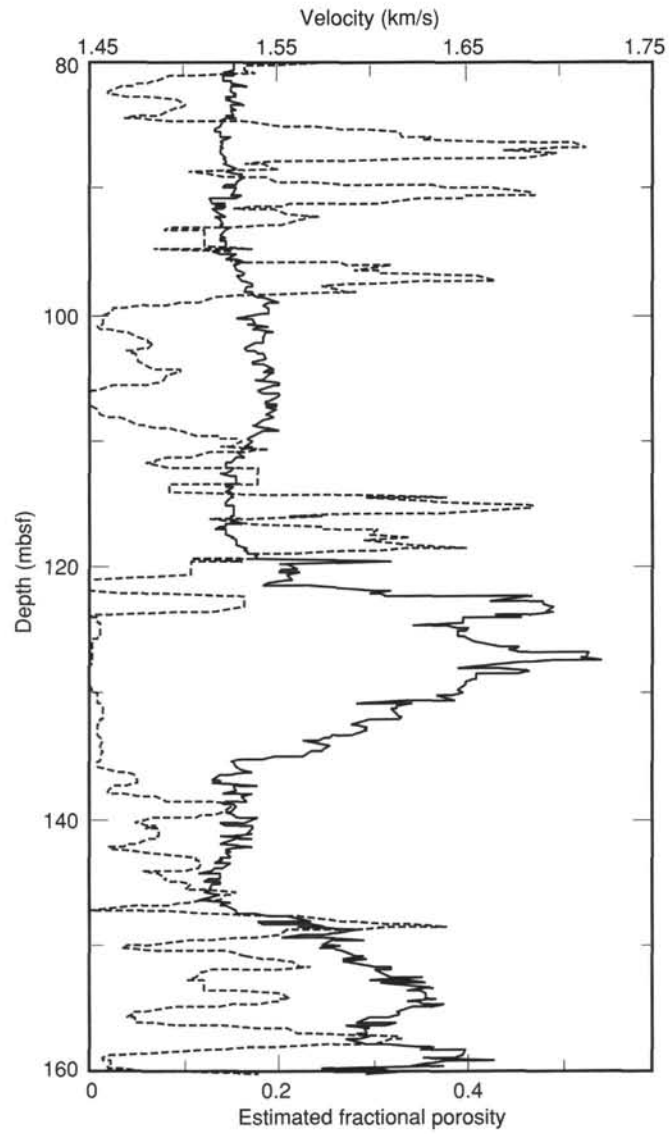
Figure 44. Velocity (solid line) and porosity estimated from neutron geochemical logging results (dashed line) vs. depth in the interval from 80 to 160 mbsf. Note the decrease in estimated porosity from 120 to 136 mbsf, which corresponds to the interval in which velocity is anomalously high.
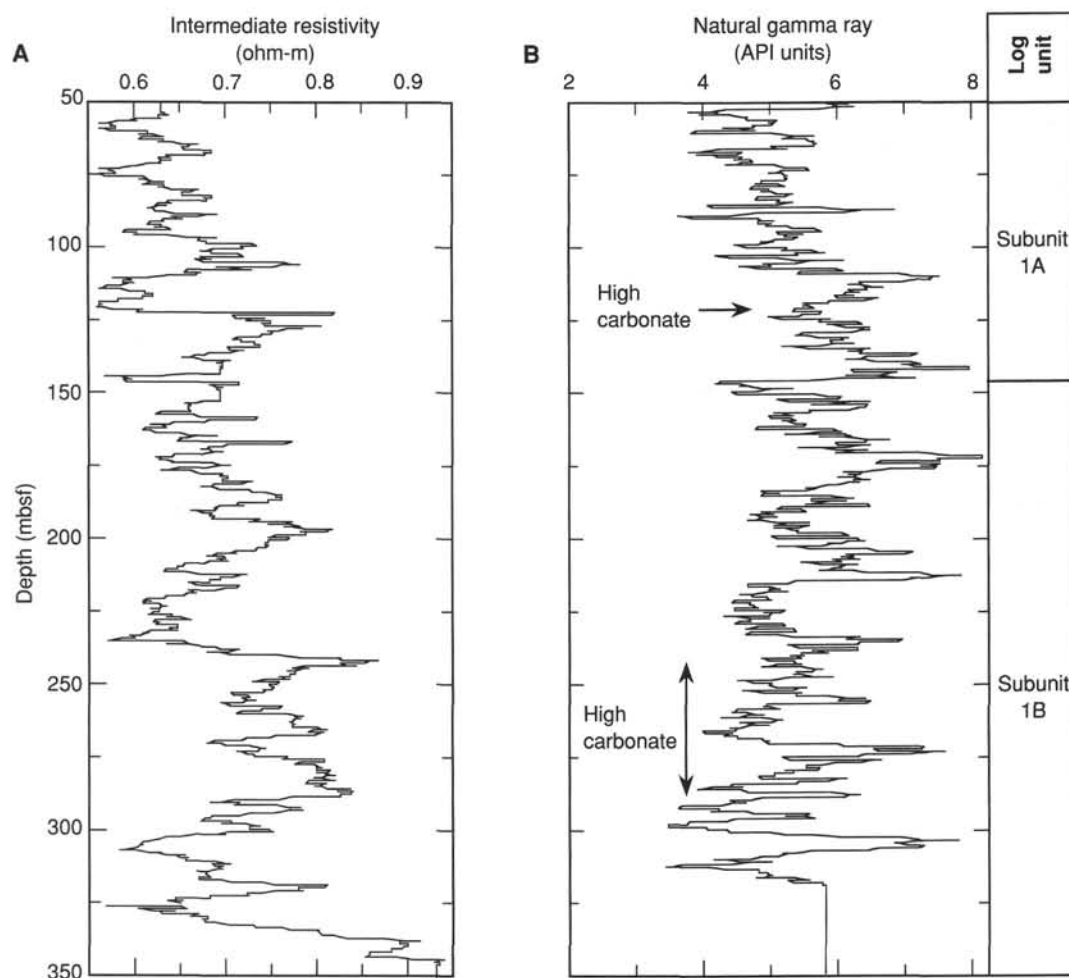
Figure 45. Intermediate resistivity (**A**) and natural gamma-ray measurements (**B**) vs. depth. Log units shown on right.
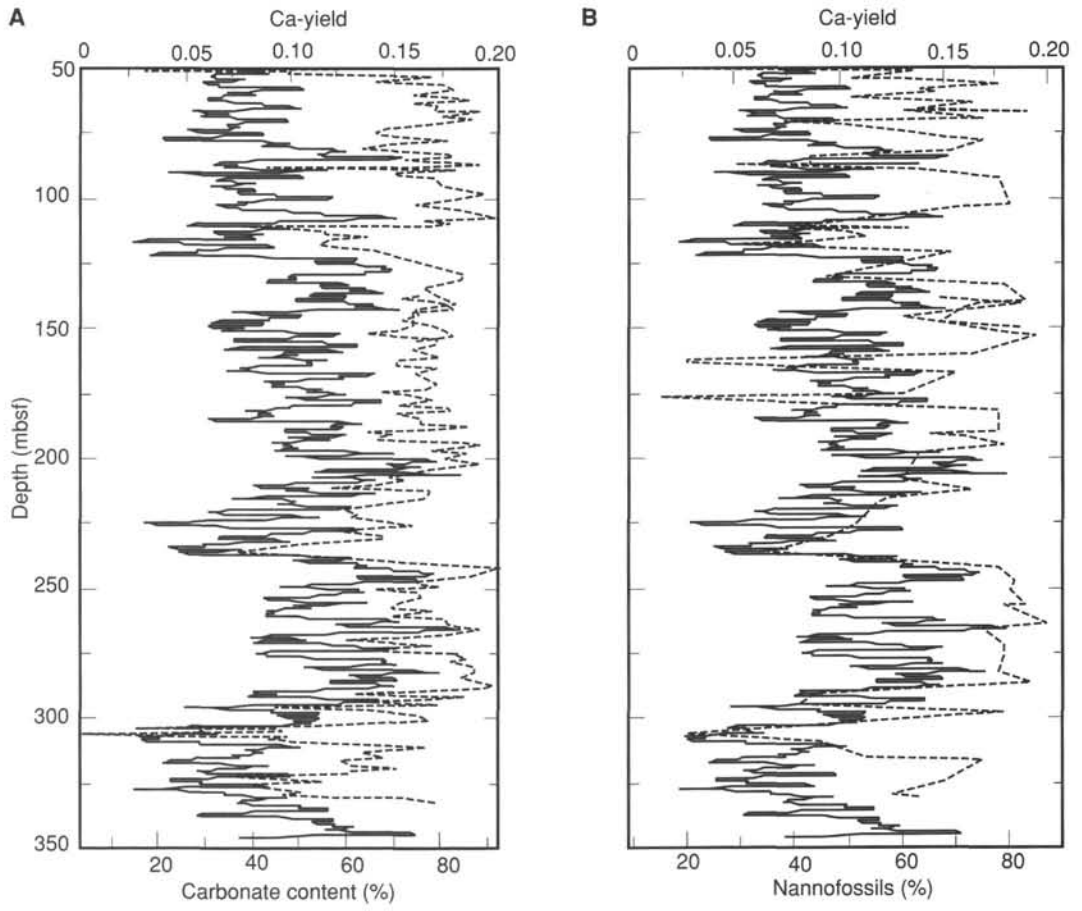
Figure 46. Ca-yield values (solid line) and laboratory-determined carbonate content (dashed line) vs. depth (**A**) and Ca-yield values (solid line) and nannofossil concentrations (dashed line; estimated from smear slides) vs. depth (**B**). Good correlations between Ca-yields and these other estimates of $CaCO_3$ were observed.
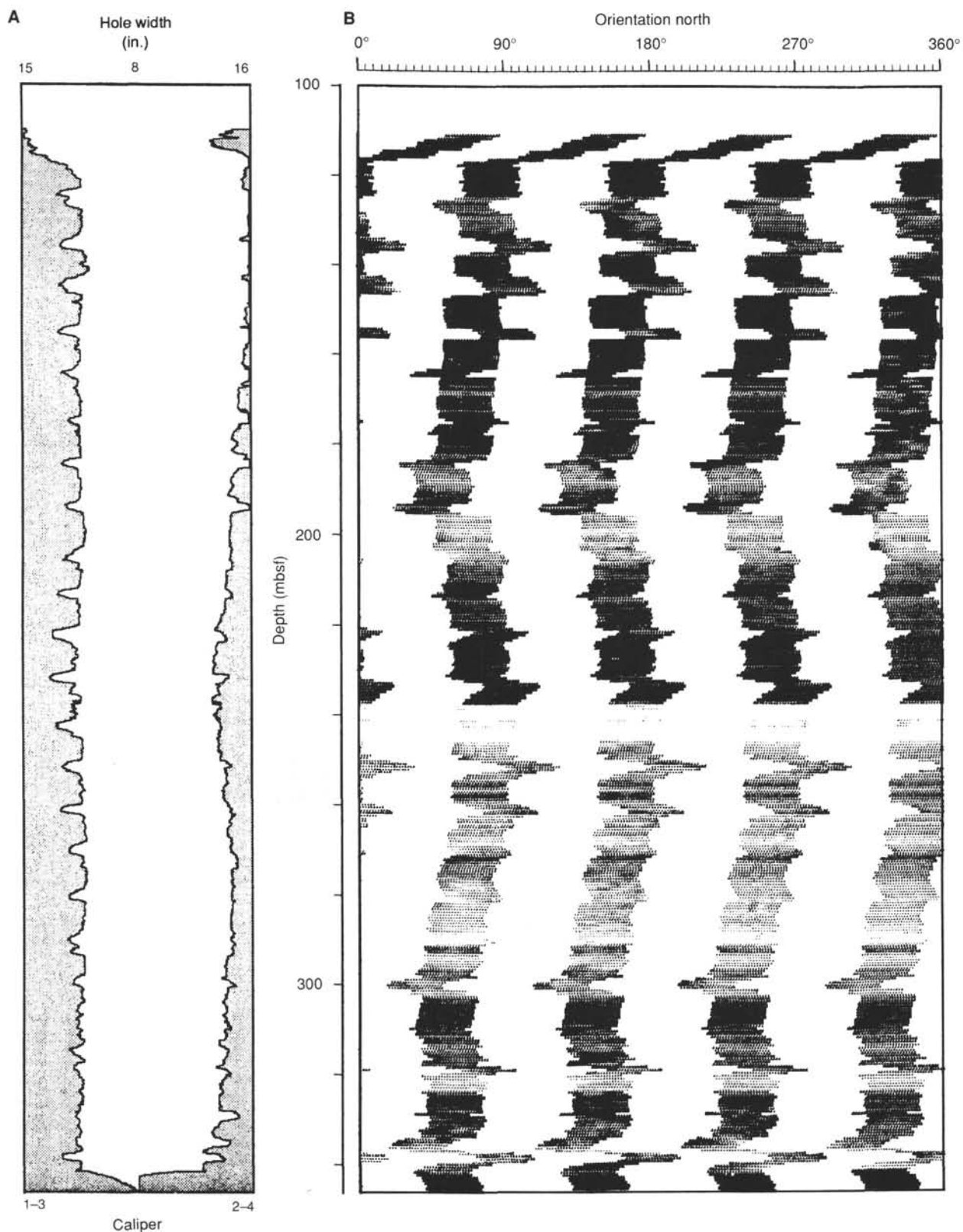
Figure 47. FMS caliper log (**A**) and image (**B**) in Hole 849B. The most striking event in the FMS log is present at approximately 240 mbsf, where resistivity increases sharply and remains high to a depth of 244 mbsf. In the caliper log, note the change in borehole shape at 116 mbsf and the 9.5-m cyclicity in borehole diameter caused by drill-pipe standoff.
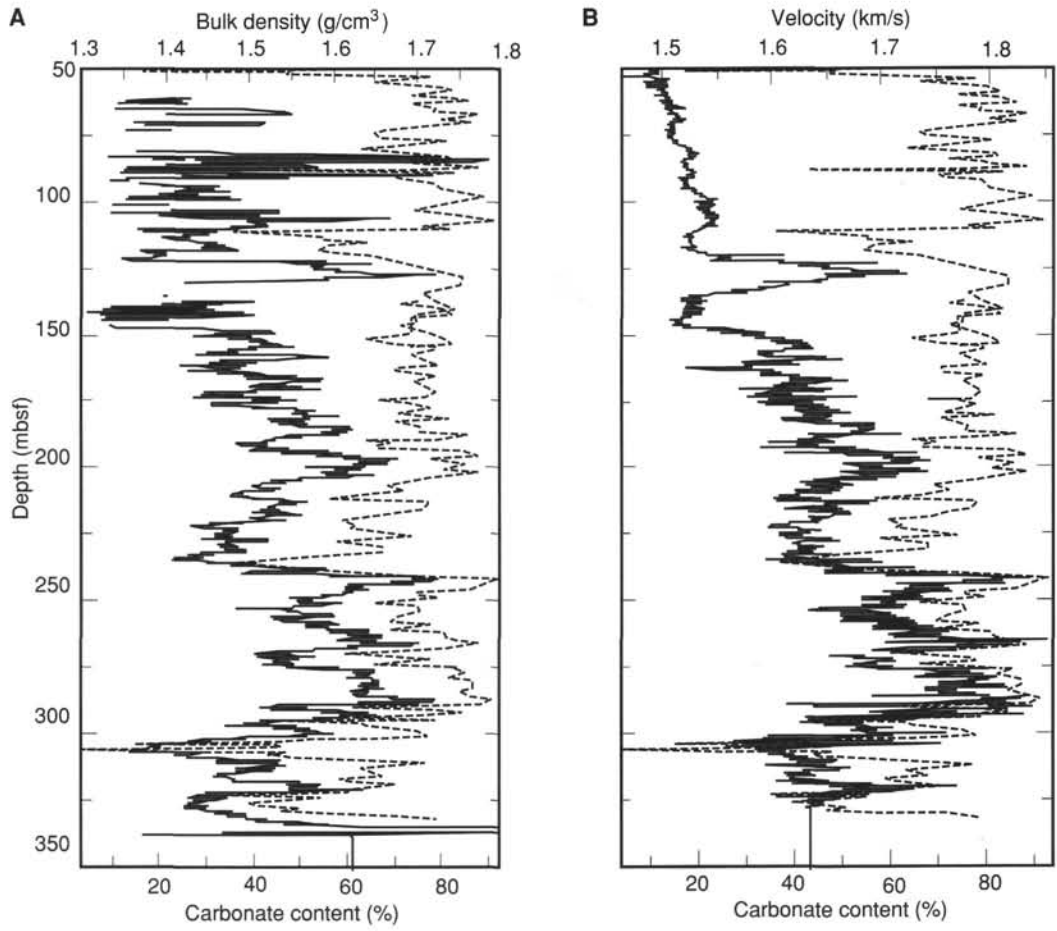
Figure 48. Laboratory carbonate contents (dashed lines) and bulk density (**A**) and velocity (**B**) vs. depth. Good-to-excellent correlations between carbonate and physical property values exist in Subunit IB.
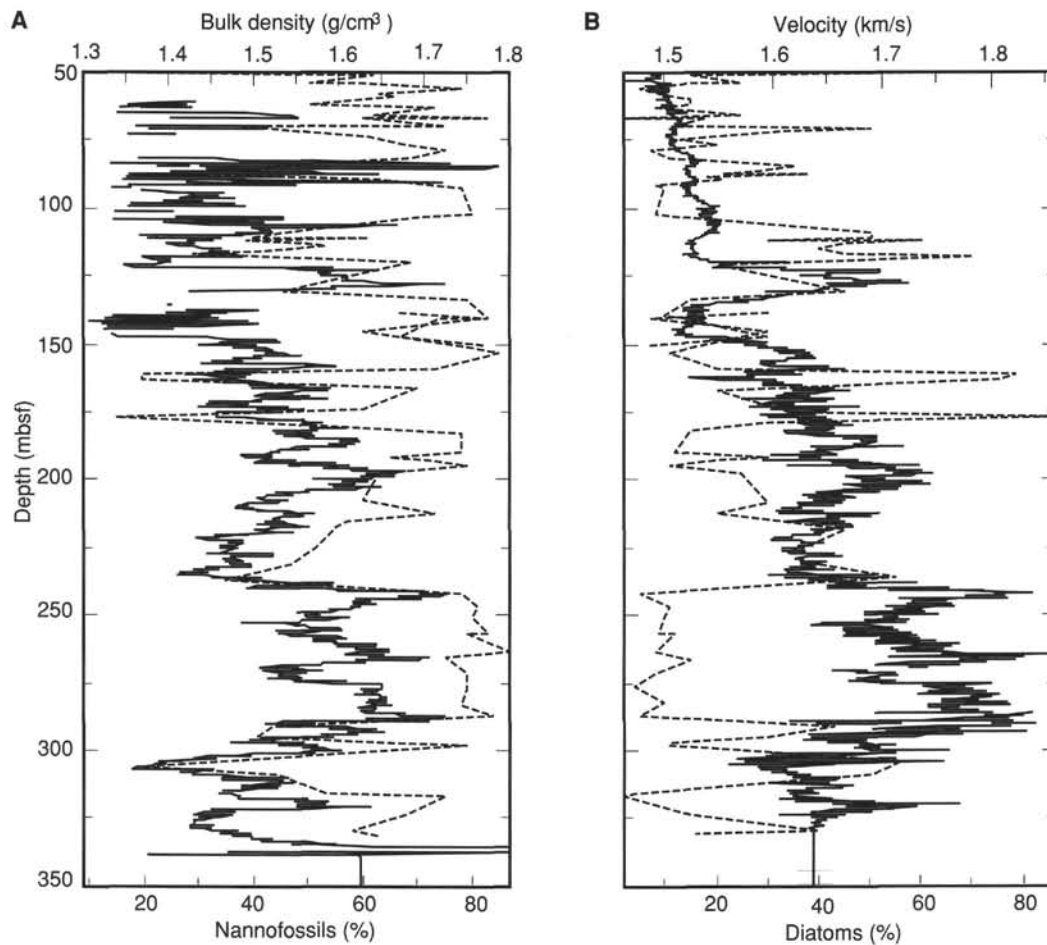
Figure 49. Log physical properties and microfossil concentrations (estimated from smear slides) vs. depth. **A.** Bulk density (solid line) and nannofossils. **B.** Velocity (solid line) and diatoms (the dominant siliceous microfossil). Relationships among these physical properties and calcareous microfossils are positive, while those with siliceous microfossils are inverse.
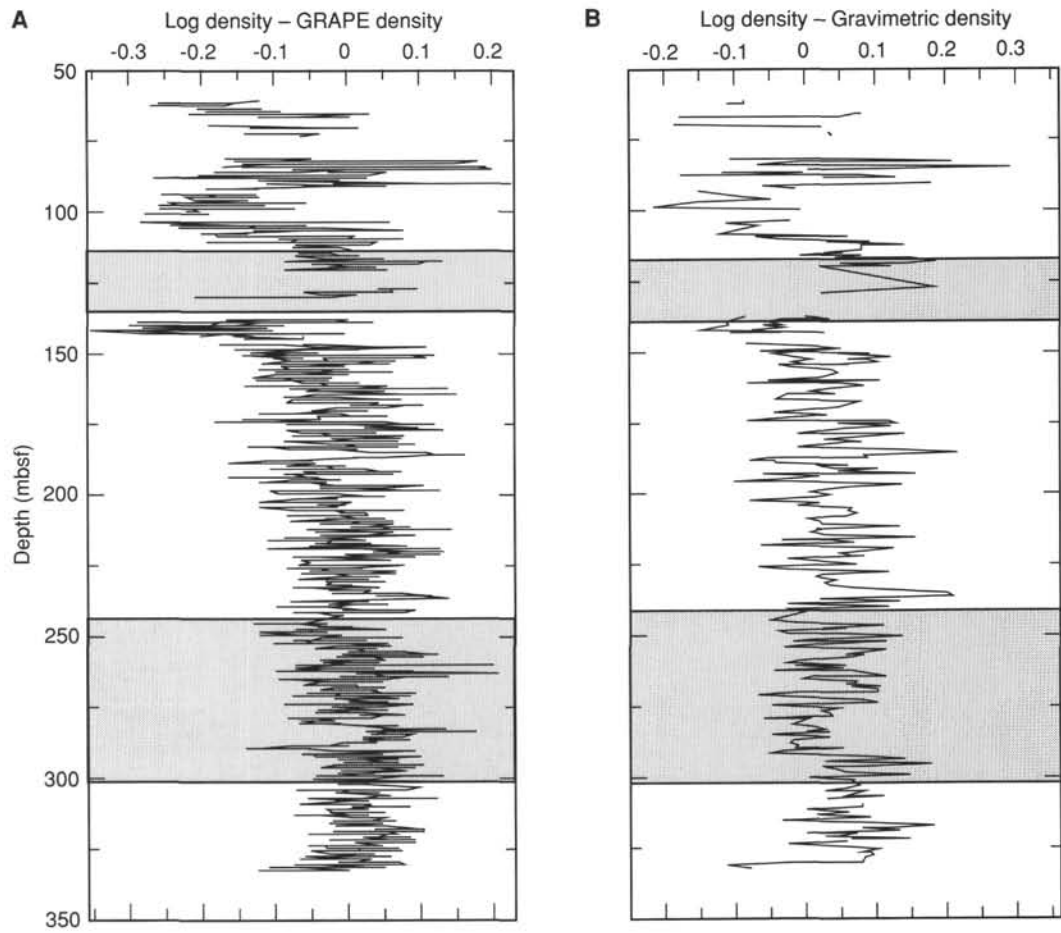
Figure 50. Density differences between log and shipboard measurements vs. depth. **A.** Log density minus GRAPE density. **B.** Log density minus gravimetric density. Shaded areas represent high carbonate intervals.
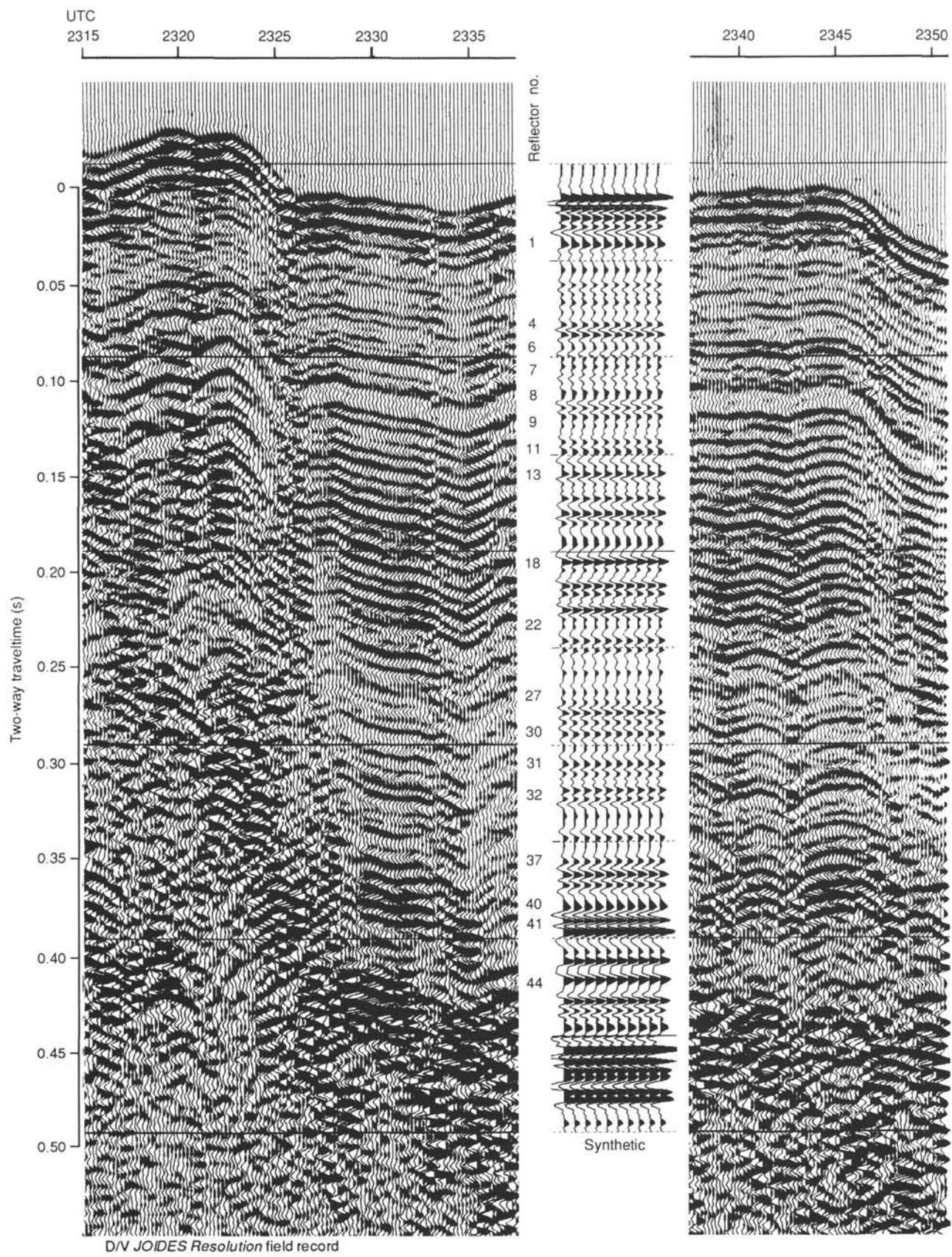
Figure 51. Comparison of synthetic seismogram with field record, Site 849.
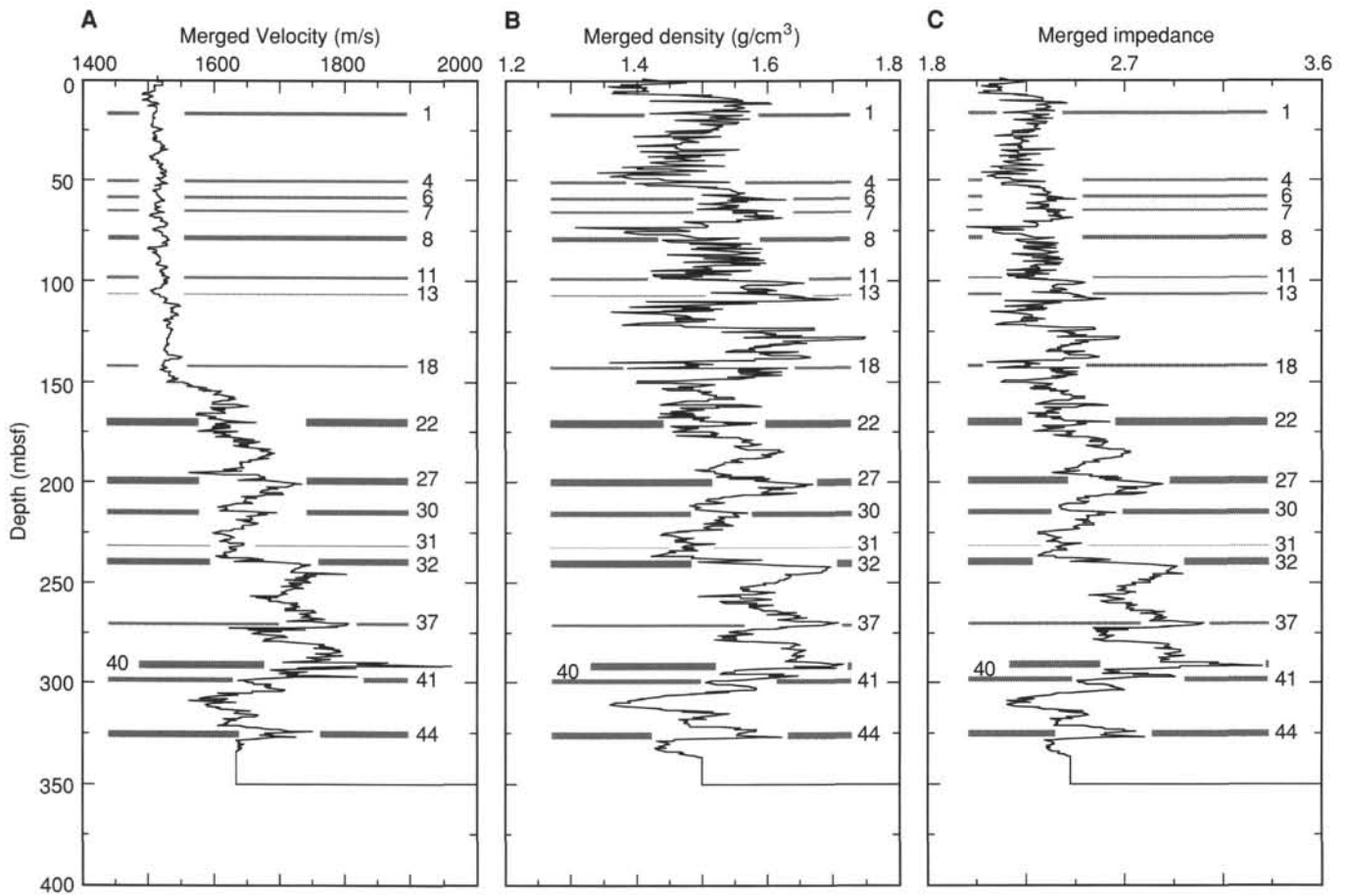
Figure 52. Data used for generating Site 849 synthetic seismograms. **A.** Velocity. **B.** Density. **C.** Acoustic impedance. The 17 reflectors selected from the synthetic seismogram have been shown for comparison.
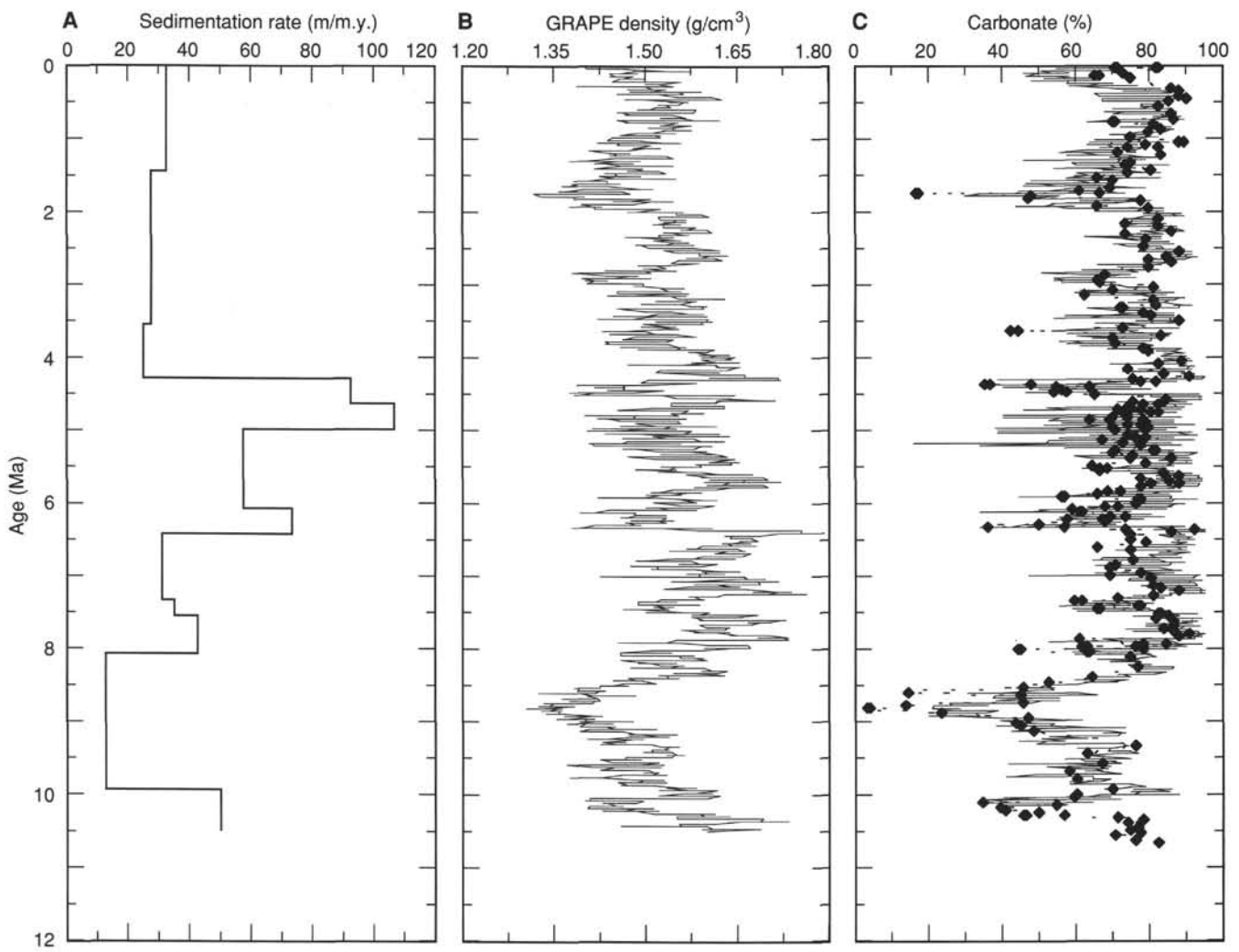
Figure 53. **A.** Sedimentation rate vs. sediment age. **B.** Sediment density vs. age. **C.** Predicted (solid line) and measured carbonate content (dashed line with solid diamonds) vs. age.

Hole 849B: Resistivity-Sonic-Natural Gamma Ray Log Summary
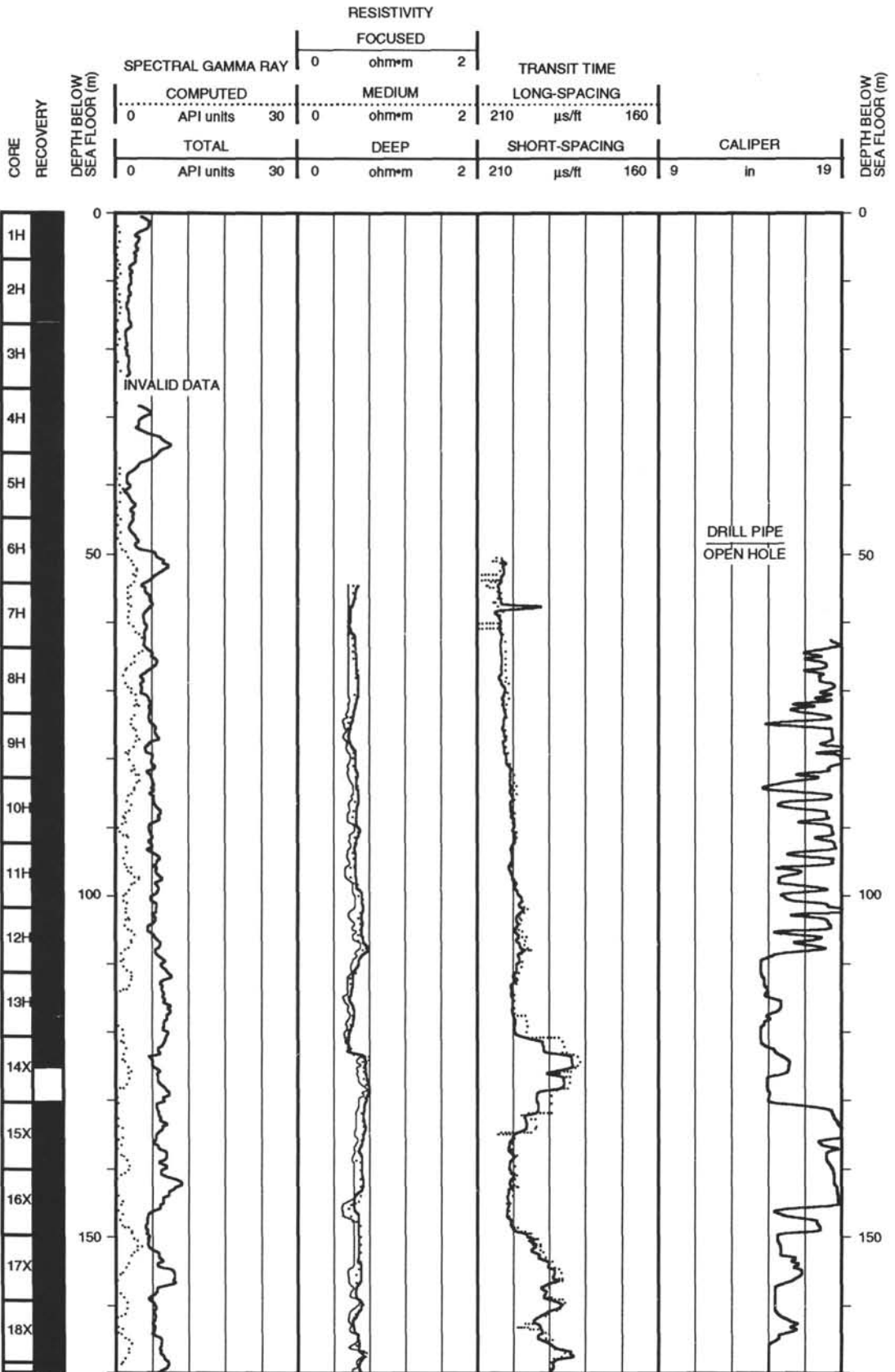
Hole 849B: Resistivity-Sonic-Natural Gamma Ray Log Summary (continued)
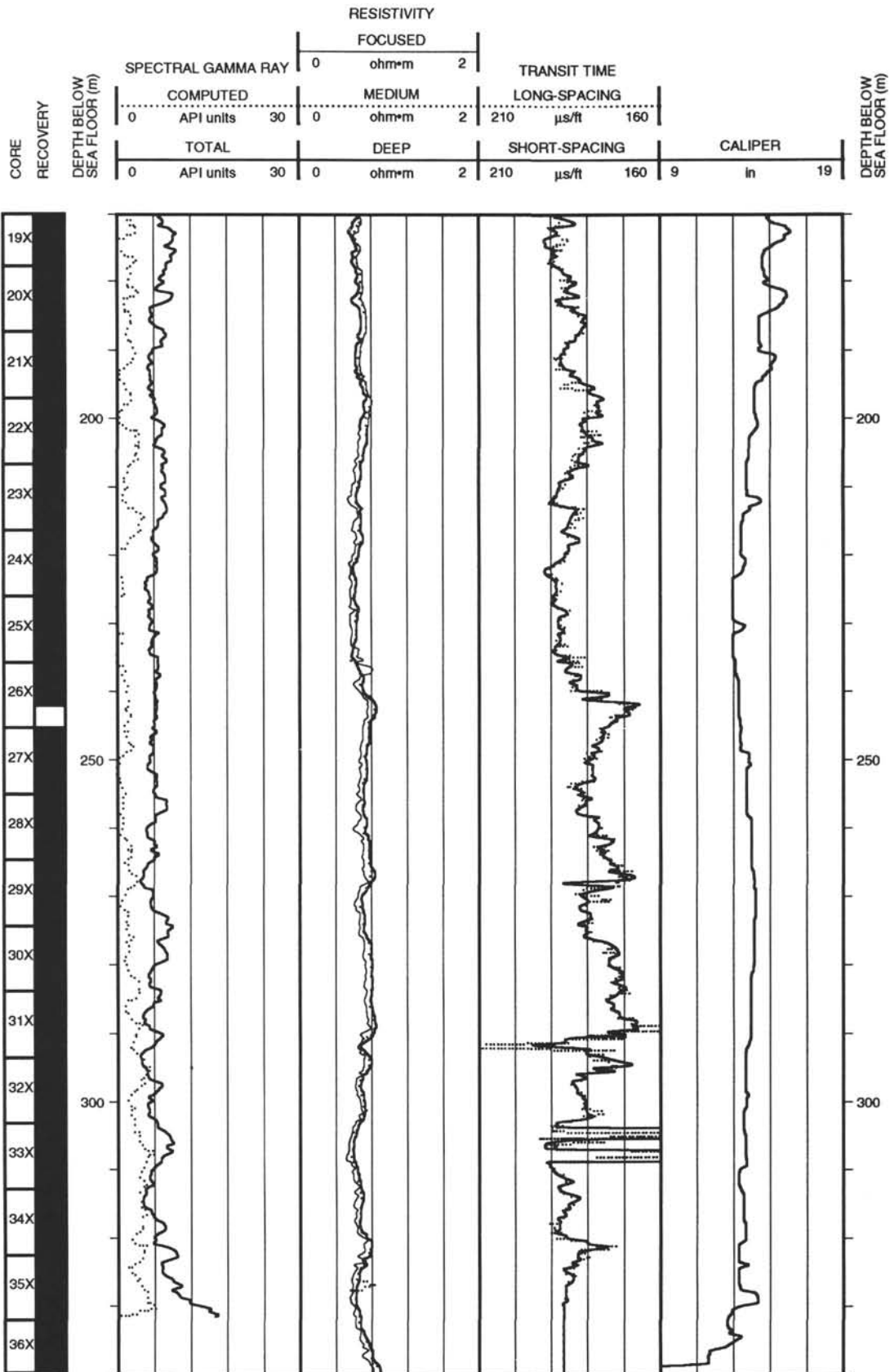
Hole 849B: Density-Natural Gamma Ray Log Summary

Hole 849B: Density-Natural Gamma Ray Log Summary (continued)

Hole 849B: Geochemical Log Summary

Hole 849B: Geochemical Log Summary (continued)